Application of TLM for Optical Microresonators

Harshana Gihan Dantanarayana,
BEng.(Hons.)

Thesis Submitted to the University of Nottingham
for the degree of Doctor of Philosophy

November 2012

Abstract

Optical microresonators can form the basis of all-optical switching and control devices. The presented study is an exploration of the Transmission Line Modelling (TLM) method as a suitable candidate for designing optical microresonators. Chalcogenide glasses were identified as promising materials, with which to fabricate optical microresonators.

The study presents the formulation of TLM in two dimensions to model nonmagnetic dielectric materials and a suitable computationally efficient yet flexible software design. Some methods for extracting spectral properties of resonators are compared and the modified difference Prony method was identified as a suitable tool to extract resonant frequencies and Q factors from a limited time signal.

When applying TLM to microresonators of sub-wavelength dimensions it was understood that the method of discretisation plays an important role in accurately modelling microresonators. Two novel methods of discretisations - the *same area method* and the *anti-aliasing method* - were used to improve the accuracy significantly compared to existing mesh refinement techniques. Perfect matched layers (PMLs) were implemented to improve reflections from domain truncation using several methods. A Convolutional PML(CPML) was identified as the best, but it does not reach the efficiency of PMLs in the Finite Difference Time Domain (FDTD) method.

Several frequency dependent refractive index models were proposed and implemented in TLM. A Tauc-Lorentz model was identified as the best fit to the experimental refractive index of three chalcogenide glasses, but a Sellmeier model with one term and a coefficient was efficient for TLM implementation. The main concern in the use of these models within TLM was shown to be the error arising due to mesh dispersion.

Kerr nonlinear models were formulated and implemented in TLM and the models applied to the study of a waveguide junction. Compared to an equivalent implementation in a time domain beam propagation method, TLM models better represent the waveguide junction reflections.

List of Publications

The following journal and conference papers have resulted in whole or part from the work described in this thesis.

[1] H. Dantanarayana, X. Meng, P. Sewell, A. Vukovic, and T. Benson, "Techniques for embedding non-linear materials in tlm," in *Transparent Optical Networks (ICTON), 2011 13th International Conference on*, pp. 1–4, IEEE, 2011.

[2] H. Dantanarayana, A. Vukovic, P. Sewell, Z. Lian, D. Furniss, A. Seddon, E. Romanova, A. Konyukhov, B. Derkowska, J. Orava, *et al.*, "The optical properties of chalcogenide glasses: From measurement to electromagnetic simulation tools," in *Transparent Optical Networks (ICTON), 2010 12th International Conference on*, pp. 1–4, IEEE, 2010.

[3] K. Le, H. Dantanarayana, E. Romanova, T. Benson, and P. Bienstman, "Comparative assessment of time-domain models of nonlinear optical propagation," in *ICTON Mediterranean Winter Conference, 2009. ICTON-MW 2009. 3rd*, pp. 1–4, IEEE, 2009.

[4] H. G. Dantanarayana, A. Vukovic, P. Sewell, and T. M. Benson, "Resonant frequency and Q factor extraction from temporal responses of ultra high Q optical resonators," *IET Journal of Science Measurement and Technology*, Under Review.

Acknowledgement

First and foremost I very much grateful to Professor Trevor Benson for giving me this opportunity to read for a PhD under his supervision. I am forever thankful for the guidance and help extended towards me to complete my studies successfully at the University of Nottingham. Further his kindness and understanding rendered throughout my study during my ups and downs is greatly appreciated.

I would also like to thank my co-supervisors Prof. Phillip Sewell and Dr. Ana Vukovic for the help and support given to me when I stumbled upon dazzling problems. I would also like to mention Dr. Steve Greedy, Dr. Chris Smartt, and Dr. Ahmed Al Jarro for the useful discussions we had during my stay at Nottingham. I would also like to thank Members of the George Green Institute for Electromagnetics Research including Dr.Ken Chan, Dr. Hiroki Wakatsuchi, Sendy Phang and Vicky Meng for their support and friendship.

I am very much grateful for my wife for standing beside me during these years and enduring hardships especially during my thesis writing period. I would also like to mention my son who at most of the times cooperated when daddy couldn't be with him even on weekends. I would also like to thank my parents in law for helping me during this period.

Lastly I would like to thank my parents for not only helping through all my student years and standing beside me, but also for bringing me up and making me who I am today.

Contents

List of Symbols

Notation	Description
J_{ef}	Electrical curent density.
J_{mf}	Magnetic curent density.
$\chi_e^{(2)}$	Seond order electrical nonlinear suceptibility of a material.
$\chi_e^{(3)}$	Third order electrical nonlinear suceptibility of a material.
χ_e	Electrical suceptibility of a material.
χ_m	Magnetic suceptibility of a material.
η_0	Wave impedance of freespace.
η	Wave impedance of a material.
$\mathbf{E}$	Electric field vector.
$\mathbf{P}$	Electrical Polarisation vector.
μ	Magnetic permeability of a material.
ω	Angular Frequency.
σ_e	Electrical conductivity.
σ_m	Magnetic conductivity .
ε_0	Dielectric permittivity of freespace.
ε	Dielectric permittivity of a material.
c	Phase velocity of light in freespace.

Notation	**Description**
n_2	Kerr nonlinear coefficient.
$\Im$	Imaginary part of a complex number.
PDE	partial differential equation.
$\Re$	Real part of a complex number.
SCN	Symmetrical Condensed Node.
sinc_π	Normalised sinc function $\mathrm{sinc}_\pi(x) = \mathrm{sinc}(\pi x)$.

1

Introduction

Light is without doubt the first encounter of our lives. In the past, many philosophers have attempted to unravel the nature of light in belief of achieving control over light. It has been interpreted as rays, waves, electromagnetic waves, photons progressively in order to better understand light's behaviour. All of these methods are applicable in their own domains and have been used successfully to control light to some extent. But, why are we trying to control light ?

Light is not only the first but the fastest 'thing' known to mankind. Therefore, taking control of the fastest 'thing' is bound to have favourable outcomes. As we have understood from the theories built upon classical and quantum foundations, its speed and path depends only upon the material in which light travels. Hence, by tailoring the material structure, we have been able to guide light in designated paths according to our needs. Light signals guiding in optical fibres has led to building a massive communication network all around the world. Yet, the scientific community is not content with the amount of control of light with guiding.

Even though light guiding structures make fast communication links, slow electrical signals are used to control light switching through and in between guides. This eventually slows down the communication to the speed of elec-

trical signals. Therefore, photonic research is now steering towards forming controllers actuated by optical signals. This new era is widely characterised by 'All Optical' devices.

All optical devices require some essential building blocks similar to their electrical counterparts. These include all optical oscillators, modulators, mixers, amplifiers, filters, etc. In the electrical counterparts of these fundamental devices, resonators perform an integral role. Resonators in the optical regime are more than just a fundamental building block, deserving a study devoted to their characteristics, theoretical modelling and fabrication.

1.1 Motivation

1.1.1 Optical Microresonators

Resonators in the optical regime were conceived first as Fabry Perot (FP) interferometers. These devices contained two or more highly reflective very low loss mirrors, facing each other. Light propagates back and forth after reflecting from the mirrors, interfering each other, making a standing wave pattern between the mirrors. Two mirror Fabry Perot resonators and three mirror ring resonators were very popular. These have been extensively used in lasers, and even in modern day semiconductor lasers. The performance of these devices highly depend upon the reflectively of the mirrors. In a laser, the medium between the mirrors contain a gain medium to support stimulated emission. Hence, Fabry Perot resonators have been key devices in optical research [1].

Despite wide adoptation of Fabry Perot resonators, they have some shortcomings when they are integrated. FP resonators with high Quality factors (defined in chapter 3) tend to be bulky and large ($\approx cm$). Miniaturising FP resonators yield either meagre resonator properties such as low Q factors or become complex devices that are painstaking and expensive to fabricate [2]. Hence, FP devices with high Q factors have become impractical to be used in integrated optics. Hence, research was sought to explore simpler devices

with high Q factors and tight optical confinement.

Distributed Bragg reflector (DBR) resonators have become a better alternative to FP resonators with a similar structure. DBR resonators replace the two mirrors of the FP resonators by reflector structures composed of alternative thin layers of two dielectric materials with different refractive indices; the interfaces between layers acting as frequency dependant partial mirrors. The number of layers, the ratio of the two refractive indices (contrast ratio), and the size of the cavity determine the transmission and reflection properties of such a DBR resonator. High Q DBR resonators have also been integrated as ridge waveguides in optical circuits. These intriguing features of DBR resonators have made them very popular in modern solid state lasers [3].

Photonic Crystal (PhC) resonators takes the concept of DBR further by increasing the periodicity of the mirrors to two or three dimensions. By introducing a defect within a periodic structure, light can be confined at the defect site achieving resonance [3]. The confinement region is usually sub wavelength (nm). In addition, they are ideal for integrated optics as multitude of devices can be made on a periodic structure by breaking the periodicity. Since photonic crystals are relatively newer than other resonator structures and favourable for all optical circuits, a lot of research effort is being put into this area [4].

Monolithic resonators, which can be considered as open dielectric counterparts of metal microwave resonators, confine light by almost total internal reflection. Within these resonators, light travels in closed contours near the dielectric boundaries of the resonators. In circular resonators, these optical paths (modes) are known as "Whispering Gallery Modes". The name is given on historical grounds, considering the studies carries out by Lord Rayleigh and Debye [5]. Further, "whispering gallery like modes" such as "Bow tie" resonances occur in chaotic resonators such as square and spheroidal resonators, where the circular symmetry is disturbed. Yet in all of these resonators, light is mostly confined to the perimeter yielding a low modal volume even though the total volume of the resonator is higher than that of PhC and DBR resonators. In addition, the experimentally fabricated monolithic resonators

provide the highest Q factor available of all resonator types [2, 6]. Table 1.1 shows some high Q resonators and their properties according to the literature. Due to high Q factor and low modal volume, monolithic resonators have been at the forefront of optical resonator research.

Table 1.1: Various types of high Q and ultra high Q optical resonators present in the literature.

Resonator	Material	Method	Size	Q factor	Ref.
Fabry Perot	BK7	Assembly	$1.75m$	5×10^{11}	[7]
Bragg Cavity	AlAs/GaAs	Ion etching	$4\mu m$	1.65×10^{5}	[8]
PhC.	Silicon		$1 - 2\mu m$	4.5×10^{4}	[9]
Ring	SiliconNitride	Chemical Vapour Deposition	$20\mu m$	3×10^{6}	[10]
Disk	As_2S_3	Lithography	$40\mu m$	2×10^{5}	[11]
Spheroidal	CaF_2	Polishing	$1mm$	2×10^{10}	[12]
Spherical	As_2Se_3	Thermal Reflux	$100\mu m$	2×10^{6}	[13]
Spherical	As_2Se_3	laser fusing	$2 - 25\mu m$	2×10^{4}	[14]
Spherical	GaLaSO	Thermal Reflux	$100\mu m$	8×10^{4}	[15]
Microtoroid	Polymer	Lithography	$100\mu m$	3×10^{5}	[16]
Microtoroid	Silica	Lithography & Etching	$50\mu m$	1.2×10^{8}	[17]
Cylinder	CaF_2	Polishing	$5mm$	6.3×10^{10}	[18]

1.1.2 Applications

Open dielectric resonators mentioned previously such as rings, and disks are already being used in wavelength division multiplexing devices as add drop filters [19]. Further, use of resonators in light sources change the properties of both spontaneous emission and stimulated emission yielding novel light emitting diodes and ultra-low threshold lasers [20]. Due to the enhancement of nonlinearities in the material within micoresonators, as an effect of high Q and high confinement, Kerr and Raman nonlinear phenomena have been

observable at low optical powers [20, 21]. These advantages have become a key in realising ultra low threshold Raman lasers and nonlinear mixers [20]. Hence, the microresonators have proven to be more advantages to telecommunication applications than was expected.

In addition to the applications in telecommunications, a new range of sensing applications have evolved due to the sensitivity of the resonances of microresonators to surrounding materials. Adsorption of chemical compounds or proteins is highly detectable via the resonance shifts of microresonators [22]. Hence monolithic microresonators have been widely used in label free biological and chemical sensing with high particle resolution.

The very high Q factors achievable as large as 10^9 in silica microspheres [3], enhances various optical phenomena, which would otherwise be unrecognisable in FP resonators. This optical phenomenon is not only confined to previously mentioned Kerr, Raman, and stimulated effects, but spreads out to photon, phonon, exciton interactions. Hence, these resonators have found themselves as the subject of fundamental physics experiments [3].

According to the discussion led so far, it is evident that the applications of microresonators are immense and fascinating. They are very much bound to define their territories on all optical devices. However, as one should notice, these structures have been limited to simple canonical geometries. It is unarguably for the fabrication simplicity; But is that it? We must explore the challenges that lie upon us, in order to tailor the microresonators in our applications.

1.2 Background

As mentioned previously, optical microresonators are promising components for all optical switching, but have been limited to simple canonical shapes such as spheres, disks, rings, spheroidals, etc. More than for simplicity, the lack of accurate and efficient design methodologies has hindered the progression in this research area [23].

1.2.1 Simulation Techniques

Analytical studies for some canonical structures are available to help design resonators, especially spherical microresonators [5]. These studies allow identification of the Q factors and resonating frequencies in terms of the whispering gallery modes of the spherical resonators. In addition to these analytical studies, the boundary integral equation (BIE) method in the frequency domain has been able to extract the resonant modes of resonators of arbitrary shapes in 2 dimensions [24]. In most of these methods, the studies have been undertaken in the frequency domain, limiting the materials to have only frequency dependent properties. In addition, frequency domain methods do not model transients of temporal incidents, such as a state change of an optical switch or an optical memory. These require the sophistication of time domain analysis.

Comprehensive time domain methods based on Maxwell's equations, such as finite difference time domain (FDTD)[25] and transmission line modelling (TLM) method[26] have proven to be time consuming in most optical problems such as waveguides and fibres. Eventhough microresonators are small in the spacial domain, the discretisation must be high in order to avoid spurious resonances and apparent low Q factors appearing due to artificial surface roughness imparted by the discretisation. Since, resonators confine light for a long time (high Q), the simulation time must be sufficiently large aggravating the problem of already heavy computation time, even in 2 dimensions [27].

1.2.2 Chalcogenide Glasses

In search for materials suitable for microresonators, it has been vaguely possible to define characteristics of materials or limit ourselves to a set of ground rules. As a matter of fact, crystals, semiconductors, polymers, glasses and even liquids have been suggested over the past two decades as possible candidates for resonator materials [2], [28].

Chalcogenide glasses are amorphous glasses based on the group VI elements

(except oxygen and polonium in the periodic table) sulphur (S), selenium (Se), tellurium (Te), as the characteristic elements. Most of the glasses are opaque to visible light and have better characteristics in the infrared region. The characteristics can be modified by using group V or IV elements such as germanium (Ge), gallium (Ga), arsenic (As), etc. According to this broad definition, chalcogenide glasses refer to a wide range of glass compositions which are being currently investigated [29, 30].

Chalcogenide glasses have higher refractive index almost double that of silica. In terms of microresonators, this improves the light confinement. Further, nonlinearities of Chalcogenides are up to 3 orders higher in magnitude than that of silica nearing the nonlinearity range of gallium arsenides (GaAs) [30]. This implies that the optical intensity required to observe a given nonlinear change in refractive index could be 3 orders or magnitude lower for chalcogenide glasses than silica. Therefore, chalcogenide glasses are potentially interesting candidates for realising microresonators as existing nonlinear effects in the material can be enhanced further by optical confinement supported by resonators.

1.3 Thesis Outline

Having discussed the background of optical microresonators and their applications in this introductory first chapter, the main time domain simulation technique used to model these resonators are briefly discussed along with some software implementation details in chapter 2. The next chapter introduces resonator spectral properties and discusses some techniques for extracting spectral properties from time domain numerical simulations. This involves comparing several techniques along with a Fourier transform based method to identify an accurate method to determine closely spaced high Q resonances in the context of optical resonators in chapter 3.

Once a resonance identification method is established, the limitations of time domain numerical methods particularly TLM, in accurately modelling

high Q optical resonators are presented in chapter 4. Some solutions to overcome these limitations from within the numerical technique are also discussed in this chapter.

Even though limitations due to boundary reflections are not identified as particularly problematic, it will be when modelling coupling mechanisms such as waveguides. Therefore, perfect matched layers implemented in TLM are presented to produce better reflection properties in chapter Perfect Matched Layers for TLM.

Once TLM techniques are well established to accurately model optical resonators with linear constant dielectric materials, dispersive Chalcogenide materials are modelled in TLM and the associated limitations are discussed in chapter 6. As a part of linear material properties, optical loss is also discussed in the chapter to study its effects on Chalcogenide optical resonators.

As the last theoretical exploration, optical Kerr nonlinearity present in Chalcogenide materials are modelled in TLM in chapter 7. The method developed is compared with a nonlinear approximate frequency domain technique to identify the model's strengths and weaknesses in modelling nonlinear waveguides.

References

[1] J. Liu, *Photonic Devices*. Cambridge University Press, 2005.

[2] A. Matsko and V. Ilchenko, "Optical resonators with whispering-gallery modes-part i: basics," *Selected Topics in Quantum Electronics, IEEE Journal of*, vol. 12, no. 1, pp. 3–14, 2006.

[3] K. Vahala, *Optical microcavities*. World Scientific Publishing Company Incorporated, 2004.

[4] J. Joannopoulos, R. Meade, and J. Winn, *Photonic Crystals: Molding the Flow of Light*. Princeton University Press, 1995.

[5] A. N. Oraevsky, "Whispering-gallery waves," *Quantum Electronics*, vol. 32, no. 5, pp. 377–400, 2002.

[6] M. L. Gorodetsky, A. A. Savchenkov, and V. S. Ilchenko, "Ultimate Q of optical microsphere resonators," *Optics Letters*, vol. 21, no. 7, pp. 453–455, 1996.

[7] A. M. D. Riva, G. Zavattini, S. Marigo, C. Rizzo, G. Ruoso, G. Carugno, R. Onofrio, S. Carusotto, M. Papa, F. Perrone, E. Polacco, G. Cantatore, F. D. Valle, P. Micossi, E. Milotti, P. Pace, and E. Zavattini, "Very high q frequency-locked fabry–perot cavity," *Review of Scientific Instruments*, vol. 67, no. 8, pp. 2680–2684, 1996.

[8] S. Reitzenstein, C. Hofmann, A. Gorbunov, M. Strauß, S. H. Kwon, C. Schneider, A. Löffler, S. Höfling, M. Kamp, and A. Forchel, "Alas/gaas micropillar cavities with quality factors exceeding 150.000," *Applied Physics Letters*, vol. 90, no. 25, p. 251109, 2007.

[9] Y. Akahane, T. Asano, B.-S. Song, and S. Noda, "High-q photonic nanocavity in a two-dimensional photonic crystal," *Nature*, vol. 425, pp. 944–947, Oct 2003. 10.1038/nature02063.

[10] A. Gondarenko, J. S. Levy, and M. Lipson, "High confinement micron-scale silicon nitride high q ring resonator," *Opt. Express*, vol. 17, pp. 11366–11370, Jul 2009.

[11] J. Hu, N. Carlie, N.-N. Feng, L. Petit, A. Agarwal, K. Richardson, and L. Kimerling, "Planar waveguide-coupled, high-index-contrast, high-q resonators in chalcogenide glass for sensing," *Opt. Lett.*, vol. 33, pp. 2500–2502, Nov 2008.

[12] A. A. Savchenkov, V. S. Ilchenko, A. B. Matsko, and L. Maleki, "Kilohertz optical resonances in dielectric crystal cavities," *Phys. Rev. A*, vol. 70, p. 051804, Nov 2004.

[13] D. Broaddus, M. Foster, I. Agha, J. Robinson, M. Lipson, and A. Gaeta, "Silicon-waveguide-coupled high-Q chalcogenide microspheres," *Optics express*, vol. 17, no. 8, pp. 5998–6003, 2009.

[14] C. Grillet, S. N. Bian, E. C. Magi, and B. J. Eggleton, "Fiber taper coupling to chalcogenide microsphere modes," *Applied Physics Letters*, vol. 92, no. 17, p. 171109, 2008.

[15] G. R. Elliott, D. W. Hewak, G. S. Murugan, and J. S. Wilkinson, "Chalcogenide glass microspheres; their production, characterization and potential," *Opt. Express*, vol. 15, pp. 17542–17553, Dec 2007.

[16] A. M. Armani, A. Srinivasan, and K. J. Vahala, "Soft lithographic fabrication of high q polymer microcavity arrays," *Nano Letters*, vol. 7, no. 6, pp. 1823–1826, 2007.

[17] S. M. Spillane, T. J. Kippenberg, K. J. Vahala, K. W. Goh, E. Wilcut, and H. J. Kimble, "Ultrahigh-q toroidal microresonators for cavity quantum electrodynamics," *Phys. Rev. A*, vol. 71, p. 013817, Jan 2005.

[18] I. S. Grudinin, V. S. Ilchenko, and L. Maleki, "Ultrahigh optical q factors of crystalline resonators in the linear regime," *Phys. Rev. A*, vol. 74, p. 063806, Dec 2006.

[19] J. Hryniewicz, P. Absil, B. Little, R. Wilson, and P. Ho, "Higher order filter response in coupled microring resonators," *Photonics Technology Letters, IEEE*, vol. 12, no. 3, pp. 320–322, 2000.

[20] S. Spillane, T. Kippenberg, and K. Vahala, "Ultralow-threshold raman laser using a spherical dielectric microcavity," *Nature*, vol. 415, no. 6872, pp. 621–623, 2002.

[21] T. Kippenberg, S. Spillane, and K. Vahala, "Kerr-nonlinearity optical parametric oscillation in an ultrahigh-q toroid microcavity," *Physical review letters*, vol. 93, no. 8, p. 83904, 2004.

[22] W. Lukosz, "Integrated optical chemical and direct biochemical sensors," *Sensors and Actuators B: Chemical*, vol. 29, no. 1, pp. 37–50, 1995.

[23] T. Benson, S. Boriskina, P. Sewell, A. Vukovic, S. Greedy, and A. Nosich, "Micro-optical resonators for microlasers and integrated optoelectronics," *Frontiers in Planar Lightwave Circuit Technology*, pp. 39–70, 2006.

[24] A. V. Boriskin, S. V. Boriskina, A. Rolland, R. Sauleau, and A. I. Nosich, "Test of the FDTD accuracy in the analysis of the scattering resonances associated with high-Q whispering-gallery modes of a circular cylinder," *J. Opt. Soc. Am. A*, vol. 25, pp. 1169–1173, May 2008.

[25] A. Taflove and S. C. Hagness, *Computational electrodynamics*. Artech House Boston, 1995.

[26] C. Christopoulos, *The transmission-line modeling method: TLM*. Institute of Electrical and Electronics Engineers, 1995.

[27] P. Sewell, T. M. Benson, A. Vukovic, and A. A. Jarro, "The challenges for numerical time domain simulations of optical resonators," in *Transparent Optical Networks (ICTON), 2010 12th International Conference on*, pp. 1–4, 2010.

[28] V. S. Ilchenko and A. B. Matsko, "Optical resonators with whispering-gallery modes-Part ii: Applications," *Selected Topics in Quantum Electronics, IEEE Journal of*, vol. 12, no. 1, pp. 15–32, 2006.

[29] A. Seddon, "Chalcogenide glasses: a review of their preparation, properties and applications," *Journal of non-crystalline solids*, vol. 184, pp. 44–50, 1995.

[30] A. Zakery and S. Elliott, *Optical nonlinearities in chalcogenide glasses and their applications*, vol. 135. Springer, 2007.

2

Transmission Line Modelling Method

The Transmission Line Modelling (TLM) technique is a time domain numerical method that is mostly used to solve the differential form of Maxwell's equations with an electrical component analogy [1]. The analogy is drawn from the similarity between the electric and magnetic field equations with the voltage and current equations of an arrangement of transmission lines in a unit cell.

This chapter briefly introduces the TLM method in the context of the two dimensional modelling of E-type waves (defined below). The original loss-free method [2] deriving from inductors and capacitors is presented as well as an alternative z-domain model used extensively in this study. The second half of this chapter presents the software design of TLM used to implement the method to balance computational efficiency and flexibility in order to adapt to various requirements of this study.

2.1 TLM formulation

In this study two dimensional electromagnetic analysis is used almost throughout in analytical closed form as well as in time domain numerical simulations. In the numerical analysis in this study, Cartesian coordinates are implied unless stated otherwise. In two dimensions, the electromagnetic fields $(E_{x,y,z}, H_{x,y,z})$ are invariant in one direction, here taken to be the z-direction (infinite dimension). Hence, three field components out of the six vanish creating two distinct sets [1]. Let E-type waves be denoted by non zero E_z, H_x, H_y and H-type waves be denoted by non zero H_z, E_x, E_y. Even though these are also noted as TE and TM formulations [1, 3], in this thesis, these names are strictly limited to guided modes to avert probable confusion of existing conventions.

2.1.1 Formulation

For E-type waves, Maxwell's equations are given by [3],

$$\begin{bmatrix} (\nabla \times \mathbf{H})_z \\ -(\nabla \times \mathbf{E})_x \\ -(\nabla \times \mathbf{E})_y \end{bmatrix} - \begin{bmatrix} J_{efz} \\ J_{mfx} \\ J_{mfy} \end{bmatrix} = \frac{\partial}{\partial t} \begin{bmatrix} \varepsilon_0 E_z \\ \mu_0 H_x \\ \mu_0 H_y \end{bmatrix} + \begin{bmatrix} \sigma_e * E_z \\ \sigma_m * H_x \\ \sigma_m * H_y \end{bmatrix} + \frac{\partial}{\partial t} \begin{bmatrix} \varepsilon_0 \chi_e * E_z \\ \mu_0 \chi_m * H_x \\ \mu_0 \chi_m * H_y \end{bmatrix} \tag{2.1}$$

where, the last letter of superscipt x, y, z denotes the component and

J_{ef}	Electrical curent density	J_{mf}	Magnetic curent density
σ_e	Electrical conductivity	σ_m	Magnetic conductivity
χ_e	Electrical suceptibility	χ_m	Magnetic suceptibility

For lossless, source-free region in space, the equations can be reduced to [1],

$$\frac{\partial E_z}{\partial y} = -\mu \frac{\partial H_x}{\partial t} \tag{2.2}$$

$$-\frac{\partial E_z}{\partial x} = -\mu \frac{\partial H_y}{\partial t} \tag{2.3}$$

$$\frac{\partial H_y}{\partial x} - \frac{\partial H_x}{\partial y} = \varepsilon \frac{\partial E_z}{\partial t} \tag{2.4}$$

where, ε, μ are material permittivity and permeability respectively, and can be combined by differentiating equation 2.2 with respect to y, equation 2.3 with respect to x and equation 2.4 with respect to t to produce,

$$\frac{\partial^2 E_z}{\partial x^2} + \frac{\partial^2 E_z}{\partial y^2} = \mu\varepsilon \frac{\partial^2 E_z}{\partial t^2} \tag{2.5}$$

By Kirchhoff's current and voltage laws, the following electrical equation can be written for the transmission line model shown in figure 2.1a [1].

$$\frac{\partial^2 V_z}{\partial x^2} \frac{(\Delta l)^2}{L} + \frac{\partial^2 V_z}{\partial y^2} \frac{(\Delta l)^2}{L} = 2C \frac{\partial^2 V_z}{\partial t^2} \tag{2.6}$$

The equivalent transmission line model is shown in figure 2.1b.

Equation 2.6 can be transformed using the relationships,

$$L = \mu \Delta l \tag{2.7}$$

$$C = \varepsilon \Delta l \tag{2.8}$$

$$E_z = -\frac{V_z}{\Delta l} \tag{2.9}$$

$$H_y = -\frac{I_x}{\Delta l} \tag{2.10}$$

$$H_x = -\frac{I_y}{\Delta l} \tag{2.11}$$

into

$$\frac{\partial^2 E_z}{\partial x^2} + \frac{\partial^2 E_z}{\partial y^2} = 2\varepsilon\mu \frac{\partial^2 E_z}{\partial t^2} \tag{2.12}$$

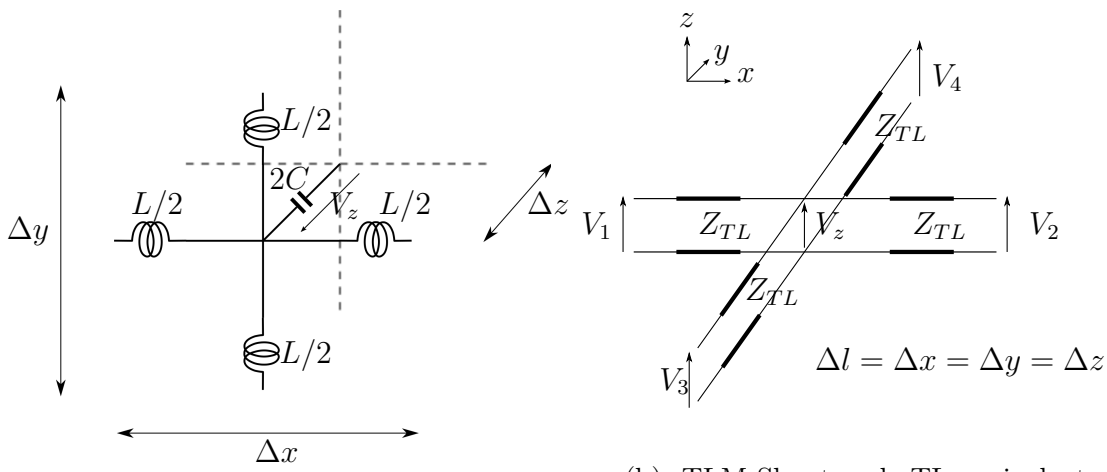

(a) TLM Shunt node electrical equivalent

(b) TLM Shunt node TL equivalent

Figure 2.1: TLM 2D Shunt Node

The analogy of equation 2.6 with equation 2.12 is noted. However, in the RHS of this equation $2\varepsilon\mu$ is found instead of the required $\varepsilon\mu$ found in equation 2.5.

Usually but not necessarily, the background medium is chosen to be free space and the inductances and capacitors in the basic shunt node correspond to free space values. Additional inductances and capacitances can be added to the shunt node structure to increase permeability and permittivity respectively as required by the modelled material [1].

If each transmission line in figure 2.1a, is chosen to consist of inductance $L/2$ and capacitance $C/2$, then the total inductance (L_T) will be L and total capacitance (C_T) will be $2C$ from figure 2.1a. Therefore, the velocity of propagation in the transmission line (u_{TL}) and the characteristic impedance of the transmission lines (Z_{TL}) can be defined using L, C [1] as:

$$Z_{TL} = \sqrt{\frac{L}{C}} \qquad u_{TL} = \frac{\Delta l}{\sqrt{LC}}$$
$$L_T = Z_{TL}\Delta t \qquad C_T = 2\frac{\Delta t}{Z_{TL}} \tag{2.13}$$

In order to match the transmission lines representing the inductors and capacitors to free space (ε_0, μ_0), the velocity of propagation in the transmission line (u_{TL}) and the characteristic impedance of the transmission lines (Z_{TL}) are chosen to be [1],

$$u_{TL} = \frac{\sqrt{2}}{\sqrt{\mu_0 \varepsilon_0}} \tag{2.14}$$

$$Z_{TL} = \sqrt{2}\sqrt{\frac{\mu_0}{\varepsilon_0}} \tag{2.15}$$

Hence, the modelled inductance per unit length ($L_T/\Delta l$) and modelled capacitance per unit length ($C_T/\Delta l$) are,

$$L_d = \frac{Z_{TL}\Delta t}{\Delta l} = \mu_0 \tag{2.16}$$

$$C_d = \frac{2\Delta l}{Z_{TL}\Delta t} = \varepsilon_0 \tag{2.17}$$

Therefore, this model represents free space.

2.1.2 Stubs for Permittivity

The optical materials used in this study are non-magnetic in nature. For the purpose of the current formulation, the materials are also assumed to be loss-free. The loss is discussed in chapter 6 along with dispersion. The dielectric permittivity can be modelled by an open terminated stub at the centre of the shunt node representing a capacitor as shown in figure 2.2.

The formula for the total capacitance as given in equation 2.13 is modified as,

$$C_T = 2\frac{\Delta t}{Z_{TL}} + \frac{\Delta t}{2} Y_s \tag{2.18}$$

where Y_s is the characteristic admittance of the added stub [1].

Hence the capacitance per unit length must be equal to the permittivity of

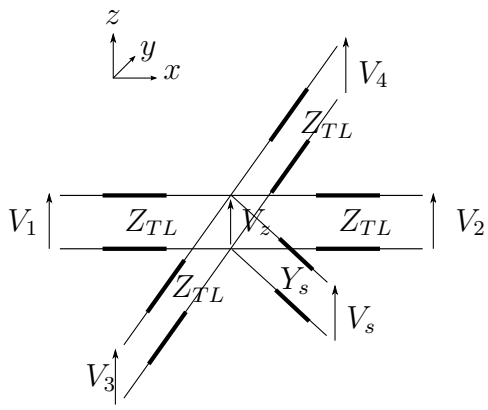

Figure 2.2: TLM Shunt node TL equivalent

the medium.

$$C_d = \frac{2\Delta t}{Z_{TL}\Delta l}\left(1 + Y_s\frac{Z_{TL}}{4}\right) = \varepsilon_0\left(\frac{Z_{TL}}{4}\right) = \varepsilon_0\varepsilon_r \tag{2.19}$$

Therefore, to model a medium of relative permittivity $\varepsilon_r = n^2$ where n is the refractive index,

$$Y_s = 4\frac{\varepsilon_r - 1}{Z_T L} \tag{2.20}$$

2.1.3 Field Calculation

The simulation domain modelled above can now be used to determine the voltage at the node when voltages are incident from the links at a given time step. Using the Thevenin equivalent of a lossless transmission line, which is twice the incident voltage in series with its characteristic impedance, the equivalent circuit can be presented as given in figure 2.3, [1].

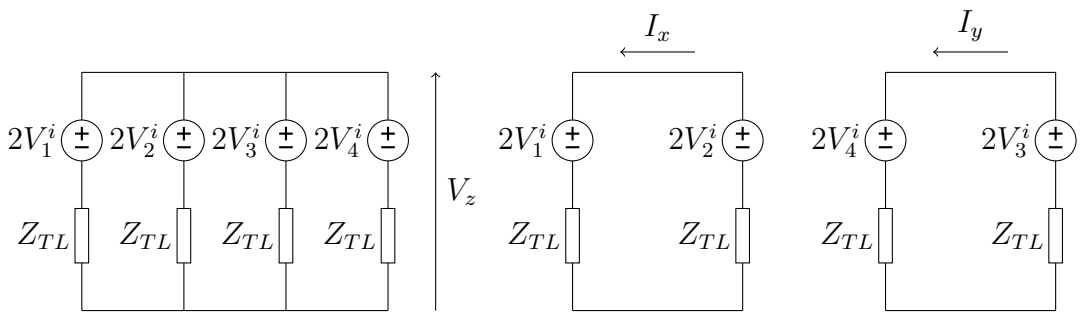

Figure 2.3: Equivalent circuits of 2D shunt transmission line network

Using Kirchhoff's voltage and current laws [1],

$$V_z = \frac{V_1^i + V_2^i + V_3^i + V_4^i}{2} \tag{2.21}$$

$$I_x = \frac{V_2^i - V_1^i}{Z_{TL}} \tag{2.22}$$

$$I_y = \frac{V_3^i - V_4^i}{Z_{TL}} \tag{2.23}$$

When a stub is added for relative dielectric permittivity, another branch with twice the stub voltage and characteristic impedance of $1/Y_s$ is added to figure 2.3. Hence, equation 2.21 is modified into equation 2.24.

$$V_z = \frac{2(V_1^i + V_2^i + V_3^i + V_4^i) + 2V_s^i Y_s Z_{TL}}{4 + Y_s Z_{TL}} \tag{2.24}$$

where V_s^i is the stub incident voltage.

2.1.4 Scattering

The reflected voltages after calculating the node voltages are given by [1],

$$V_j^r = V_z - V_j^i \tag{2.25}$$

where $j = 1, 2, 3, 4$. With the stub the additional reflected voltage into the stub is similarly given by,

$$V_s^r = V_z - V_s^i \tag{2.26}$$

2.1.5 Connection

The above describes what happens within a TLM time step. In order to connect link voltages to adjacent point in going from one time step to another time step, the connection step in TLM is defined as follows.

Let the point of interest be $(x_n,\ y_m)$, where $x_n = n\Delta l$ and $y_m = m\Delta l$. If the current time is t_k where $t_k = k\Delta t$, the connection steps for a 2D TLM mesh are,

$$V_1^i(x_n, y_m, t_{k+1}) = V_2^r(x_{n-1}, y_m, t_k) \quad V_2^i(x_n, y_m, t_{k+1}) = V_1^r(x_{n+1}, y_m, t_k)$$
$$V_3^i(x_n, y_m, t_{k+1}) = V_4^r(x_n, y_{m-1}, t_k) \quad V_4^i(x_n, y_m, t_{k+1}) = V_3^r(x_n, y_{m+1}, t_k)$$

If the node contains a capacitive stub, the stub voltage is connected simply by,

$$V_s^i(x_n, y_n, t_{k+1}) = V_s^r(x_n, y_n, t_{k+1})$$

2.1.6 TLM Matched Boundary

The connection step is defined at all points except the simulation boundary. The self-connection at the simulation boundary depends on what type of reflection is required. The simplest conditions are the open circuit and short circuit and are simply connected with the same value with the same polarity or inverted polarity respectively.

As a simple emulation of the radiation condition, a TLM matched boundary can also be used. This terminates the boundary link with an impedance equal to the wave impedance of the medium as illustrated in figure 2.4.

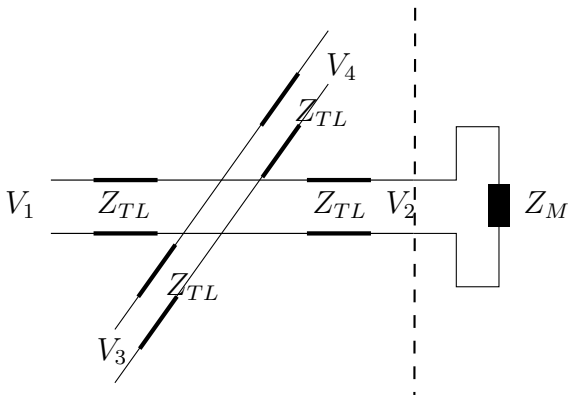

Figure 2.4: TLM Shunt node Matched Boundary

Hence, the boundary connection is defined as,

$$V_b^i(x_n, y_m, t_{k+1}) = \frac{Z_M - Z_{TL}}{Z_M + Z_{TL}} V_b^r(x_n, y_m, t_k)$$

where, Z_M is the material characteristic impedance and is equal to $Z_0 = \sqrt{\mu_0/\varepsilon_0}$ in free space.

2.2 Alternative Z transform Formulation

An alternative TLM formulation using bilinear z-transform was also presented by J. Paul in [3]. The derivation uses less of an electrical analogy and more of transmission line characteristics and a z-transform of Maxwell's equations. In this study, a 2D condensed model is used for E-type wave modelling.

2.2.1 Formulation

The formulation begins with Maxwell's equation and transforming first to the frequency domain(s-domain) as given in equation 2.1 and then using bilinear transform to transform the equation to z-domain.

The normalising in the z-domain model is slightly different from that in the electrical counterpart. In the z-domain model currents are also normalised to

act as voltages. The normalising relationships are,

$$E_z = -\frac{V_z}{\Delta l} \qquad H_{x,y} = -\frac{i_{x,y}}{(\Delta l)\eta_0}$$
$$J_{efz} = -\frac{i_{fz}}{(\Delta l)^2\eta_0} \qquad J_{mf(x,y)} = -\frac{V_{f(x,y)}}{(\Delta l)^2}$$
$$\sigma_e = \frac{g_e}{(\Delta l)\eta_0} \qquad \sigma_m = \frac{r_m\eta_0}{(\Delta l)}$$

The time domain derivative is replaced by s in the frequency domain and is normalised according to,

$$s = \frac{\bar{s}}{\Delta t} = \frac{2}{\Delta t}\left(\frac{1-z^{-1}}{1+z^{-1}}\right) \tag{2.27}$$

where $\bar{s}$ is the normalised s variable. The spatial derivative is normalised by

$$\frac{\partial}{\partial x} = \frac{1}{\Delta l}\frac{\partial}{\partial \bar{x}}$$

where $\bar{x} = x_n$ is the cell index. In the frequency domain equation 2.1 becomes,

$$\begin{bmatrix} (\bar{\nabla}\times\mathbf{i})_z \\ -(\bar{\nabla}\times\mathbf{V})_x \\ -(\bar{\nabla}\times\mathbf{V})_y \end{bmatrix} - \begin{bmatrix} i_{fz} \\ V_{fx} \\ V_{fy} \end{bmatrix} = \bar{s}\begin{bmatrix} 2V_z \\ i_x \\ i_y \end{bmatrix} + \begin{bmatrix} g_eV_z \\ r_mi_x \\ r_mi_y \end{bmatrix} + \bar{s}\begin{bmatrix} 2\chi_eV_z \\ \chi_mi_x \\ \chi_mi_y \end{bmatrix} \tag{2.28}$$

Using Stokes' theorem,

$$\begin{bmatrix} (\bar{\nabla}\times\mathbf{i})_z \\ -(\bar{\nabla}\times\mathbf{V})_x \\ -(\bar{\nabla}\times\mathbf{V})_y \end{bmatrix} = \begin{bmatrix} (V_1+V_2+V_3+V_4) \\ -(V_3-V_4) \\ -(V_1-V_2) \end{bmatrix} \tag{2.29}$$

Transforming equation 2.28 after substituting equation 2.29 to the travelling

wave format (using Thevenin equivalents) the field calculation is given by,

$$2\begin{bmatrix} (V_1+V_2+V_3+V_4) \\ -(V_3-V_4) \\ -(V_1-V_2) \end{bmatrix}^i - \begin{bmatrix} i_{fz} \\ V_{fx} \\ V_{fy} \end{bmatrix} = \begin{bmatrix} (4+g_e+\bar{s}2\chi_e)V_z \\ (2+r_m+\bar{s}\chi_m)i_x \\ (2+r_m+\bar{s}\chi_m)i_y \end{bmatrix} \tag{2.30}$$

2.2.2 Scattering

The condensed formulation has a slightly different scattering step to the scattering step given in the circuit analogy. This is mainly due to the simultaneous modelling of permittivity and permeability. The scattering step is [3],

$$\begin{bmatrix} V_1 \\ V_2 \\ V_3 \\ V_4 \end{bmatrix}^r = \begin{bmatrix} V_z+i_y-V_2^i \\ V_z-i_y-V_1^i \\ V_z-i_x-V_4^i \\ V_z+i_x-V_3^i \end{bmatrix} \tag{2.31}$$

2.2.3 Other Differences

Apart from the previously mentioned differences between the two formulations, one must keep in mind that the transmission line's characteristic impedance(Z_{TL}) in the z-domain formulation is unity. Hence, the material characteristic impedance also has to be normalised to the freespace impedance accordingly.

2.3 A TLM Implementation

2.3.1 Basic Requirements

A transmission line modelling method implementation is comprised of simple repetitive steps of scattering and connection as mentioned in the previous sections. Each of these steps is carried out for all the nodes within the domain of

interest. With the addition of excitation and field saving steps, the complete process in order can be given as,

1. Excitation of Fields
2. Field Calculations from Link/Stub Voltages
3. Save Field data as required
4. Calculate reflected Link/Stub Voltages
5. Connect adjacent nodes
6. Self connect boundary nodes

Please note that, the saving field data step (3) can be performed at any place after the field calculation step (2).

2.3.2 Requirements for a Parallel Implementation

Note that all the steps given above, with the exception of the connection step (5), can be carried out independently for each node. The connection step involves pairs of adjacent nodes along each major dimension. Therefore, the problem is parallel in each node, while inter-node communication occurs at the connection step. Therefore, the problem is parallel for any chosen domain set of $D_N = d_1, d_2, d_3, ..., d_N$ covering the domain of interest D (i.e. $d_1 \cup d_2 \cup d_3 \cup ... \cup d_N = D$), where inter-domain communication occurs at all the boundaries of the domains between nodes at the boundaries. Hence, this becomes the recipe for a parallel implementation or a multi-threaded implementation on a multi-core processor.

2.3.3 Object Oriented Requirements

Given a specific geometrical structure, a non object oriented implementation of the above mentioned steps is fairly straightforward and efficient. However,

such an implementation inevitably becomes hard to maintain, modify and extend features as required. Hence, a software engineering approach to the implementation of the TLM method should address the following.

- User configurable
- Extend for new types of materials and nodes
- Extend for new excitation source types
- Extend for new field saving and/or processing methods
- Adapt to new discretising techniques
- Adapt to new methods of node storage

In order to accomplish the above, key 'concepts' of an object oriented implementation of TLM method (or similar parallel computational electromagnetic technique) can be defined as follows:-

- Material
- Node
- Geometry shape
- Excitation Source
- Field Sink (Saving)
- Discretiser (meshing algorithm)
- Node Store (storage of nodes created by the discretiser)

Typically, the configuration of the above concepts is initially provided by the user, as illustrated in figure 2.5. Then the required excitation sources and field saving methods(sinks) are added to the simulation before executing for

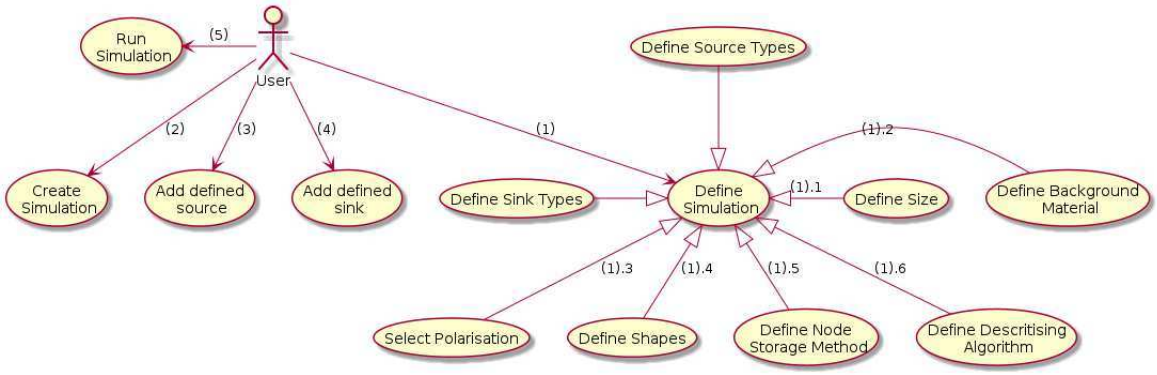

Figure 2.5: Use case diagram of the designed TLM platform

a specific time. The concepts used in the configuration are implementations of the base classes with the relationships shown in figure 2.6.

The class diagram in figure 2.6 is organised around the main simulation class which holds all information centrally and acts as the facade for the configuration and simulation. The discretiser the simulation class holds is responsible for providing information such as step time, step size and the size of the domain based on its instantiation parameters. It is also the bridge in transforming between discrete time step t_k and time value t as well as discrete space step (x_n, y_m, z_l) and space coordinates (x, y, z). This is required when non uniform meshing is used by the discretiser. Though the size of the domain is provided by the user, the discretiser might have to extend the size depending on boundary types used (e.g. Perfect Matched Layers (PML)). The discretiser also creates the nodes depending on the geometries defined in the simulation and the materials. Therefore, the discretiser is the bridge between the physical domain and structure and the internal node structure. In a parallel implementation, both simulation and discretiser must be available to all processes.

Once the node structure is determined, the instantiated nodes are stored within the node store. In a parallel implementation, the node store selects the set of nodes to work on as well as its node boundaries. All actions to be performed on nodes must be passed onto the node store for it to apply

depending on the internal ordering of the steps. This allows one to optimise the storage of a set of nodes. For multi threading, this also gives one the ability to divide the nodes into sets to be processed in parallel.

Two types of actions can be performed on nodes as defined in figure 2.6. They are independent actions which can be performed in parallel and actions which concern sets of nodes which can be performed in parallel on disjoint node sets. All steps except inter node connections fall into the former category and can be performed with very low overhead. Connection mostly concerns either two, three or six nodes in one,two, three dimensions respectively. Further, it can be generalised to use two nodes at a time only considering the link between them. Then the application can be optimised to use two nodes at a time. In one dimension it can be readily used. In two and three dimensions, the connection has to be performed for x-directed links, y-directed links and z-directed links independently. Since the connection involves two distinct types for some links (other links connect same type nodes), run time type information has to resolved for the two nodes every time with a significant overhead.

The node selector is a concept defined by the discretiser to select a set of nodes to be acted upon either based on some physical parameters or internal mesh parameters. TLM steps (i.e. field calculation, scattering, connection, boundary connection) use internal node selection, while user defined source and field sink use physical parameters. Sources such a point source, plane wave source, waveguide mode source define excitations to be performed at a certain physical location (possibly set of locations). Similarly, Field sinks are also defined to measure the field at a physical location (possible set of locations). Field sinks are the most performnance critical step beside the connection step as it possibly involves transferring a set of data over the network or to a permanent storage (such as a hard drive).

Therefore, to improve the efficiency of the software, the node store must be designed to optimally perform the connection without breaking the parallel nature of nodes. To minimise the data flow to storage when storing the field values of a large set of nodes, one could compress the data with a data storage

standard such as HDF (http://www.hdfgroup.org/).

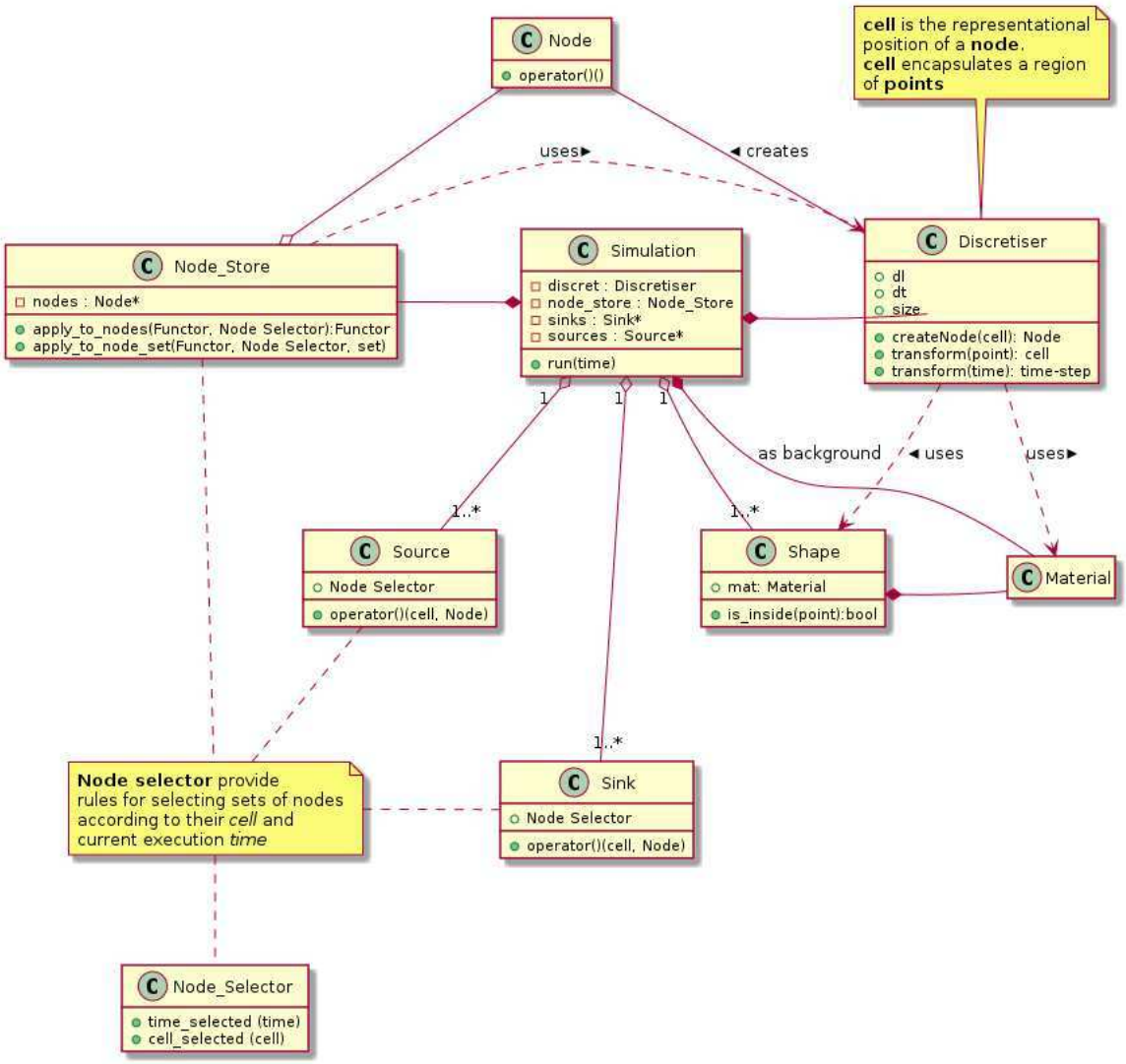

Figure 2.6: Class diagram of the TLM Platform

As shown in figure 2.7, the instantiating sequence consists of instantiating the discretiser and the node store depending on the discretiser. The net sequence illustrates a multi threaded implementation of running the simulation. Mutual exclusion (mutex) rules defined in the node store states the order of execution for a given set of nodes.

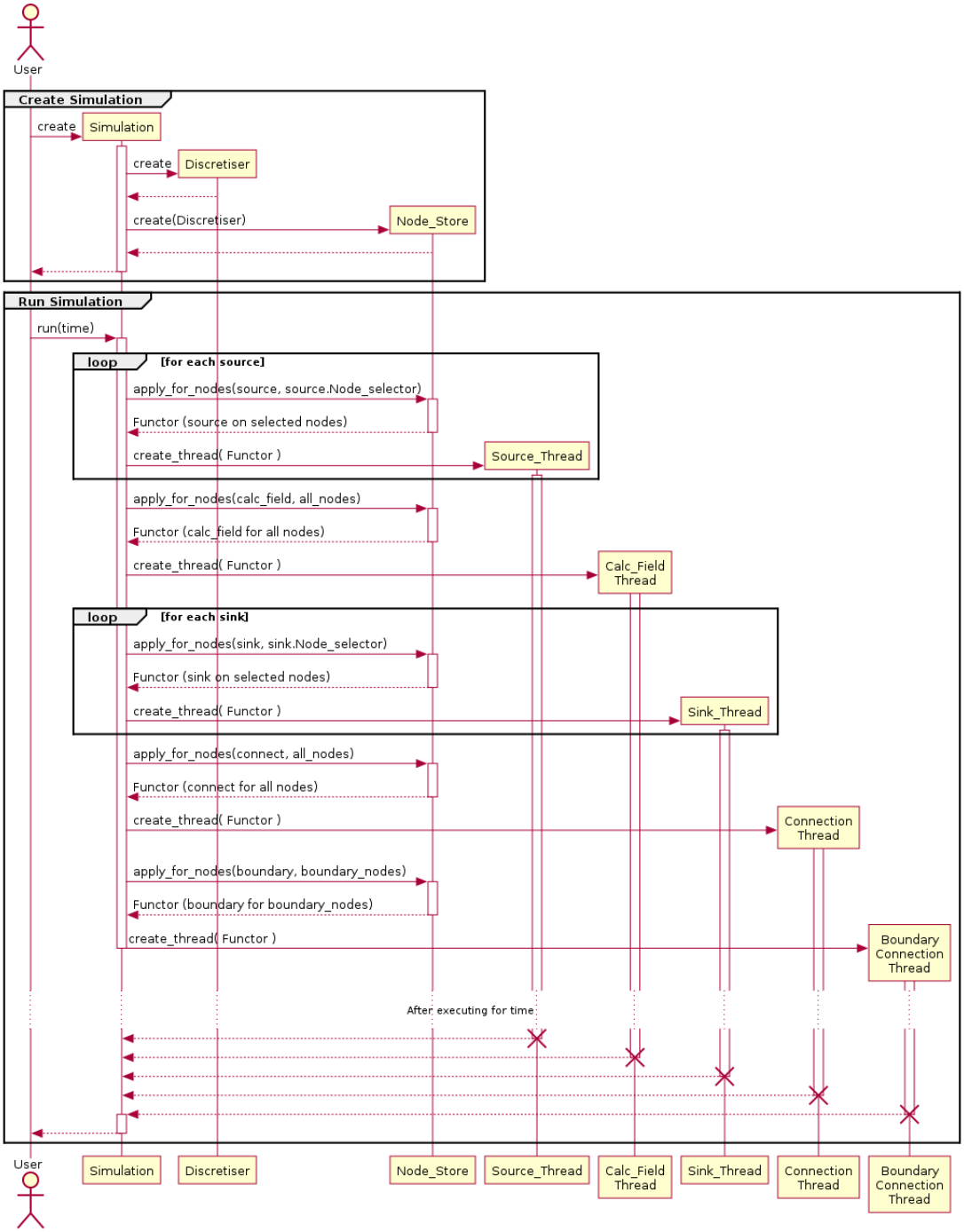

Figure 2.7: Sequence Diagram for Creating and Running a Simulation

2.3.4 OOP Hierarchy and Associated Problems

Ideally each concept could be defined as an abstract class, with a well defined interface between them.The concrete objects can be combined together at run-time according to the user configuration. However, this approach has some shortcomings.

First, the implementation is unaware of the specific types and the arrangement at compile-time, and has to depend on run time type information (RTTI) at all function calls. Yet, typically, the user configuration is defined before the program is run. The run-time type resolution involves resolution of virtual functions and affects most for small repetitive functions. This inevitably slows down the entire process severely, as the TLM process is constructed from simple repetitive steps defined for every node at every time step. This also implies that the compiler can only make local optimisation to the concept members; hence, code in-lining cannot in this case improve the performance drastically.

A second more hidden problem lies in defining the concept interface as it should include all common behaviours of the concrete concepts. This requires complex concrete concepts to either find a way around the rigid interface or change the interface, which might introduce unrelated interface functions for simpler concepts. A lot of such changes to an existing interface, makes the code lose clarity eventually becoming hard to maintain.

2.3.5 Template Meta-programming as an Alternative

The first problem of run-time type binding overhead can be eliminated by using static binding instead of run-time binding if the user configuration is available at compile time. That is the user configuration must allow the compiler to define all the concepts and their usage contexts. This however demands the removal of virtual functions and the abstract hierarchy. Hence, the user configuration should be able to define the interface between the concrete concepts rigidly. This brings the second problem into light in defining

a rigid, yet flexible enough interface, to adapt to extensions and variations mentioned earlier.

In C++, templates are used for on demand code generation, for types given by the template parameters. If the user configuration can be defined as parameters to templated concepts, the associated concrete concept can be generated by the compiler and bind them together according to the user configuration (i.e. template parameters). In this case, not all concrete implementations of a concept need be matched for all concrete implementations of another concept, as it should have been with abstract class interfaces. Only the concepts matching together can be generated according to the user configuration.

2.3.6 Computational Efficiency Comparison

In this study, TLM was implemented under three software paradigms. The first one used an imperative programming paradigm. The second implementation used object oriented programming (OOP) entirely, following the diagrams shown above. The last implmentation improved the OOP implementation with functional programming and multi threading so that all objects are statically known at compile time. In table 2.1, run times for the three methods are compared for three test configurations, as performed on a dual core Pentium processor with 4 Giga bytes of memory. The operating system used was FreeBSD 9.0 without any graphical user environment to minimise irrelevant background processes.

The first test consisted of a line source excitation entirely in freespace with a simulation domain of $10\mu m \times 10\mu m$, for a simulation time of $2000fs$. The source was excited at the centre and the field was saved throughout the simulation domain at all time steps in an HDF file with medium compression (level 6 in HDF). The second test added a dielectic cylinder of radius $r = 1.35\mu$, refractive index $n = 2.82$ at the centre of the simulation domain used in the first test. The source was excited at $(4.2\mu m, 4.2\mu m)$. The third test consisted of a core clad waveguide with core width of $0.6\mu m$, cladding width of $3\mu m$ (appears on both sizes of the core), core refractive index of 2.82, cladding

refractive index of 1.73. The length of the waveguide was $50\mu m$. The simulation domain was truncated to include only the waveguide which was excited with a line source within the core.

Table 2.1: Computational Loads for a three tests carried out with the three implementations. The tests are 1. freespace of size $10\mu m \times 10\mu m$ simulated for $2000fs$, 2. dielectric cylinder ($r = 1.35\mu m$, $n = 2.82$) in freespace of size $10\mu m \times 10\mu m$ simulated for $2000fs$, 3. dielectric waveguide ($50\mu m \times 0.6\mu m$, $n = 2.82$) in freespace with domain size of $50\mu m \times 6.6\mu m$ simulated for $2000fs$.

	Space Step (μm)	Imperative Method	OOP Method	OOP + Templates + Functional
Free Space Test	0.5	30s	221s	38s
	0.25	325s	2354s	458s
	0.125	3503s	24471s	4300s
Cylinder Test	0.5	37s	254s	47s
	0.25	423s	2606s	545s
	0.125	4523s	28946s	5587s
Waveguide Test	0.5	98s	982s	121s
	0.25	972s	9934s	1021s

As can be seen clearly, the imperative method is the most efficient program from all the tests carried out. The OOP method was about 8 times slower than the imperative method. The templated method had run-times on average about 1.5 times the imperative program. Therefore, the templated program is nearly as good as the imperative program with the added flexibility.

2.4 Conclusions

In this chapter, the formulation of TLM for two dimensional E waves was presented. The analogy of the transmission line network to the Maxwell's equations in free space were presented. Further, its technique of adding permittivity and matching boundary condition for radiating condition were discussed.

As used extensively in this study, an alternative but equivalent formulation using z-transform method was presented.

From the details of the TLM method, a software implementation based on object oriented programming was suggested. However, due to the inefficient nature of the OOP method, template meta programming was used to remove the overhead in determining objects at run time. Comparing the CPU times for some typical problems, it was understood that the templated OOP program works as well as a fairly rigid imperative program.

The next task in this study was to observe the spectral properties of optical microresonators. But, due to non trivial nature of identifying the spectral properties of high Q optical resonators, extracting resonances from a time signal is discussed before embarking on determining these properties from TLM simulations.

References

[1] C. Christopoulos, *The transmission-line modeling method: TLM*. Institute of Electrical and Electronics Engineers, 1995.

[2] R. Beurle and P. Johns, "Numerical solution of 2-dimensional scattering problems using a transmission-line matrix(numerical solution of two dimensional scattering by waveguide bifurcation, using transmission line matrix impulse analysis)," in *Institution of Electrical Engineers, Ppoceedings*, vol. 118, pp. 1203–1208, 1971.

[3] J. Paul, *Modelling of General Electromagnetic Material Properties in TLM*. PhD thesis, The University of Nottingham, 1998.

3

Extraction of Resonator Properties

This study is centred on the application of a time domain electromagnetic simulation technique to optical resonators. The effectiveness of the application can be deduced from how well the resonator properties are represented by the method. Resonant frequency and quality factors are the most fundamental characteristics of a resonator. Hence, the accuracy of resonant frequencies and quality factors of a resonator simulated by the numerical simulation method can be taken as a representative of the effectiveness of the method. However, these properties cannot be measured directly and need to be calculated either from an energy spectrum or an energy measurement over time. The latter is directly available in time domain simulations and can be converted to former by means of a Fourier transform. But before making any statements on the accuracy of the numerical simulation method, one must make sure that the resonant frequency and Q factor calculations are more accurate than the simulation method. To this end, the accuracy of calculating resonant frequency and Q factor must be known.

This chapter is dedicated to accurately extracting linear spectral properties of high Q optical resonators from a time-domain numerical simulation. Even

though the properties and methods discussed here are generally applicable to any resonator, special attention is required in the case of very high Q resonators such as optical resonators. The first section introduces the concepts of the spectral properties and sets the requirements for extracting them.

A Fourier transform based method is discussed first in an attempt to extract spectral properties. Identifying its limitations, complex exponential extraction techniques are then presented and compared, noting their strengths and weaknesses for this particular problem. All methods are then applied to an emulation of a typical numerical problem of a circular resonator, which is the subject of the next chapter.

3.1 Spectral Properties - Resonant Frequency and Q factor

The linear spectral properties of microresonators are completely determined by the geometry and the refractive index distribution inside and just outside the resonator. The spectral properties of spherical open dielectric resonators were formulated by Debye in 1909 [1]. A similar formulation, following from Maxwell's equations for spherical dielectric resonators can be found in [2]. In this technique, the vector time harmonic Maxwell's equation is reduced to a scalar wave equation on the basis of one component of the field being zero. Two such wave categories are then formed so that a magnetic component is zero (E waves) and an electric component is zero (H waves). By variable separation of the resulting partial differential equation (PDE), the fields inside and outside the resonator are written in terms of Legendre polynomials (θ distribution), sinusoidals (φ distribution) and spherical Bessel functions (r distribution) as given in equation 3.1 [2].

$$U_{mn}(r,\theta,\varphi) = \begin{cases} C^i_{mn} P^m_n(\cos\theta)\sqrt{kr}J_\nu(kr)e^{\pm jm\varphi} & (r \leq a) \\ C^e_{mn} P^m_n(\cos\theta)\sqrt{k_0 r}H^{(1)}_\nu(k_0 r)e^{\pm jm\varphi} & (r > a) \end{cases} \tag{3.1}$$

where U_{mn} is the scalar potential of the mode number combination (m, n), C^i_{mn}, C^e_{mn} are the complex amplitude inside and outside the sphere of mode (m, n), P^m_n is the Legendre polynomial of order (n, m), $k = k_0\sqrt{\varepsilon_r}$ is the wave number within the sphere, k_0 is the free space wave number, a is the radius of the sphere, (r, θ, φ) are the spherical coordinates and $\nu = m + \frac{1}{2}$.

By applying boundary conditions to the general solution given in equation 3.1, a characteristic equation in terms of k_0 can be obtained, as given in equation 3.2 [2].

$$\frac{\left[\sqrt{ka}J_\nu(ka)\right]'}{\sqrt{ka}J_\nu(ka)} = \frac{\left[\sqrt{k_0a}H^{(1)}_\nu(k_0a)\right]'}{\sqrt{k_0a}H^{(1)}_\nu(k_0a)} \tag{3.2}$$

where a prime denotes a total derivative in terms of ka or k_0a.

3.1.1 Resonant Frequency

Therefore, there exists an infinite number of discrete frequencies related to the real parts of the roots k_0 of the characteristic equation known as the *resonant frequencies* f_r ($f_r = \Re\{k_0\}c/2\pi$, where c is the phase velocity of light in vacuum), at which the resonator will store optical energy in fields of the form given by equation 3.1. At all other frequencies optical power within the resonator (exited from outside or generated inside) will be scattered storing little or no energy. Experiments towards the end of 1970s have confirmed the existence of such optical resonances. In one such prominent experiment, the levitation of silicone oil droplets with radiation pressure induced by a dye-laser [3] was studied. In this experiment, the radiation force required to levitate the droplets increased sharply due to the scattering of optical power at some specific frequencies. The study confirmed that these frequencies closely resemble the resonant frequencies of the oil droplets calculated from Mie-Debye scattering theory [3].

3.1.2 The Q factor

The complex nature of the roots $k_0 = k_{r0} + jk_{i0}$ of the characteristic equation 3.2, give rise to the decaying nature of the resonances in the time domain [2]. This is further illustrated in figure 3.1. In the time domain it is a decaying oscillation (figure 3.1a) while in frequency domain (figure 3.1b), it takes the shape of a Lorentzian function.

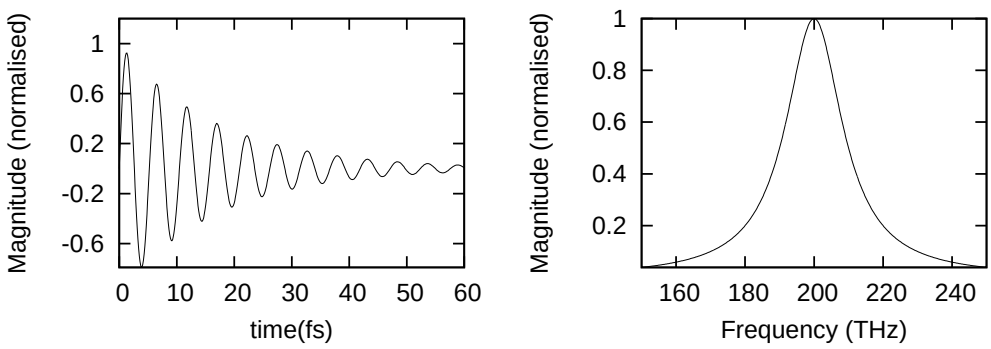

(a) Resonance in the time domain (b) Resonance in the frequency domain

Figure 3.1: A typical resonance $k_0 = k_{r0} + jk_{i0}$

Q factor is defined in many ways depending on the problem at hand. When defined for energy, the Q factor is the ratio between energy stored and energy dissipated. When defined for the frequency domain, it is the bandwidth relative to the resonant frequency. An approximate expression in the frequency domain for Q factor is given by [4],

$$Q = \frac{f_r}{\Delta f} \tag{3.3}$$

where Δf is the half power bandwidth of the resonance. This is invaluable in most experiments where the frequency response is directly available. The more exact definition is given by equation 3.4 [5].

$$Q = \frac{f_r}{2f_i} \tag{3.4}$$

where f_i is the imaginary part of the complex frequency $f = \frac{k_0 c}{2\pi} = f_r + jf_i$.

The importance of Q-factor is several fold. In the frequency domain, it is a measure of the frequency selectivity as mentioned previously. In the time domain, the Q factor is an indication of the length of the transient in the resonator. In other words, when light coupled into a resonator, Q factor is related to the length of time over which the resonator is capable of holding a significant amount of optical power without radiating or absorbing. In a typical spherical optical resonator, light transients as long as $2.7\mu s$ at $633nm$ have been observed [6]. The length of the transient is known as the *resonator ring down time* or *lifetime of light energy*(τ) in the resonator. Hence, the Q factor is also defined by [6],

$$Q = 2\pi f_r \tau \tag{3.5}$$

3.1.3 Extracting Resonant Frequency and Q factor

As mentioned in the previous subsection, the resonant frequency and Q factor information is present in both time domain and the frequency domain. In frequency domain data, accurately extracting these two properties is a matter of resolving enough in frequency in order to apply equation 3.3. In order to apply equation 3.4 to time domain data, one must extract a complex frequency $f_r + jf_i$. However, extracting resonant frequencies and Q factors from a limited time signal is proven to be a non trivial task [7, 8, 9, 10], even when these can be observed in a Fourier transform of the time signal.

High Q cylindrical and spherical dielectric resonators have closely spaced resonant frequencies with Q factors as high as 10^9 [6]. In order to accurately resolve these from time domain data, long time signals are required. In time domain simulations, due to heavy computational demands, very long simulations of high Q 3D resonators using time domain numerical methods is highly impractical. Therefore, methods of resonance frequency extraction from limited length time domain signals are compared in the next few sections in the context of high Q optical resonators.

3.2 Fourier Transform Fitting Technique

In this section, a method for extracting resonances with a known function fit to the Fourier transform of a time signal is presented. Then, its limitations when extracting one complex frequency and two closely spaced complex frequencies from a time signal are discussed.

A resonant peak in the frequency domain corresponds to a Fourier transform of a sinusoid truncated by a rectangular time window [9]. Hence, the resonance line shape will be the frequency domain representation of the sinusoid convoluted by the sinc function. In the case of an undamped sinusoid (i.e. infinite Q factor), the peak assumes the shape of a sinc function [7, 8, 9]. This is explained by the Fourier transform of an undamped sinusoid, a Dirac delta function ($\delta(f - f_r)$) convoluted by the sinc function, resulting in a sinc function centred at f_r. For a damped sinusoid (i.e. finite Q factor), the line shape will be a Lorentzian [2], the width of which is determined by the Q factor, convoluted by a sinc function. The shape of the resulting function is sought next in order to make an appropriate fitting function.

3.2.1 Fourier Transform Fitting Method

Let the continuous damped sinusoidal signal be,

$$\mu(t) = Ae^{2\pi j(f_r + jf_i)t} \tag{3.6}$$

where A is the complex amplitude, which also includes phase delay. Using Fourier Transform $\mathcal{F}(f)$ of a function $x(t)$ is defined as,

$$\mathcal{F}(f) = \int_{-\infty}^{\infty} x(t)e^{-j2\pi ft}dt \tag{3.7}$$

The magnitude of the Fourier transform of signal in equation 3.6 of length T is,

$$\begin{aligned} |\mathcal{F}(f)| &= \left| \int_0^T \mu(t) e^{-j2\pi ft} dt \right| \\ &= |A| \left| \frac{1 - e^{-2\pi f_i T} e^{-j2\pi(f-f_r)T}}{2\pi f_i + j2\pi(f - f_r)} \right| \end{aligned} \tag{3.8}$$

In equation 3.8, the magnitude of the numerator represents a periodic function of amplitude determined by $f_i T$ and oscillation period determined by $1/T$. Hence, the width of the main lobe of the sinc function is determined by $1/T$, whereas the height of the side lobes of the sinc function is determined by $f_i T$. When $f_i T >> 1$, the amplitude of the oscillations will be small and the frequency domain resembles a Lorentzian function. When $f_i T << 1$, the amplitude of the oscillations will be large indicating that the frequency domain resembles a sinc function.

When extracting high Q resonances from small length time signals, the second condition $f_i T << 1$ becomes true; hence by allowing a uniform noise floor ε, one obtains,

$$|\mathcal{F}(f)| = \frac{\alpha \left| 1 - e^{-2\pi j(f - f_r - f_i j)T} \right|}{\sqrt{f_i^2 + (f - f_r)^2}} + \varepsilon \tag{3.9}$$

where $\alpha = |A|/2\pi$. If the discrete Fourier transform data is fitted to this function with sufficient number of points for the fitting algorithm to converge, the resonant frequency (f_r) and the Q factor (ratio of $f_r/2f_i$) can be estimated from a time signal of an isolated resonance.

3.2.2 Extracting an Isolated Resonance from Fourier Transform

An illustrative damped sinusoidal time signal with a complex frequency of $(193.548 + j0.00097)THz$ ($1.55\mu m$ wavelength in free space and $Q \approx 10^6$) of time length $65536fs$ (12688 cycles) was converted to the frequency domain

by fast Fourier transform (FFT) and the frequency samples within the interval $(192.5, 194)THz$ were fitted using a least square fitting (LSF) algorithm. The fitting accuracy was increased by padding the time signal with zeros to increase the number of frequency samples within the interval, yet maintaining the underlying Fourier transform function of the signal truncated by the rectangular window.

The fitting algorithm used was Lavenberg-Maquardt linear least square fitting algorithm [11]. The fitting process requires careful attention in setting the initial parameters. This is mostly due to the nature of the sinc function. If the resonant frequency is set at the correct position, the other parameters (i.e. amplitude, damping and noise) tend to adjust appropriately. Therefore, setting the resonant frequency is important to the fitting algorithm. This however is not a tedious task as the resonant frequency can be set by observing the line shape, because a curve shift can be observed for small variations of resonant frequency. As illustrated in figure 3.2, which shows the frequency domain data of a damped sinusoid along with a fitting curve of which the frequency has a 0.001THz error compared to the signal represented by the data. With the available resolution on paper, one can deduce that the actual frequency of the data is slightly higher. Therefore, the accuracy of the resonant frequency estimation for a noiseless isolated resonance depends only on how far one can zoom in to see the overall shift between the fitted curve and the data points.

The fitting results are presented along with a continuous Fourier transform of the truncated time signal (equation 3.9 where $\varepsilon = 0$), in figure 3.3 with corrected resonant frequency. The error in resonant frequency was less than 0.0005%, while the error in Q factor was less than 1%. The same form of signal but with higher Q factors was fitted similarly to observe a limitation of extracting Q factor. The results are presented in table 3.1.

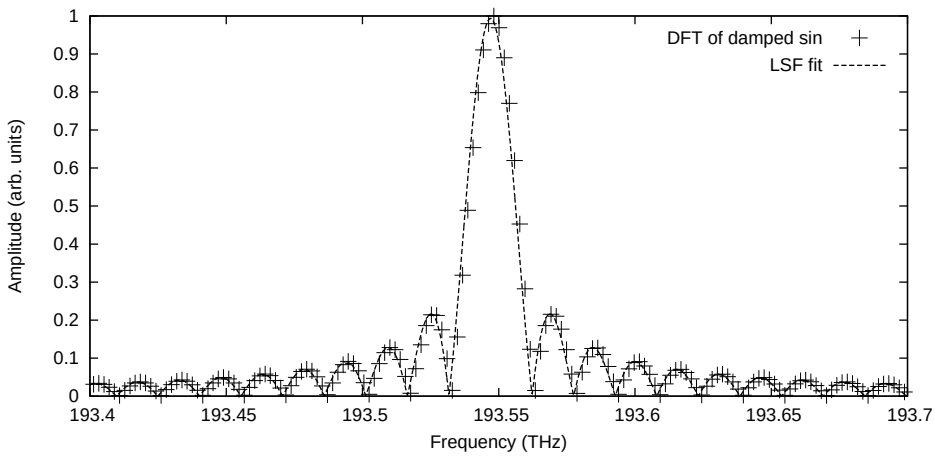

Figure 3.2: The resonance function (LSF) fit to a discrete Fourier transform of a damped sinusoidal time signal of 193.548THz and Q of 10^6(cross) by setting the resonant frequency at 193.547THz (with 0.001THz error).

Table 3.1: Results of extracting isolated high Q resonances of resonant frequency $f_r = 193.548THz$ and a signal length of $T = 65536fs$.

Q factor	Estimated Q factor
10^6	1.00×10^6
2×10^6	1.96×10^6
5×10^6	4.50×10^6
8×10^6	6.33×10^6
10^7	7.08×10^6
5×10^7	1.02×10^7
10^8	1.03×10^7
10^9	1.03×10^7

According to table 3.1, beyond a Q factor of 5×10^6, the Q factor extraction degrades heavily. Beyond a Q factor of 5×10^7, the result does not vary with increasing Q factor producing the limit of $f_iT < 0.0025$ for accurate extraction of the Q factor. The reason for the limitation can be explained with the aid of figure 3.4, which shows the frequency domain representations

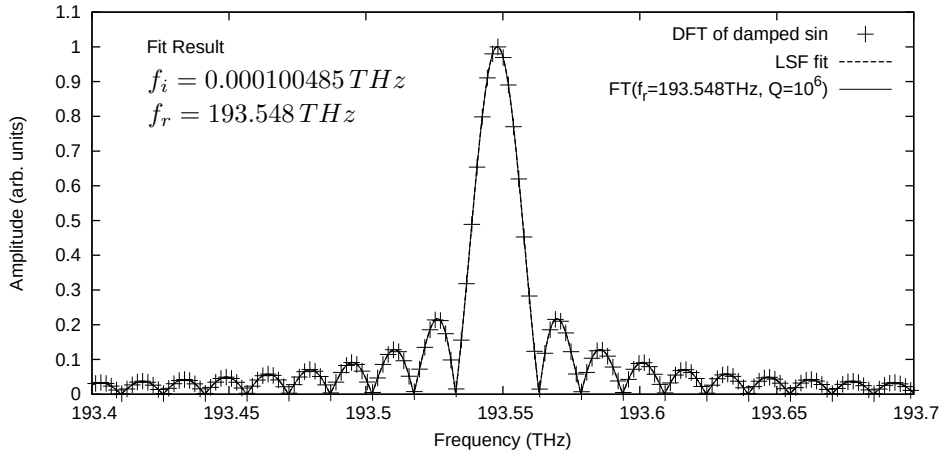

Figure 3.3: The resonance function (LSF) fit (dashed) to a discrete Fourier transform of a damped sinusoidal time signal of 193.548THz and Q of 10^6(cross), and the corresponding continuous Fourier transform of the damped sinusoidal (solid). Note: the continuous Fourier transform coincides with the fitted function.

of four resonances, each differing only in Q factor.

In figure 3.4, the Fourier transforms of signals with Q factors of 10^6 and 10^7 are indistinguishable to the naked eye. To the fitting algorithm, any Q factor beyond 5×10^7 is indistinguishable. The only difference between the Fourier transforms of signals of Q factors 10^6, 10^5 are at the nulls near the centre. This indicates that beyond a Q factor of 5×10^7 for a time signal of $65536fs$ the Fourier transform becomes a sinc function with a shape governed by the rectangular window width. Hence, beyond this limit Q factors extracted from Fourier transforms of time signals do not relate to the underlying Q factor of the signal. This limit depends on the time length of the signal T and can be increased by increasing the time length. When αT is close to its limiting value, the Fourier transform has characteristics of both Lorentzian and sinc functions and can still be used to extract the Q factor with reasonable accuracy. If otherwise, the Fourier transform takes the shape of a Lorentzian and, as table 3.1 confirm, can be used to extract Q factor with high accuracy.

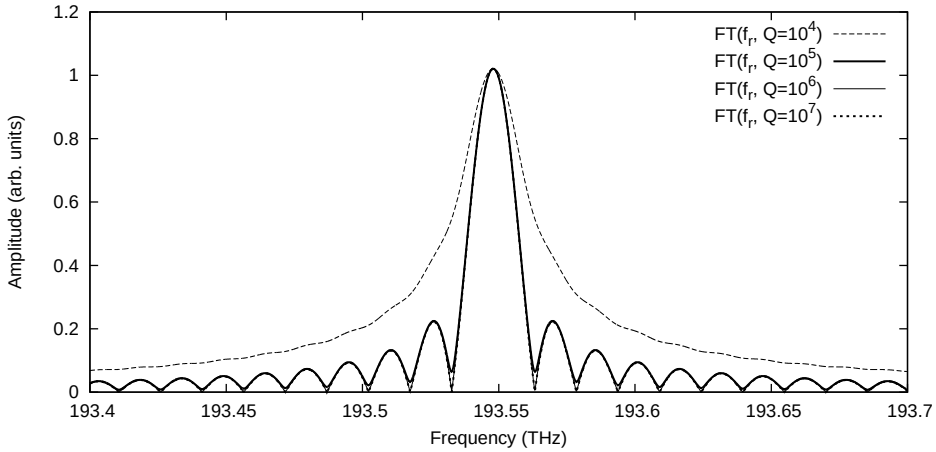

Figure 3.4: Fourier transforms of signals of length $65536fs$ and resonant frequency $f_r = 193.548THz$ and varying Q factors of 10^4 (dashed),10^5 (thick solid), 10^6 (solid), 10^7 (thick dotted).

3.2.3 Extracting Two Closely Spaced Resonances

In addition to accurately extracting an isolated resonance in practical applications, resonance extraction techniques must be able to resolve two closely spaced resonances. If the frequencies are sufficiently far apart, the frequency domain samples can be separated and two fittings can be performed independently.

In order to find a limiting condition for two single line shape fittings, resonant frequency and Q factor were extracted from a time signal of two resonances, with varying separation between the two resonances (f_{sep}), keeping one resonance at $193.548THz$ of $Q = 2 \times 10^5$.

In order to separate the two resonances by programmable means, one could identify the peaks by visiting data points in order. However, this has to be done before padding the time signal, after which humps related to the underlying sinc function appear. In addition, one can no longer interpret the resonant frequency of each resonance by merely observing the Fourier transform. Hence, only an educated guess can be provided as the initial resonant frequency parameter for the fitting algorithm. This is due to the

leakage from the other resonance as explained below.

Figure 3.5 illustrates the extraction of two peaks separated $10\Delta f$, $5\Delta f$ and $2\Delta f$ respectively. Even though spectral leakage (effect of the presence one frequency component to other components in a Fourier transform [12]) can be observed in $10\Delta f$ and $5\Delta f$ separations, the fitting processes is not very much affected, as the main lobe is intact. However, when the separation is $2\Delta f$, even the main lobe is affected degrading the ability to resolve for resonant frequency. The error in frequency and Q factor of the varying resonance ($Q = 2 \times 10^5$) are presented in figure 3.6.

Until the separation is about one DFT frequency interval Δf (i.e. $1/T$), the resonant frequency could be obtained with high accuracy. The Q factor however degraded rapidly when the separation was decreased according to figure 3.6, which shows the percentage errors of estimated resonant frequencies and Q factors, when the separation is varied. This is due to the spectral leakage from the resonances. The means of reducing spectral leakage is to employ window functions with larger dynamic range(i.e. smaller side-lobes). But all other window functions compared to the rectangular window used here have lower frequency resolution, compromising the separation altogether and merging the two high Q resonances into one lower Q resonance [12].

When the resonant frequency separation is between Δf and $0.5\Delta f$, the DFT displays two combined humps as illustrated in figure 3.7a, but the centre of each hump tends to shift from its actual resonant frequency due to severe spectral leakage. Even multiline fitting failed to extract the resonant frequency properly in this range, as confirmed by Feit *et. al* [9]. Below the seperation of $0.5\Delta f$, the resonances morph into one resonance as illustrated in figure 3.7b.

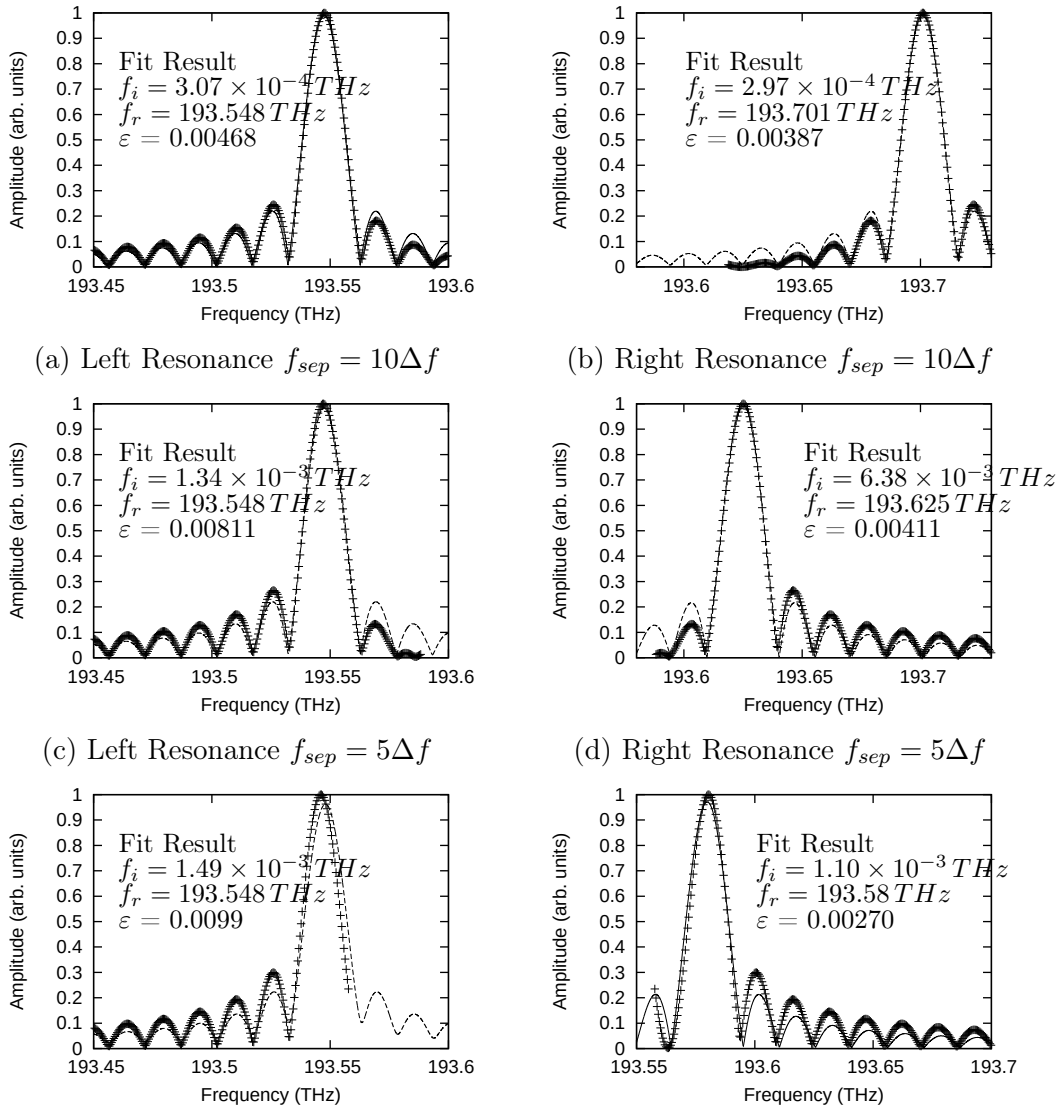

(a) Left Resonance $f_{sep} = 10\Delta f$

(b) Right Resonance $f_{sep} = 10\Delta f$

(c) Left Resonance $f_{sep} = 5\Delta f$

(d) Right Resonance $f_{sep} = 5\Delta f$

(e) Left Resonance $f_{sep} = 2\Delta f$

(f) Right Resonance $f_{sep} = 2\Delta f$

Figure 3.5: Fitting of two resonances both of $Q = 2 \times 10^5$ separated by f_{sep}, keeping the lower resonant frequency fixed at $f_r = 193.548THz$. The Fourier transform is obtained from a $65536fs$ long signal padded with zeros to obtain more points. FFT samples are denoted as (+) and the Fitted function as (-)

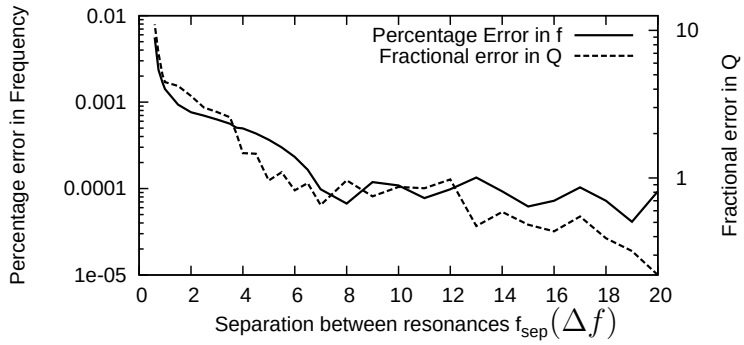

Figure 3.6: Error in extracted resonant frequency and Q factor of one of two closely spaced resonances using two independent single-line fittings, against the separation in frequency. $\Delta f = 1/T$ where $T = 65536fs$. One resonance was fixed at $193.548THz$ and both have a Q of 10^5.

3.3 Alternative Methods of Resonant Frequency Extraction

As seen previously, in the time domain representation, a resonance can be represented completely by a complex exponential (or damped sinusoidal). When fitting algorithms process the time signal without transforming the signal into the frequency domain, the limitation in extracting Q factor due to sinc convolution is lifted. However, the fitting for all components has to be accomplished simultaneously. The exponential terms of the fitting problem makes the problem a demanding one. There exists techniques to either reduce the fitting problem into a more manageable linear fitting problem or reduce the number of components acted upon at one time. Some of these methods are briefly discussed in this section.

3.3.1 Matrix Pencil Method

The matrix pencil method(MPM) is a non-iterative approach to solving the nonlinear least squares problem involving complex exponentials [13]. Let the

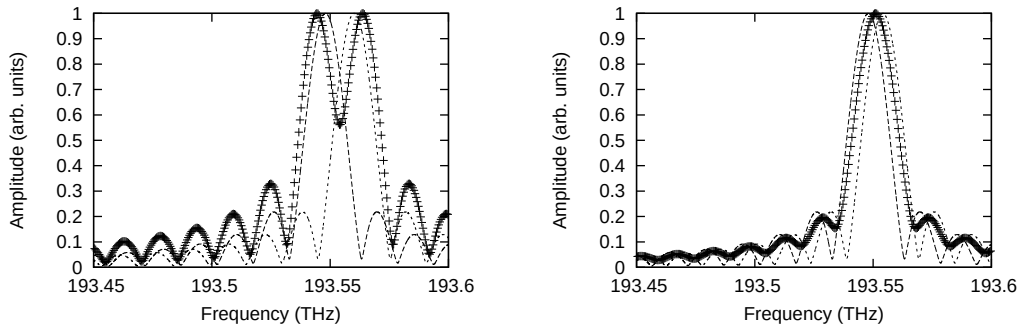

(a) Left Resonance $f_{sep} = 0.8\Delta f$ (b) Right Resonance $f_{sep} = 0.4\Delta f$

Figure 3.7: Fitting of two resonances both of $Q = 2 \times 10^5$ separated by f_{sep}, keeping the lower resonance at $f_r = 193.548THz$. The Fourier transform is obtained from a $65536fs$ long signal padded with zeros to obtain more points. FFT samples are denoted as (+) and Underlying Line Shapes as dashed and dotted.

input signal be $\mathbf{y} = \{y_0, y_1, \ldots, y_{N-1}\}$ N samples contaminated with noise. The signal is prefiltered using Singular Value Decomposition after making a matrix Y from shifted columns of $\mathbf{y}$,

$$Y = \begin{bmatrix} y_0 & y_1 & \cdots & y_L \\ y_1 & y_2 & \cdots & y_{L+1} \\ \vdots & \vdots & \ddots & \vdots \\ y_{N-L-1} & y_{N-L} & \cdots & y_{N-1} \end{bmatrix}_{(N-L)\times(L+1)} \tag{3.10}$$

where L is the pencil parameter chosen arbitrarily to be larger than the number of unique complex sinusoids in the signal (M) [13]. Hua *et. al* have shown that if the pencil parameter L, is kept between $N/3$ and $2N/3$, the method is immune to a SNR of $20 - 26dB$ [14]. The highest noise immunity is achieved at the extremes of the given range [14]. In this work L is chosen to be $\lfloor N/2 \rfloor$. Singular value decomposition is carried out on Y resulting in,

$$Y = U\Sigma V^H \tag{3.11}$$

where U, V are unitary matrices containing eigenvectors of YY^H and Y^HY. $\Sigma = diag\{\sigma_0, \sigma_1, \ldots, \sigma_{min(N-L,L+1)} \,|\, \sigma_i > \sigma_{i+1}\}$ contains singular values of Y. By comparing the values of Σ, the most significant M number of σ values are preserved while making insignificant values zero. M is selected so that $\sigma_M/\sigma_0 < 10^{-4}$. Let the filtered singular values be $\Sigma' = diag\{\sigma_0, \sigma_1, \ldots, \sigma_{M-1}\}$ and right singular vectors $V' = \{\mathbf{v_0}, \mathbf{v_1}, \ldots, \mathbf{v_{M-1}}\}$, where $\mathbf{v_i}$ are the column vectors of V.

Matrices V_1' and V_2' are made from V' by deleting the last row and the first row respectively. The filtered pencil of materices Y_1' and Y_2' is made as,

$$Y_1' = U\Sigma' V_1'^H \tag{3.12}$$

$$Y_2' = U\Sigma' V_2'^H \tag{3.13}$$

The generalised eigen value of Y_1' and Y_2' are the complex eigenfrequencies of the signal. The same can be obtained by the eigenvalues of matrix $\{V_1'^H\}^+\{V_2'^H\}^+$. where $^+$ denotes psuedo inverse defined as $\{A\}^+ = \{A^HA\}^{-1}A^H$.

A comparison between the matrix pencil method and the original Prony estimation method is given in [13, 14], and shows that despite the common formulation MPM is superior in terms of noise immunity.

3.3.2 Modified Prony Estimation

Prony's method of extracting complex exponentials from a time signal is a well known iterative least square fitting method. However, the method does not converge, or provides inconsistent results in the presence of noise [15]. Osborne and Smyth have developed and generalised a modified Prony approach addressing these issues [16, 17, 18].

Let the noiseless signal $\boldsymbol{\mu} = \{\mu_0, \mu_1, \ldots, \mu_{N-1}\}$ is a combination of complex

exponentials,

$$\mu_i = \sum_{k=1}^{p} \alpha_k e^{-\beta_k t_i} \tag{3.14}$$

where α_k, β_k are generally complex, and $t_i = i/N$ is the normalised time.

Given a sampled time signal with Gaussian noise with zero mean ε_i,

$$y_i = \mu_i + \varepsilon_i \tag{3.15}$$

the modified Prony method estimates the function $\mu(t)$ that satisfies a constant coefficient differential equation of order p.

$$\sum_{i=1}^{p+1} \gamma_i \mathfrak{D}^{i-1} \boldsymbol{\mu} = 0 \tag{3.16}$$

where $\mathfrak{D}$ is the differential operator.

The equation can be represented in a difference equation as,

$$\sum_{i=1}^{p+1} \gamma_i \Delta^{i-1} \boldsymbol{\mu} = 0 \tag{3.17}$$

where,

$$\Delta = N(II - I) \tag{3.18}$$

$$II = \begin{bmatrix} 0 & 1 & 0 & \dots & 0 \\ 0 & 0 & 1 & \dots & 0 \\ \vdots & \vdots & \vdots & \ddots & \vdots \\ 1 & 0 & 0 & \dots & 0 \end{bmatrix} \tag{3.19}$$

The method estimates the complex constant coefficients $\boldsymbol{\gamma} = (\gamma_0, \gamma_1, ..., \gamma_p)$, so that the derivative of the reduced sum of squares with respect to the complex amplitudes α_j of the fitted complex exponentials, $\dot{\psi} = 2B_\gamma(\gamma)\gamma$ is as close to

zero as possible.

$$B(\gamma)_{ij} = \mathbf{y}^T X_{\gamma i}(X_\gamma^T X_\gamma)^{-1} X_{\gamma j}^T \mathbf{y} - \mathbf{y}^T X_\gamma (X_\gamma^T X_\gamma)^{-1} X_{\gamma i}^T X_{\gamma j} (X_\gamma^T X_\gamma)^{-1} X_\gamma^T \mathbf{y} \tag{3.20}$$

where, X_j is the leading $(n-p)$ columns of C_j.

$$C_j = \left(\sum_{k=1}^{p+1} \Delta^{k-1} \right)^T \tag{3.21}$$

$$X = \sum_{k=1}^{p+1} \gamma_k X_k \tag{3.22}$$

The matrix X is a Toeplitz banded matrix where the first $p+1$ elements of the first column is given by,

$$\mathbf{c} = \begin{bmatrix} 1 & -1 & 1 & \dots & (-1)^p \\ & 1 & -2 & \dots & (-1)^p p \\ & & \ddots & \ddots & \vdots \\ & & & 1 & -\begin{pmatrix} p \\ 1 \end{pmatrix} \\ & & & & 1 \end{bmatrix} \begin{bmatrix} 1 & & & \\ & N & & \\ & & \ddots & \\ & & & N^p \end{bmatrix} \boldsymbol{\gamma} \tag{3.23}$$

The matrix B can be formed efficiently as follows[16] : From matrix Y.

$Y = (X_1^T \mathbf{y}, \dots, X_{p+1}^T \mathbf{y})$	Matrix does not depend on γ
$M = (X^T X)^{1/2}$	The lower Cholesky factor - banded
$Z = M^{-1} Y$	Banded Matrix Multiplication
$\mathbf{v} = M^{-T} Z \boldsymbol{\gamma}$	
$V = (X_1 \mathbf{v}, \dots, X_{p+1} \mathbf{v})$	
$B = Z^T Z - V^T V$	

After forming B, its eigenvector is taken as new $\boldsymbol{\gamma}$ and is iterated until its eigenvalue is close to zero as possible for the precision of floating point values used. The eigenvector of $Y^T Y$ is used as the initial $\boldsymbol{\gamma}$.

The roots of the characteristic polynomial $p_\gamma(z) = 0$ of the differential equation, are the complex frequencies β_j [18]. In order to convert them to the time/frequency scale of the input signal,

$$\zeta_i = -\frac{1}{2\pi\Delta t}\ln\left(1+\frac{\beta_i}{N}\right) \tag{3.24}$$

This formulation based on the constant coefficient differential equation, known as the "difference formulation", has a limitation in forming matrix B from differencing the input signal y. When calculated with 64-bit precision, a non-negligible amount of subtractive cancellation occurs during the differencing[18], requiring algorithms with adjustable precision depending on both the number of samples N and p. Therefore, when extracting multiple resonances from the difference method, a precision of more than $log_2(N^P)$ bits was used in this implementation, when applying recursive differencing to the input signal y and when calculating the Choleski factorisation required in the process of calculating B.

An alternative formulation known as the "recurrence formulation", derived from a constant coefficient difference equation, does not suffer this limitation due to precision[18].

By approximating the difference by a shift operation [18], equation 3.17,

$$\sum_{i=1}^{p+1} \delta_i I I^{i-1}\boldsymbol{\mu} = 0 \tag{3.25}$$

This formulation becomes simpler as the recurrance prony parameters $\boldsymbol{\delta} = \{\delta_1, \delta_2, \ldots, \delta_{p+1}\}$ are directly present in the banded Toeplitz matrix X as $\mathbf{c}$.

The method for calculating $B(\delta)$ is similar to that of $B(\gamma)$, only simpler because $X_i^T\mathbf{y}$ are simply $\mathbf{y}$ shifted by i. The downside of the recurrance method is that for large N and p, the problem becomes ill-conditioned because the roots of the characteristic polynomial become very close to unity in the "recurrence formulation" [18].

3.3.3 Harmonic Inversion

Harmonic inversion by filter diagonalisation is a method first developed by Wall and Neuhauser[10] and later developed by Mandelshtam and Taylor[19]. The method filters the time signal using a windowed DFT to band limit ($\Delta\omega$) the signal, so that only 50 to 200 damped exponentials are present within the chosen frequency band ($[\omega_0 - \Delta\omega, \omega_0 + \Delta\omega]$). The signal is then shifted by $-\omega_0$ in the frequency domain, so that the resulting signal is centred at zero frequency. The frequency domain signal is then inverted to the time domain by an inverse discrete Fourier transform to obtain the band limited decimated complex time signal. Frequency extraction is then carried out by methods such as Prony's method, direct signal diagonalisation or Pade approximant. In this study, 'haminv' – an implementation using direct signal diagonalisation – available on the internet at http://ab-initio.mit.edu/harminv was used. A detailed formulation of the method is given in [10, 19] was used in the work undertaken here.

3.4 Comparison of Frequency Extraction Methods

In comparing the frequency extraction methods discussed in section 3.3, the extraction of an isolated high Q resonances in the presence of noise is the simplest, but nonetheless important, task. Time domain numerical methods such as the Finite Difference Time Domain(FDTD) and Transmission Line Modelling(TLM) methods are known to introduce unwanted noise via mesh dispersion[20, 21] and mesh boundaries[22]. Noise also arises from simulation domain boundaries (usually perfectly matched layers). These effects are discussed separately in chapter 4.

3.4.1 Extracting an Isolated Resonance

In order to identify the limitation of extracting resonances in the presence of noise, random noise of known strength was added to a time signal of a damped sinusoid, in the form given by equation 3.6, of a known frequency of $193.548THz$ ($1.55\mu m$ free-space wavelength) and varying Q factors ranging from 100 up to 10^8. The random noise was generated with a normal probability density function with varying strengths down to a SNR of $40dB$.

Signal Parameters

Results pertaining to four noise levels - namely $100dB$, $80dB$, $60dB$ and $40dB$ are discussed in the following sections. The noise values were generated from a Gaussian random distribution with zero mean and a standard deviation of 10^{-5}, 10^{-4}, 10^{-3} and 10^{-2} times the amplitude of the sinusoidal signal for the respective noise levels. The random number distribution used was Mersenne Twister psuedo random number generator, the cycle length of which is about 10^{6000} [23].

Under noise, all of these methods provide different values for different signals. Hence, a single reproducible value cannot be provided for a given set of signal parameters. A statistical parameter representing the central value and its dispersion (in statistical distribution sense) over many signals with the same signal parameters produces a better picture of the strengths and weaknesses of these methods. Median was used as the measure of central tendency, while inter-quartile range was used as the measure of statistical dispersion about the median. These two robust statistical measures together indicate the accuracy of extracting each parameter from a given time signal with a known signal to noise ratio.

In this section, the isolated resonance was extracted from the time signal formed as discussed above. All methods were given 500 double precision floating point samples of the time signal sampled at $1fs$ increments. 100 such signals were generated from the same sinusoidal signal, by adding random numbers drawn from the same statistical dispersion, to carry out the

statistical analysis.

Results with Noise

The medians of estimated resonant frequencies of all methods at all noise levels were at $193.548THz$ indicating that methods have no bias in extracting resonant frequencies. Therefore, given enough number of time responses of the same resonator with SNR more than 40dB, one could statistically evaluate the actual resonant frequency. Further, the statistical dispersion of resonant frequencies was negligible ($< 1e-8\%$) for all methods at $-100dB, -80dB$ noise levels. At $-60dB$ only the harmonic inversion method had an accountable statistical dispersion (still low at $2 \times 10^5\%$). This along with dispersion of frequency for all methods at $-40dB$ noise is presented in figure 3.8.

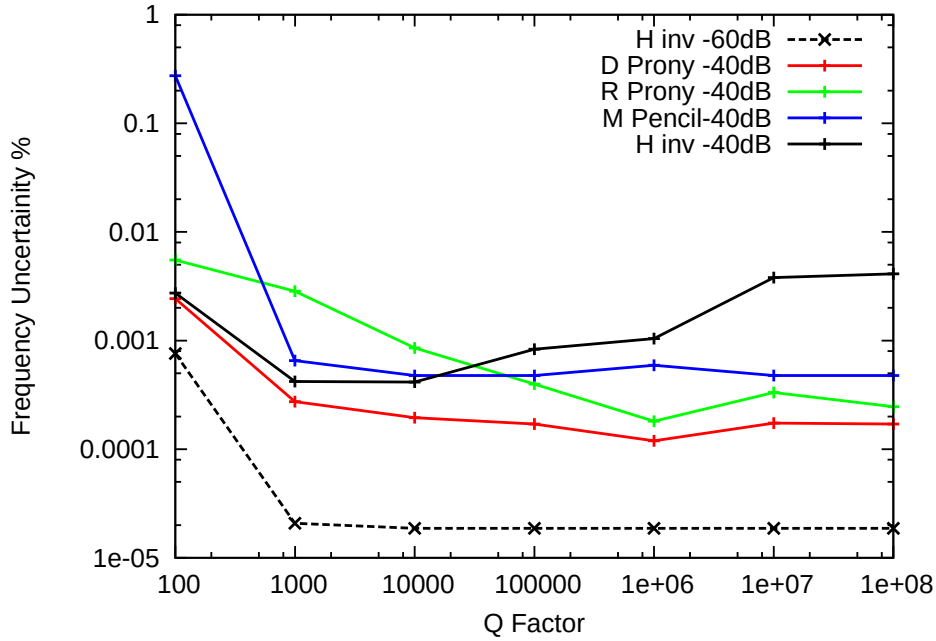

Figure 3.8: The numerical dispersion of frequency extracted by all methods at $-40dB$ and harmonic inversion at $-60dB$.

According to figure 3.8, in general, the statistical dispersion in estimated resonant frequency (i.e. error in resonant frequency for a given time signal)

is higher for low Q factors. This is due to the fast decay making most time samples (towards the end of the time signal) with lower signal to noise ratio than that indicated (Harmonic inversion has the largest statistical dispersion when the Q factors are high).

The median of the estimated Q factor is given in figure 3.9, whereas the dispersion of estimated Q factor as a percentage of the median Q is given in figure 3.10.

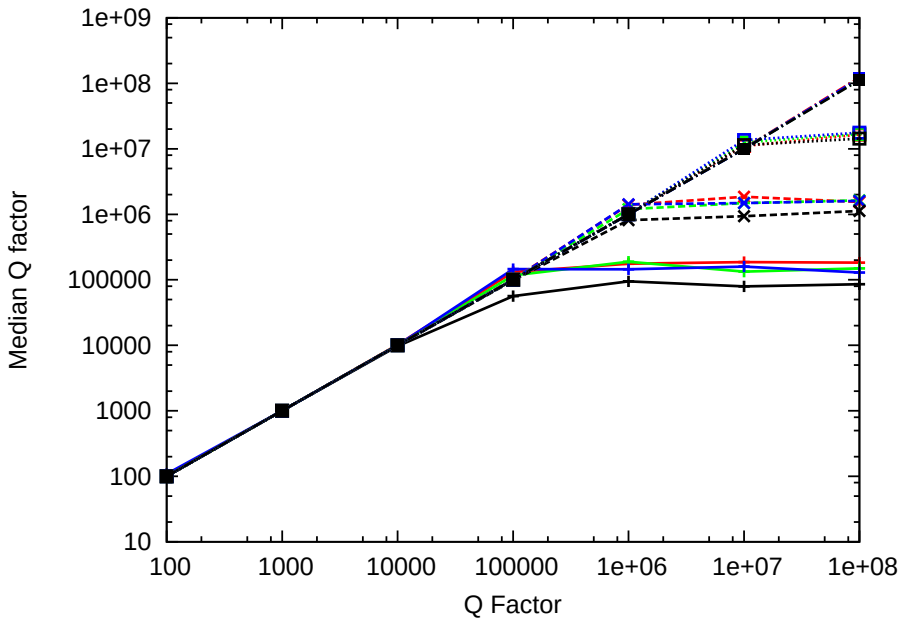

Figure 3.9: The median estimated Q factor from a time signal of $500fs$ at noise levels $-100dB$ (dot-dash), $-80dB$ (dotted), $-60dB$ (dashed), $-40dB$ (solid) extracted from difference Prony (red), recurrence Prony (green), matrix pencil (blue) and harmonic inversion (black) methods.

As can be seen from figure 3.9, at $-100dB$, the ratio of the estimated median to the actual Q factor is close to unity according to the gradient of the graph. At $-80dB$, the graph levels at about 10^7, at $-60dB$ levels at about 10^6 and at $-40dB$ levels at about 10^5 indicating that the median error in Q factor estimation is directly proportional to the noise level present in the signal.

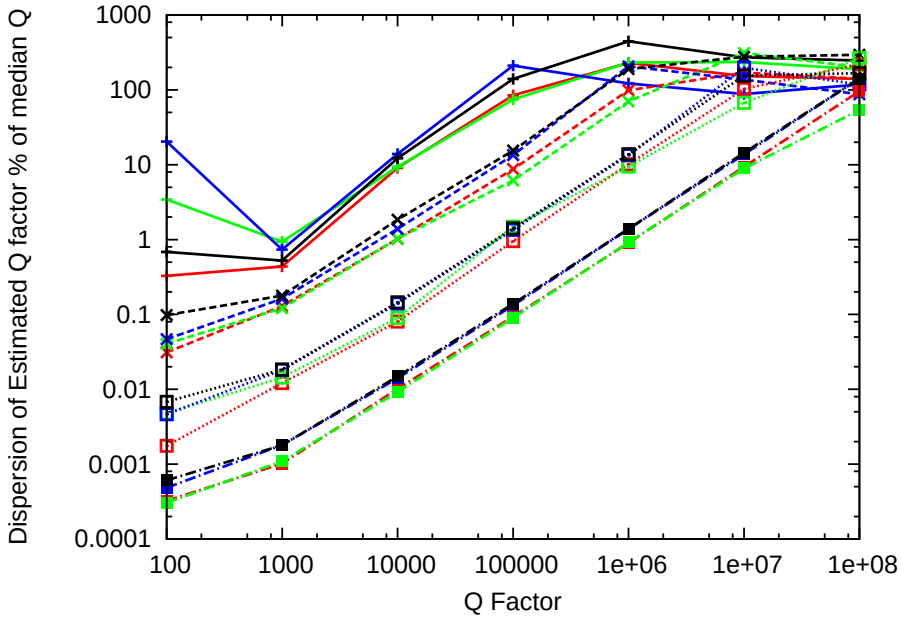

Figure 3.10: The interquartile range (measure of dispersion of Q) of estimated Q factor against the actual Q factor at noise levels at $-100dB$ (dot-dash), $-80dB$ (dotted), $-60dB$ (dashed), $-40dB$ (solid) extracted using difference Prony (red), recurrence Prony (green), matrix pencil (blue) and harmonic inversion (black) methods.

According to figure 3.10, the statistical dispersion of estimated Q increases by ten folds when the noise level is increased by ten folds in general. the percentage of statistical dispersion of Q reaches 100% when close to the levelling off point in figure 3.9. The two graphs indicate that the the maximum limit of the Q factor estimated from these methods is directly proportional to the noise level. Figure 3.10, shows no clear distinction as to which method is best/worst, according to the results seen so far, harmonic inversion is marginally worse than others.

The effect of increased time duration on Q factor estimation was observed by comparing a time signal of $1000fs$ duration with the same signal parameters and a noise level of $-60dB$. The median and inter-quartile range of these results are presented in figures 3.11 and 3.12 along with the results previously obtained for a time signal of duration $500fs$ with similar properties.

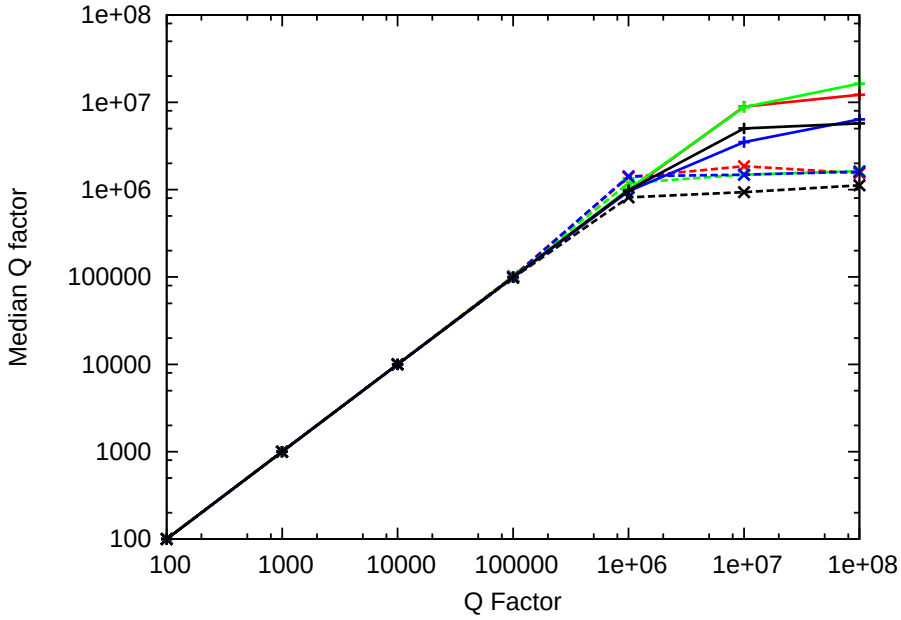

Figure 3.11: The median of estimated Q factor from a time signal of $500fs$ (dashed) and $1000fs$ (solid) at a noise level of $-60dB$ extracted from difference Prony (red), recurrence Prony (green), matrix pencil (blue) and harmonic inversion (black) methods.

According to figures 3.11 and 3.12, as a direct result of increasing the time duration by 2, both sets of curves have been shifted by a factor of 10. In other words, the maximum Q factor obtainable with a given accuracy is increased 10 times when the time duration is doubled.

Compared to FFT based extraction method presented, these methods have similar accuracy in estimating resonant frequency. But when estimating the Q factor (or imaginary part of frequency), complex frequency extraction methods, clearly outperform the FFT method. This is knowing that the complex extraction methods has 65 times less time duration and much lower SNR of 100dB-40dB (noiseless case in FFT includes quantisation noise of the IEEE double precision floating point value which calculates to $\approx 300dB$).

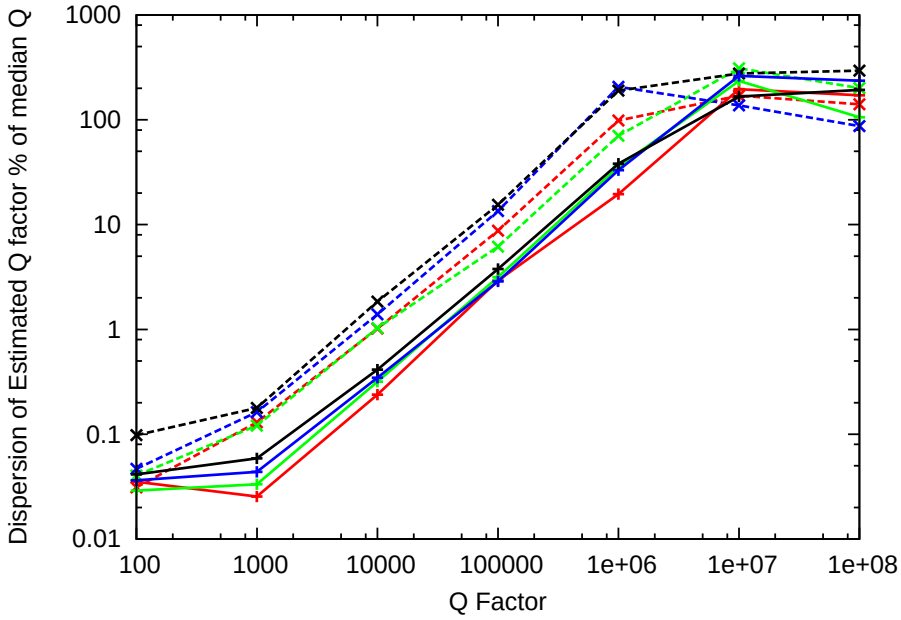

Figure 3.12: The inter-quartile range of estimated Q factor from a time signal of $500fs$ (dashed) and $1000fs$ (solid) at a noise level of $-60dB$ extracted from difference Prony (red), recurrence Prony (green), matrix pencil (blue) and harmonic inversion (black) methods.

3.4.2 Identifying Two Closely Spaced Resonances

In ultra high Q optical resonators, resonances of the same radial order occur at a separation given by the free spectral range(FSR), which depends on the dimensions of the resonator[24]. These need to be separated to obtain a correct estimation of Q factors. As shown previously with FFT, this can be obtained by high enough frequency resolution, requiring long simulation times. In addition to the heavy computations, errors due to the approximate nature of numerical wave simulation methods become higher when simulated for a longer time duration [25].

This section aims to obtain a limitation on the separability of two closely spaced resonances that can be obtained for a given length of time, by extracting a pair of resonances with varying separation at varying noise levels.

Signal Parameters

Time signals were formed by linearly combining two high Q resonances ($Q = 10^7$), where one resonance was placed at $193.548THz$ ($1.55\mu m$ free space wavelength), and the other placed with varying separation in frequency. Gaussian random noise was added to the signals at SNR levels of 100dB, 80dB.

Results

The resonant frequencies and Q factors were extracted using difference Prony, recurrence Prony, matrix pencil and harmonic inversion methods from the above mentioned time signals. For each signal parameter 100 distinct signals were generated with different noise values drawn from a Gaussian random number distribution.

In the simulations, the main concern was the separability of the resonance into two resonances by the extraction technique. If the method could identify the two resonances, the median error percentage and the interquartile range was insignificant and resembled the values obtained for isolated resonance case. The recurrance Prony method at $-80dB$ could not identify peaks closer than $0.5\Delta f$, where $\Delta f = 0.5THz$ is the frequency resolution determined by the total time ($2000fs$) in the time signal. All other methods could identify two seperate resonances upto $0.2\Delta f$, whereas the recurrence Prony method at $-100dB$ could identify even upto $0.1\Delta f$.

The median of the percentage errors in Q factor of such obtained resonances are shown in figure 3.13, whereas the interquartile range is shown in figure 3.14.

From figures 3.13 and 3.14, it is evident that the error in Q factor increases with decreasing separation in all methods except harmonic inversion. Below Δf harmonic inversion behave like other methods, but above Δf, its behaviour is unexplainable. This might be because of the filtering and decimation occurring in harmonic inversion method. However, this behaviour is not reported elsewhere and cannot be confirmed by this test alone. At $-100dB$ all methods (except harmonic inversion) can separate resonances upto $0.5\Delta f$

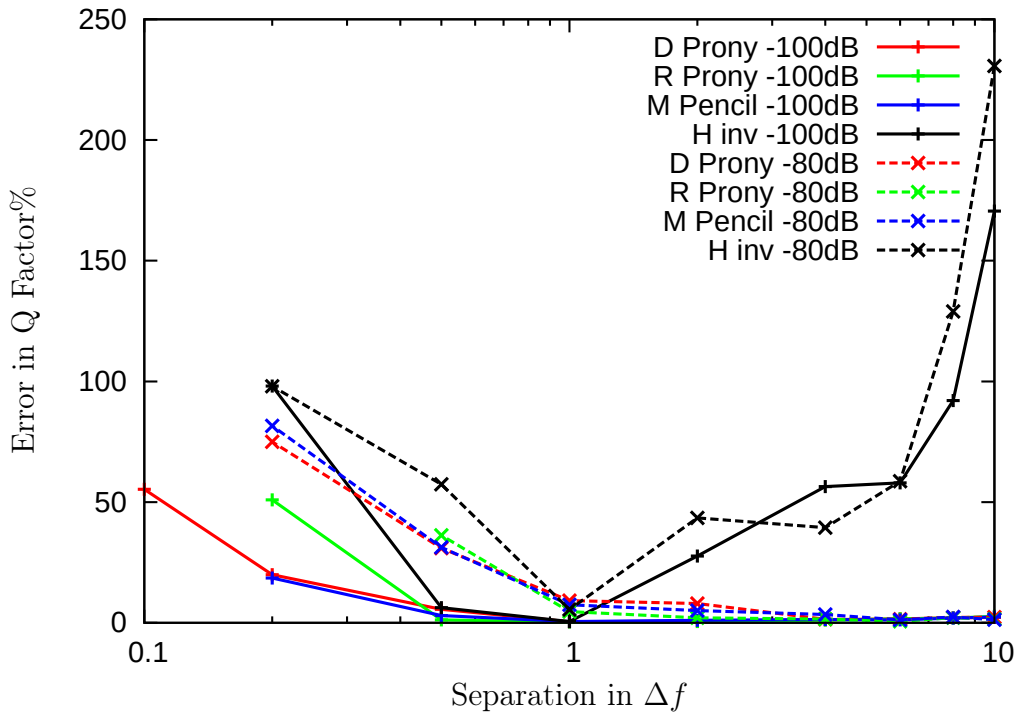

Figure 3.13: The median percentage error in extracting Q factors from time signals of two resonances of $Q = 10^7$ of length $2000fs$ with two noise levels -100dB (solid) and -80dB(dashed) obtained via difference Prony (red), recurrence Prony (green), matrix Pencil (black), and harmonic inversion (black).

with 10% accuracy in Q factor. At $-80dB$ all methods (except harmonic inversion) can separate resonances upto $2\Delta f$ with 10% accuracy in Q factor. This is the limitation of extracting two closely spaced high Q resonances from a limited time signal using complex frequency determination techniques.

According to the results obtained so far, the difference formulation of modified Prony method provides the best accuracy in the resonant frequency and the Q factor, while the recurrence formulation provides the least accurate results. The matrix pencil method provides results almost as good as the modified Prony method in most circumstances. The performance of the harmonic inversion method varies depending on the conditions of the signal such as noise, Q factor and separation in frequency in an unpredictable manner. In

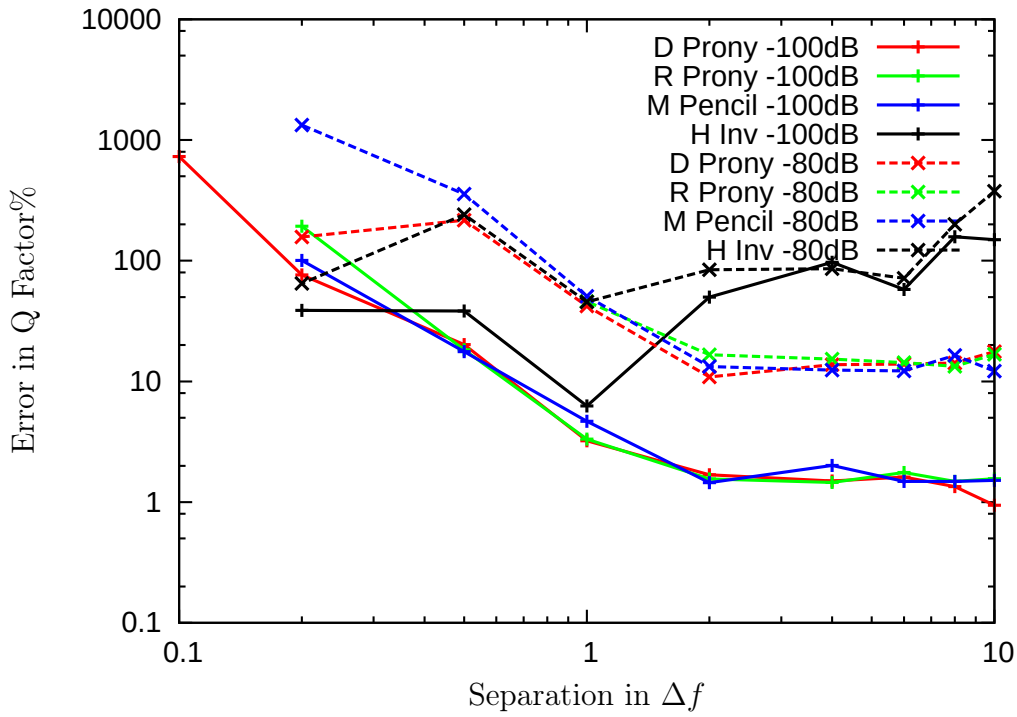

Figure 3.14: The interquartile range of percentage error in extracting Q factors from time signals of two resonances of $Q = 10^7$ of length $2000fs$ with two noise levels -100dB (solid) and -80dB(dashed) obtained via difference Prony (red), recurrence Prony (green), matrix Pencil (black), and harmonic inversion (black).

general, all methods could identify the resonant frequency and the Q factor with an accuracy better than the FFT based fitting method.

3.4.3 Extracting Resonances of a Dielectric Infinite Cylinder

Having studied the limitations of the frequency extraction techniques in extracting isolated and two closely spaced resonances, limitations occurring in applying these methods in extracting multiple resonances of a practical resonator, which contains a mix of low and high Q resonances with varying separations between them, are now studied.

Signal Parameters

An infinite cylindrical optical resonator is considered here as a typical example containing a mix of resonances. The complex resonant frequencies of an infinite cylinder placed in free-space can be obtained using an analytical solution as given in eqution 4.16 in the next chapter.

The time signal was formed from the resonances of an infinite cylinder of index $n = 2.82$ (As_2Se_3 at $1.55\mu m$ wavelength) and radius $a = 1.35\mu m$ within the frequency range of $150-250THz$, which includes resonances of azimuthual order m in the range of 1 to 16. Despite the sub wavelength dimensions, the resonances have high radiation Q factors, which in practical situations is much lower due to material loss [6]. All resonances of the form given in equation 3.6 with equal amplitudes A, were summed in time domain to form the time signal. Then, uniform random noise was added with an SNR of 80dB, and the resulting signal was sampled at $1fs$ intervals. Two such signals of length $2000fs$ and $4000fs$ were used to extract resonances. The Fourier transforms obtained for the signals with the two time lengths are shown in figure 3.15.

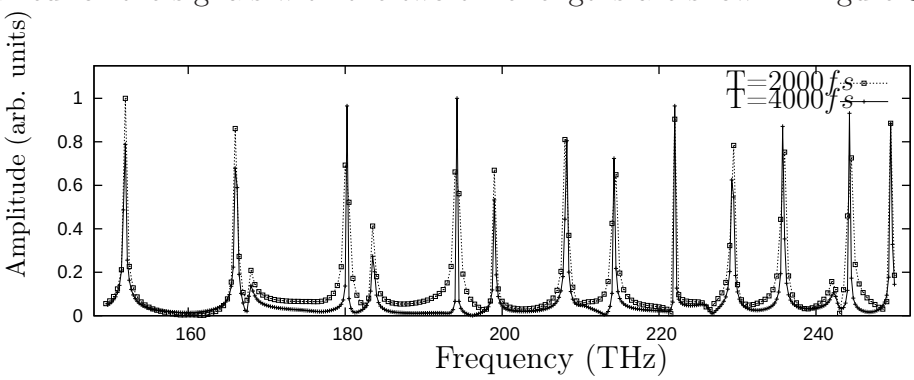

Figure 3.15: Magnitude of the discrete Fourier transform of the $2000fs$ and $4000fs$ long time signals of 2000 and 4000 samples respectively, containing the resonances of an infinite cylinder of refractive index $n = 2.82$ and radius $a = 1.35\mu m$, between 150-250THz with added noise of SNR=80dB.

Prony Method Modifications

In order to use the modified Prony methods, the number of components was first estimated from the Fourier transform shown in figure 3.15. Since each resonance appears as a complex conjugate pair forming a real signal, P should at least be twice the number of resonances present. According to figure 3.15, the number of frequency components P was initially set to 32.

The attempt to extract these resonances failed with the recurrence formulation with double precision calculations, as the limited precision of 53 bits (IEEE 754 floating point standard[26]) was not sufficient to perform the required Cholesky factorisation[18], when NP is large. Therefore, quadruple precision (113 bits according to IEEE 754[26]) was used in the modified Prony recurrence method.

In both formulations of modified Prony method, it was observed that the estimate of the Q factors improved when P was increased from its initial guess at $P = 32$. The estimated Q factors improved until P was equal to 60. In the solution, the additional resonances had small amplitude and/or did not fall within the frequency range of $150 - 250THz$ considered, indicating they were spurious resonances that helped the solution to converge while compensating for noise. This was confirmed from the solution of the matrix pencil method, which estimates the number of resonances from the most significant singular values, as mentioned in section 3.3.1. The matrix pencil solution also had 60 components and some of them were out of the frequency range of interest and had small amplitudes.

Results

The error in the resonant frequency and the Q factor are given in figures 3.16 and 3.17 respectively for the time signal of lengths $2000fs$ and $4000fs$.

According to figure 3.16(a), and figure 3.17(a), the difference Prony method was the most accurate, where as the matrix pencil method fared as the second best. According to figures 3.16 and 3.17, when extracting frequency, harmonic inversion was close in accuracy to the Fourier transform based method, while

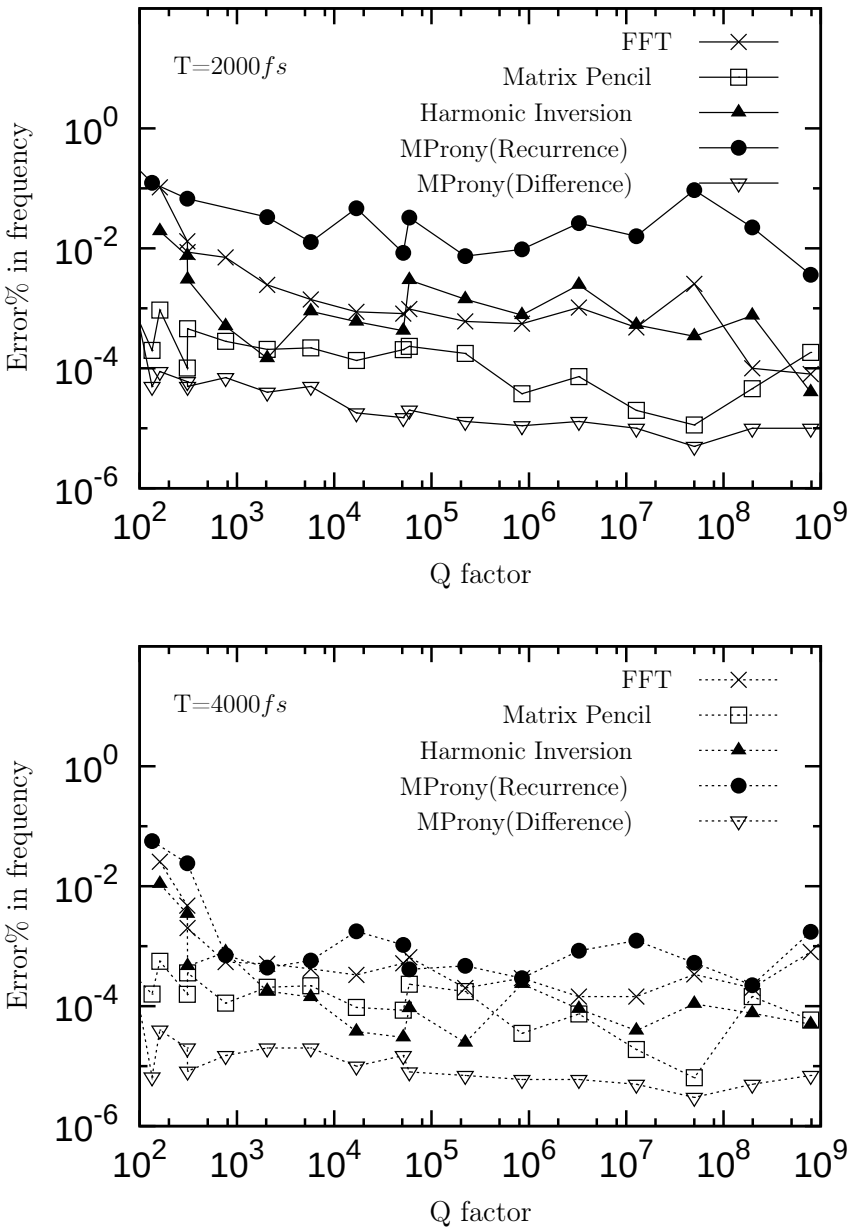

Figure 3.16: Error in resonant frequency estimation from a time signal (a) of length $T = 2000fs$ and (b) of length $T = 4000fs$, of a dielectric cylindrical cavity of radius $r = 1.35\mu m$ and refractive index $n = 2.82$ obtained using harmonic inversion, matrix pencil and modified Prony (recurrence and difference) methods. T is the length of the time signal.

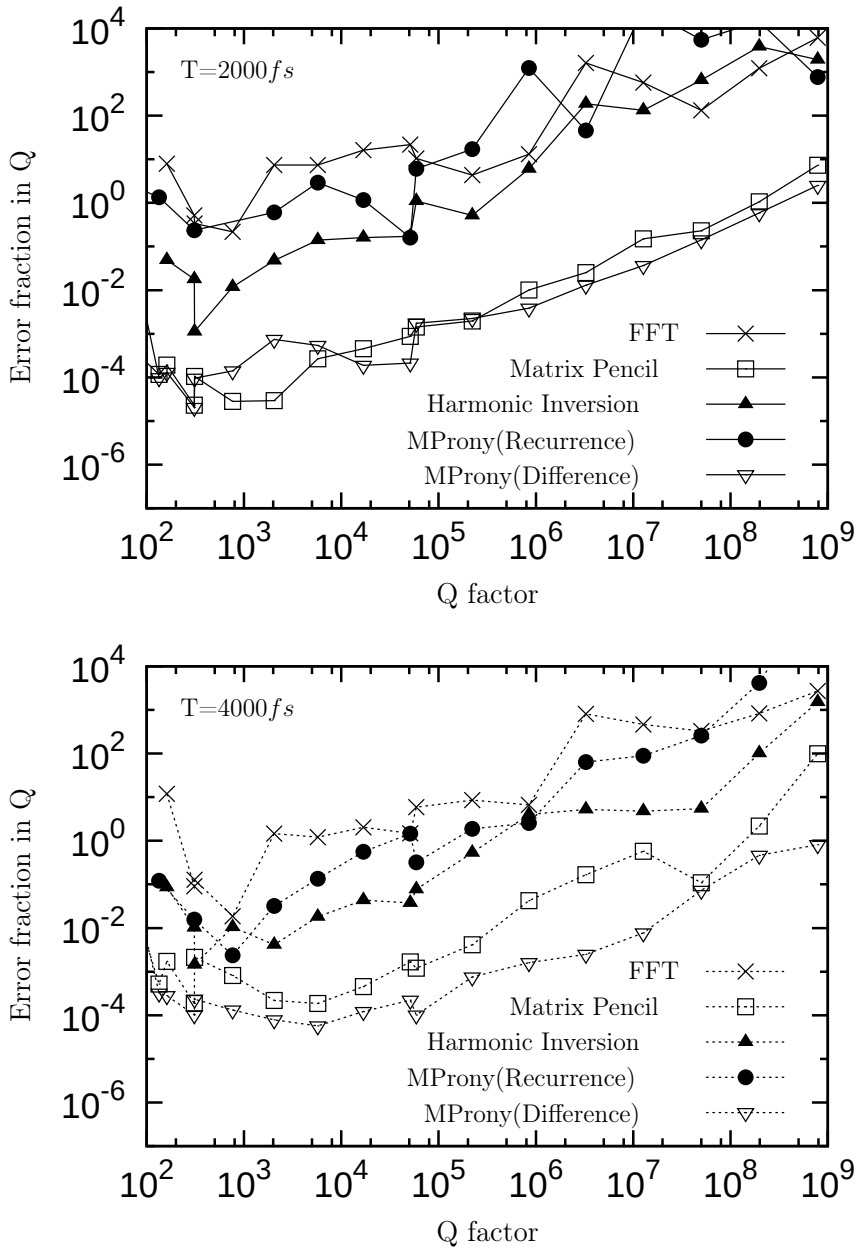

Figure 3.17: Error in Q factor estimation from a time signal (a) of length $T = 2000fs$ and (b) of length $T = 4000fs$, of a dielectric cylindrical cavity of radius $r = 1.35\mu m$ and refractive index $n = 2.82$ obtained using harmonic inversion, matrix pencil and modified Prony (recurrence and difference) methods. T is the length of the time signal.

the recurrence Prony method had the worst accuracy. However, harmonic inversion had better accuracy in estimating Q factors than the Fourier transform or recurrence Prony methods.

In general for all methods, the estimation of resonant frequency improved slightly with an increase in Q factor, while the estimation of Q factor degraded. An increase in the length of the time signal improved the accuracy in both resonant frequency and Q factor extraction of all methods.

Due to large P, and the high precision required to accommodate a large value of P, the difference Prony method was significantly more computationally heavy compared to other methods. The matrix pencil method on the other hand was quick to produce a solution when $N = 2000$, but took a significantly longer time, close to that of the difference Prony method, when $N = 4000$, due to the singular value decomposition of a matrix of rank 4000. Harmonic inversion was the quickest of all the methods and did not increase its complexity much when N was increased, due to the banded and decimated signal used to extract resonances.

It is important to note some limitations observed. In the matrix pencil and recurrence Prony methods, sampling of time signals beyond the Nyquist frequency limit ($f_{sampling} > 2f_{high}$), in order to decrease the matrix sizes, resulted in solutions mostly out of the frequency range of interest. This poses a challenge in transforming them into the frequency range of interest. Since the recurrence Prony method is unable to handle a large number of samples and resonances, this limitation in sampling interval renders the method marginally suitable for extracting the parameters of closely spaced high Q resonances.

Table 3.2 summarises the key ideas observed during the comparison of frequency extraction methods.

Therefore, for a given time signal, the modified difference Prony method is the best method in terms of accuracy to extract the resonant frequency and Q factor by tuning the number of components P and the calculation precision. The matrix pencil method can be a better alternative in terms of computational efficiency, when the number of time samples is sufficiently low. If the number of samples is very large, harmonic inversion provides a

Table 3.2: Frequency Extraction Method Summary

Method	Complexity	Accuracy	Remarks
FFT Fit	quick	low	Manual intervention for f_r
Harmonic Inversion	quick	medium	
MProny recurrence	medium	medium	Cannot be used when N is high Cannot be used for large Δt
MProny difference	slow	high	Multi-precision calculation required Memory limitations due to large matrices
Matrix Pencil	slow	high	Cannot be used for large Δt Memory limitations due to large matrices

reasonable alternative to both matrix pencil and modified difference Prony methods.

3.5 Conclusions

Resonant frequencies and Q factors are the fundamental spectral parameters of any resonator. Yet calculation of these properties from limited time signals obtained from time domain numerical simulations are not completely straight forward. Therefore, characterisation of resonance extraction techniques must be performed before applying them to extract resonances.

In this chapter, several resonant frequency estimation techniques useful for the extracting closely spaced high Q resonances of optical resonators from time domain data were discussed. As a very straight forward method, shape extraction from a Fourier transform of the time signal was presented. It was shown that a significant variation of Q factor changed the sample points in the Fourier transform only slightly when Q is high relative to the time signal length. Further, the method is poor in resolving two closely spaced resonances. These render the straight forward (Fourier transform based) method inappropriate to extract closely spaced high Q resonances. Therefore, several

complex exponential extraction techniques were then considered.

The recurrence formulation of the modified Prony method was capable of extracting isolated resonances with significant accuracy. However, its accuracy heavily reduces when two resonances are closely spaced, due to the closeness of the roots of the characteristic polynomial, to unity in the formulation, as mentioned in [18]. The difference formulation of the modified Prony method was then tested, but could not be used with standard 64-bit floating point precision as the repeated differencing and Cholesky factorisation in the method required higher precision. With the use of floating point numbers with adjustable precision, the method was successful in extracting multiple resonances with significant accuracy. However, the method was computationally intensive in practical situations, due to the multiple precision arithmetic involved and the large number of components required (P). The value for P should be much larger than the peaks visible in a Fourier transform of the time signal to accommodate resonances with small amplitudes and spurious resonances, which can be eliminated by selection. The matrix pencil method was found to be a good alternative with relatively high accuracy in evaluating both resonant frequency and Q factor. In addition, the harmonic inversion method, which is a relatively new means for extracting resonances, was tested. This method used low computational resources, while providing results with moderate accuracy.

Based on the information regarding the limitations of frequency extraction methods from limited time signals, the limitations of time domain numerical simulations can now be observed given that the accuracy of frequency extraction is made higher than that of the numerical method by simulating long enough to secure required accuracy. Therefore, the limitations of TLM in the context of optical resonators are studied in the next chapter.

References

[1] P. Debye, "Der lichtdruck auf kugeln von beliebigem material," *Annalen der Physik*, vol. 335, no. 11, pp. 57–136, 1909.

[2] A. N. Oraevsky, "Whispering-gallery waves," *Quantum Electronics*, vol. 32, no. 5, pp. 377–400, 2002.

[3] A. Ashkin and J. M. Dziedzic, "Observation of optical resonances of dielectric spheres by light scattering," *Appl. Opt.*, vol. 20, pp. 1803–1814, May 1981.

[4] J. Nilsson and S. Riedel, *Electric circuits*, vol. 8. Prentice Hall, 2009.

[5] W. Siebert, *Circuits, signals, and systems*, vol. 2. The MIT Press, 1986.

[6] M. L. Gorodetsky, A. A. Savchenkov, and V. S. Ilchenko, "Ultimate Q of optical microsphere resonators," *Optics Letters*, vol. 21, no. 7, pp. 453–455, 1996.

[7] E. J. Heller and M. J. Davis, "Molecular overtone bandwidths from classical trajectories," *The Journal of Physical Chemistry*, vol. 84, no. 16, pp. 1999–2001, 1980.

[8] E. J. Heller, E. B. Stechel, and M. J. Davis, "Molecular spectra, fermi resonances, and classical motion," *The Journal of Chemical Physics*, vol. 73, no. 10, pp. 4720–4735, 1980.

[9] M. D. Feit, J. A. Fleck Jr., and A. Steiger, "Solution of the schrödinger equation by a spectral method," *Journal of Computational Physics*, vol. 47, no. 3, pp. 412–433, 1982.

[10] M. R. Wall and D. Neuhauser, "Extraction, through filter-diagonalization, of general quantum eigenvalues or classical normal mode frequencies from a small number of residues or a short-time segment of a

signal. i. Theory and application to a quantum-dynamics model," *Journal of Chemical Physics*, vol. 102, no. 20, pp. 8011–8022, 1995.

[11] D. Marquardt, "An algorithm for least-squares estimation of nonlinear parameters," *Journal of the Society for Industrial and Applied Mathematics*, vol. 11, no. 2, pp. 431–441, 1963.

[12] W. Press, B. Flannery, S. Teukolsky, W. Vetterling, *et al.*, *Numerical recipes*, vol. 547. Cambridge Univ Press, 1986.

[13] T. K. Sarkar and O. Pereira, "Using the matrix pencil method to estimate the parameters of a sum of complex exponentials," *Antennas and Propagation Magazine, IEEE*, vol. 37, no. 1, pp. 48–55, 1995.

[14] Y. Hua and T. K. Sarkar, "On SVD for estimating generalized eigenvalues of singular matrix pencil in noise," *Signal Processing, IEEE Transactions on*, vol. 39, no. 4, pp. 892–900, 1991.

[15] M. H. Kahn, M. S. Mackisack, M. R. Osborne, and G. K. Smyth, "On the consistency of Prony's method and related algorithms," *Journal of Computational and Graphical Statistics*, pp. 329–349, 1992.

[16] M. R. Osborne and G. K. Smyth, "A modified Prony algorithm for fitting functions defined by difference equations," *SIAM journal on scientific and statistical computing*, vol. 12, pp. 362–382, 1991.

[17] M. R. Osborne, "Some special nonlinear least squares problems," *SIAM Journal on Numerical Analysis*, pp. 571–592, 1975.

[18] M. R. Osborne and G. K. Smyth, "A modified Prony algorithm for exponential function fitting," *SIAM Journal on Scientific Computing*, vol. 16, no. 1, pp. 119–138, 1995.

[19] V. A. Mandelshtam and H. S. Taylor, "Harmonic inversion of time signals and its applications," *The Journal of Chemical Physics*, vol. 107, no. 17, pp. 6756–6769, 1997.

[20] A. Taflove and S. C. Hagness, *Computational electrodynamics.* Artech House Boston, 1995.

[21] C. Christopoulos, *The transmission-line modeling method: TLM.* Institute of Electrical and Electronics Engineers, 1995.

[22] S. Le Maguer and M. M. Ney, "Extended PML-TLM node: an efficient approach for full-wave analysis of open structures," *International Journal of Numerical Modelling: Electronic Networks, Devices and Fields*, vol. 14, no. 2, pp. 129–144, 2001.

[23] M. Matsumoto and T. Nishimura, "Mersenne twister: a 623-dimensionally equidistributed uniform pseudo-random number generator," *ACM Transactions on Modeling and Computer Simulation (TOMACS)*, vol. 8, no. 1, pp. 3–30, 1998.

[24] V. S. Ilchenko and A. B. Matsko, "Optical resonators with whispering-gallery modes-Part ii: Applications," *Selected Topics in Quantum Electronics, IEEE Journal of*, vol. 12, no. 1, pp. 15–32, 2006.

[25] P. Sewell, T. M. Benson, A. Vukovic, and A. A. Jarro, "The challenges for numerical time domain simulations of optical resonators," in *Transparent Optical Networks (ICTON), 2010 12th International Conference on*, pp. 1–4, 2010.

[26] M. L. Overton, *Numerical computing with IEEE floating point arithmetic.* SIAM, 2001.

4

Limitations of Time Domain Numerical Methods

In almost all numerical method solutions there exists an error which can for example be quantified by comparing with results for a problem for which an analytical solution exists. The success of the numerical method lies in its ability to converge quickly to the required solution with refinement of the numerical method. Finite Difference Time Domain (FDTD) method and the transmission line modelling (TLM) method fall into the category of time domain numerical methods based on the differential form of Maxwell's equations. They are considered as rigorous methods, which converges with mesh refinement. However, this assumption is sometimes questionable; as pointed out by Boriskin *et. al* in [1], for example, FDTD does not converge to the known scattered spectra of an infinite cylinder excited externally by a line source with mesh refinement. This section therefore is dedicated to identifying the roots of such a deviation from the analytical solution, in the context of modelling optical resonators.

4.1 Problem Description

From the paper by Boriskin *et. al* , it is deducible that the solution of electromagnetic problems containing circular boundaries using a time domain code that is run for a long time is prone to errors. Further, the size of the geometries used in [1] is comparable in size to the interested wavelength. In a bid to isolate the causes of the errors, an isolated infinite cylinder of radius a and refractive index n_c was studied analytically and using TLM. But instead of exciting from outside the geometry as in [1], an off-centre line source inside the geometry was used. By using a source inside the resonator, the influence of coupling was eliminated. Free-space coupling tends to be poor for resonators especially when the Q factors are high [2]. This also minimises the effect of back scattering from the end of the simulation domain. Hence, in this chapter, the intrinsic problem of modelling of circular optical resonators is considered.

4.2 An Analytical Approach

Consider an infinite cylinder of homogeneous nonmagnetic dielectric material of refractive index n_c of radius a placed in freespace $n_0 = 1$.

The time harmonic field form of the Maxwell curl equations[3] in equations 4.1 and 4.2 for a time variation of $e^{j\omega t}$, in an isotropic medium can be expanded in a cylindrical coordinate system (ρ, φ, z) to the form given in equations 4.3a to 4.3f for a source free domain.

$$\nabla \times \mathbf{E} = -j\omega\mu\mathbf{H} \tag{4.1}$$

$$\nabla \times \mathbf{H} = j\omega\varepsilon\mathbf{E} + \mathbf{J} \tag{4.2}$$

$$\left(\frac{1}{\rho}\frac{\partial E_z}{\partial \varphi} - \frac{\partial E_\varphi}{\partial z}\right) = -j\omega\mu H_\rho \tag{4.3a}$$

$$\frac{\partial E_\rho}{\partial z} - \frac{\partial E_z}{\partial \rho} = -j\omega\mu H_\varphi \tag{4.3b}$$

$$\frac{1}{\rho}\left(\frac{\partial(\rho E_\varphi)}{\partial \rho} - \frac{\partial E_\rho}{\partial \varphi}\right) = -j\omega\mu H_z \tag{4.3c}$$

$$\left(\frac{1}{\rho}\frac{\partial H_z}{\partial \varphi} - \frac{\partial H_\varphi}{\partial z}\right) = j\omega\varepsilon E_\rho \tag{4.3d}$$

$$\frac{\partial H_\rho}{\partial z} - \frac{\partial H_z}{\partial \rho} = j\omega\varepsilon E_\varphi \tag{4.3e}$$

$$\frac{1}{\rho}\left(\frac{\partial(\rho H_\varphi)}{\partial \rho} - \frac{\partial H_\rho}{\partial \varphi}\right) = j\omega\varepsilon E_z \tag{4.3f}$$

The whispering gallery modes can be categorised into two types in order to obtain the reduced scalar wave equation of Debye Potential [4]. In electric type waves one magnetic field component is zero, whereas in magnetic type waves one electric field component is zero [2]. In the case of a cylinder infinite in z-dimension, H_z and E_z are zero in E type and H type waves respectively.

4.2.1 Electric Type Waves

Given $H_z = 0$, from equation 4.3c,

$$\frac{\partial(\rho E_\varphi)}{\partial \rho} = \frac{\partial E_\rho}{\partial \varphi} \tag{4.4}$$

By defining W so that $\rho E_\varphi = \frac{\partial W}{\partial \varphi}$, $E_\rho = \frac{\partial W}{\partial \rho}$, and $W = \frac{\partial U}{\partial z}$, from equations 4.3d and 4.3e, one can obtain,

$$H_\varphi = -j\omega\varepsilon\frac{\partial U}{\partial \rho} \tag{4.5}$$

$$H_\rho = j\omega\varepsilon\frac{1}{\rho}\frac{\partial U}{\partial \varphi} \tag{4.6}$$

By substituting 4.5 in 4.3f, one can obtain an expression for E_z in terms of U. In order to satisfy 4.3b and 4.3c with expressions for H_φ, H_ρ, and E_z in terms of U, the reduced wave equation can be obtained for cylindrical coordinates as given in equation 4.7 [2].

$$\frac{\partial^2 U}{\partial z^2} + \frac{1}{\rho}\frac{\partial}{\partial \rho}\left(\rho\frac{\partial U}{\partial \rho}\right) + \frac{1}{\rho^2}\left(\frac{\partial^2 U}{\partial \varphi^2}\right) + k^2 U = 0 \tag{4.7}$$

The electric field components are given by[2],

$$E_\rho = \frac{\partial^2 U}{\partial \rho \partial z} \tag{4.8}$$

$$E_\varphi = \frac{1}{\rho}\frac{\partial^2 U}{\partial \varphi \partial z} \tag{4.9}$$

$$E_z = \frac{\partial^2 U}{\partial z^2} + k^2 U \tag{4.10}$$

Since there is no variation of potential along the z-axis(infinite), the RHS of equations 4.8, 4.9, and the first term of equation 4.10 vanish.

By variable separation of $U(\rho, \varphi) = R(\rho)\Phi(\varphi)$, one can obtain from equation 4.7,

$$\rho^2\frac{d^2 R}{d\rho^2} + \rho\frac{dR}{d\rho} + (k^2\rho^2 - c)R = 0 \tag{4.11}$$

$$\frac{d^2\Phi}{d\varphi} + c\Phi = 0 \tag{4.12}$$

where $\frac{c}{\rho^2}$ is the separation constant.

Since the azimuthal variation $\Phi(\varphi)$ is continuous from $\varphi = 0$ to $\varphi = 2\pi$, $0 < c = m^2$, where $m \in \mathbb{Z}_0^+$. Hence, the solution of $\Phi(\varphi)$ consists of sinusoidals. Equation 4.11, is the Bessel differential equation where the argument is $k\rho$ and the order of the Bessel function is m. Since the field inside the cylinder is finite, the solution inside will consist of Bessel functions of the first kind $J_m(k\rho)$. In order to satisfy the radiation condition, the solution outside the cylinder will consist of outgoing Hankel functions (second kind) $H_m^{(2)}(k_0\rho)$.

Therefore, the general solution for a cylindrical resonator can be expressed as

$$U_m(\rho,\varphi) = \begin{cases} C_m^i J_m(k\rho)e^{\pm jm\varphi} & \rho \leq a \\ C_m^e H_m^{(2)}(k_0\rho)e^{\pm jm\varphi} & \rho > a \end{cases} \tag{4.13}$$

From the continuity of tangential field components E_z and H_φ at the cylinder boundary($\rho = a$) one can obtain two relationships between C_m^i, C_m^e for nonmagnetic materials, as given in equations 4.14 and 4.15 respectively.

$$\frac{C_m^e}{C_m^i} = \varepsilon \frac{J_m(k_0\sqrt{\varepsilon}a)}{H_m^{(2)}(k_0 a)} \tag{4.14}$$

$$\frac{C_m^e}{C_m^i} = \varepsilon^{\frac{3}{2}} \frac{J_m'(k_0\sqrt{\varepsilon}a)}{H_m^{(2)\prime}(k_0 a)} \tag{4.15}$$

By combining equations 4.14 and 4.15 one can obtain the characteristic equation of k_0 as in equation 4.16, the roots of which are the resonances of the dielectric nonmagnetic infinite cylinder.

$$J_m(k_0\sqrt{\varepsilon}a)H_m^{(2)\prime}(k_0 a) - \sqrt{\varepsilon}J_m'(k_0\sqrt{\varepsilon}a)H_m^{(2)}(k_0 a) = 0 \tag{4.16}$$

Due to the oscillatory nature of the cylindrical waves, there exists an infinite number of roots to the characteristic equation. Hence, resonances are denoted by two mode numbers m and q, where q denotes the qth root of the characteristic equation of order m. From the discussion provided in [2] for spherical resonators, one can come up with some observations about resonances in an infinite cylinder. As in spherical resonators, q also denotes the number of nodes of the field within the cylinder in the radial direction [2]. Hence, q is noted as the radial order. Similarly, m denotes the number of nodes in the azimuthal direction; hence named azimuthal order. Hence, m and q together completely describe the modes within an infinite cylinder be they high Q whispering gallery or low Q bulk modes. From the properties of Bessel functions, the Q factors of a particular azimuthal order m decreases with increasing radial order q [2]. This is also related to the fact the higher q

(more nodes within cylinder) the larger the modal volume.

4.2.2 Magnetic Type Waves

Given $E_z = 0$, from equation 4.3f,

$$\frac{\partial(\rho H_\varphi)}{\partial \rho} = \frac{\partial H_\rho}{\partial \varphi} \tag{4.17}$$

By defining W so that $\rho H_\varphi = \frac{\partial W}{\partial \varphi}$, $H_\rho = \frac{\partial W}{\partial \rho}$, and $W = \frac{\partial V}{\partial z}$, from equations 4.3a and 4.3b, one can obtain,

$$E_\varphi = j\omega\mu \frac{\partial V}{\partial \rho} \tag{4.18}$$

$$E_\rho = -j\omega\mu \frac{1}{\rho}\frac{\partial V}{\partial \varphi} \tag{4.19}$$

By combining equations 4.18,4.19 and 4.3c, 4.3d,4.3e, one could obtain the reduced wave equation for the H type waves as given in equation 4.20, which is of the same form as equation 4.7.

$$\frac{\partial^2 V}{\partial z^2} + \frac{1}{\rho}\frac{\partial}{\partial \rho}\left(\rho \frac{\partial V}{\partial \rho}\right) + \frac{1}{\rho^2}\left(\frac{\partial^2 V}{\partial \varphi^2}\right) + k^2 V = 0 \tag{4.20}$$

Similar to E-type waves, H_ρ and H_φ components vanish due to z-invariant V. The only magnetic component is given by,

$$H_z = k^2 V \tag{4.21}$$

Since the reduced wave equations for both E and H types are similar, the general solution of H-type waves will be

$$V_m(\rho, \varphi) = \begin{cases} C_m^i J_m(k\rho) e^{\pm jm\varphi} & \rho \leq a \\ C_m^e H_m^{(2)}(k_0\rho) e^{\pm jm\varphi} & \rho > a \end{cases} \tag{4.22}$$

From the continuity of tangential components E_φ and H_z at the cylinder

boundary, one can obtain two relations between C_m^i and C_m^e for nonmagnetic materials as given in equations 4.23 and 4.24 respectively.

$$\frac{C_m^e}{C_m^i} = \varepsilon \frac{J_m(k_0\sqrt{\varepsilon}a)}{H_m^{(2)}(k_0 a)} \tag{4.23}$$

$$\frac{C_m^e}{C_m^i} = \sqrt{\varepsilon} \frac{J_m'(k_0\sqrt{\varepsilon}a)}{H_m^{(2)\prime}(k_0 a)} \tag{4.24}$$

By combining equations, 4.23 and 4.24, on can obtain the characteristic equation of k_0 for H type waves as given in equation 4.25, the roots of which are the H type resonances of the nonmagnetic infinite cylinder.

$$\sqrt{\varepsilon} J_m(k_0\sqrt{\varepsilon}a) H_m^{(2)\prime}(k_0 a) - J_m'(k_0\sqrt{\varepsilon}a) H_m^{(2)}(k_0 a) = 0 \tag{4.25}$$

4.2.3 Resonant Frequencies and Q factors

The resonant frequencies and the Q factor of the structure considered in this chapter for E and H type waves can be extracted by solving equations 4.16 and 4.25 for complex k_0 respectively. The resonant frequency f_r and the Q factor can be obtained from the following relations[2].

$$f_r = \frac{c}{2\pi} \Re(k_0) \tag{4.26}$$

$$Q = \frac{\Re(k_0)}{2\Im(k_0)}$$

The equations 4.16 and 4.25 were solved by Newton Rhapson method for resonant frequencies between $150THz$ and $250THz$ ($1.55\mu m$ centre wavelength), for a cylinder of $r = 1.35\mu m$ and $n = \sqrt{\varepsilon} = 2.82$. Table 4.1 shows the resonant frequencies and Q factors for E waves, while table 4.2 shows the resonant frequencies of Q factors of H waves within the frequency range of interest.

The resonant frequency and Q factor results shown in tables 4.1 and 4.2 indicates that the Q factor increases as the number of nodes in the azimuthal

Table 4.1: The E type analytical resonances of a dielectric cylinder of $r = 1.35\mu m$ and $n = 2.82$ in the frequenbcy range of 150 - $250THz$

Azimuthal Order	Radial Order	Res. Freq. (THz)	Q
9	1	151.90	5.89×10^4
6	2	151.91	134
10	1	166.12	2.22×10^5
7	2	167.88	308
11	1	180.22	8.47×10^5
8	2	183.59	766
12	1	194.23	3.27×10^6
9	2	199.05	2042
13	1	208.16	1.27×10^7
7	3	209.91	92
10	2	214.30	5744
14	1	222.02	5.00×10^7
8	3	226.20	161
11	2	229.37	16868
15	1	235.82	1.98×10^8
9	3	242.34	310
12	2	244.28	51263
16	1	249.56	7.87×10^8

direction increases. When the radial order increased, the Q factor is decreased significantly. These results will be later used to compare the resonant frequencies and Q factors estimated from TLM numerical simulations for E and H waves.

4.3 Limitations in Representing Domains in a Cartesian mesh

Two dimensional numerical methods based on Cartesian (structured) meshes represent each geometry by a set of cuboids (in special cases cubes). There-

Table 4.2: The H type analytical resonances of a dielectric cylinder of $r = 1.35\mu m$ and $n = 2.82$ in the frequenbcy range of 150 - $250THz$

Azimuthal Order	Radial Order	Res. Freq. (THz)	Q
8	1	150.42	1.61×10^4
9	1	164.71	6.14×10^4
10	1	178.88	2.37×10^5
7	2	180.46	165
11	1	192.93	9.22×10^5
8	2	196.38	468
12	1	206.90	3.61×10^6
9	2	211.96	1382
13	1	220.79	1.42×10^7
10	2	227.25	4206
14	1	234.62	5.66×10^7
11	2	242.34	1.31×10^4
15	1	248.38	2.26×10^8

fore, the representation of the non-recti-linear edges of a geometry is non-exact. Furthermore, if the mesh is uniform in each direction, even recti-linear edges not confirming to the grid cannot be expressed exactly. Figures 4.1a and 4.1b illustrate these situations.

The stair-step approximation to curved or non-mesh-conforming boundaries poses several problems. Misrepresentation of the area and/or the perimeter of the geometry is one such problem. Another problem concerning resonators would be spurious resonances, and resonance frequency shifts due to the irregular boundary [5, 6]. In the next section, generally used methods of discretisation are tested for the circular dielectric resonator geometry discussed in section 4.2 to observe the influence of these on the accuracy of results produced using a 2D TLM method.

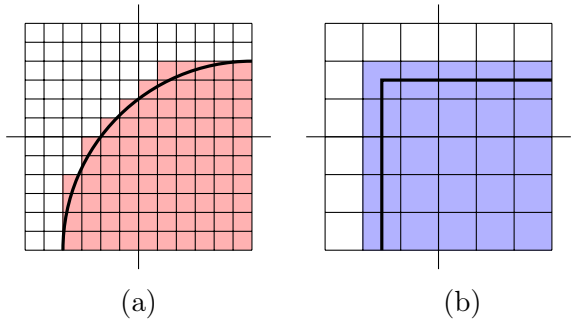

Figure 4.1: Limitations of representing (a) non-recti-linear edges and (b) non-mesh-conforming recti-linear edges in a uniform Cartesian mesh

4.4 Standard Methods of Discretisations

Since there is an ambiguity in selecting border-cells (cells partially covered by the geometry) attached to the circular geometry, one can often find several methods to approximate the curved boundary. If all border-cells are considered as inner part of the discretised geometry the total area and the perimeter will be overestimated; this will be referred to as "outside" stair-step approximation. If all border-cells are not included in the description of the inner part of the geometry, it will be referred to as "inside" stair-step approximations. This underestimates area and perimeter. These two cases are illustrated in figures 4.2a and 4.2b and may be regarded as the two extremes of the discretisation of a geometry. The difference between the two becomes smaller as the cell size decreases.

In order to test the applicability and limitations of these two standard methods of discretisation in the context of a circular resonator, the frequency response of energy within the resonator after a line source excitation inside the resonator will be compared against the analytical results obtained previously.

The domain of the simulation was discretised so that the usual rule of thumb, where $\Delta l < \lambda_{min}/10$ holds true. The complete set of simulation parameters is given in table 4.3 and the simulation structure is illustrated in figure 4.3.

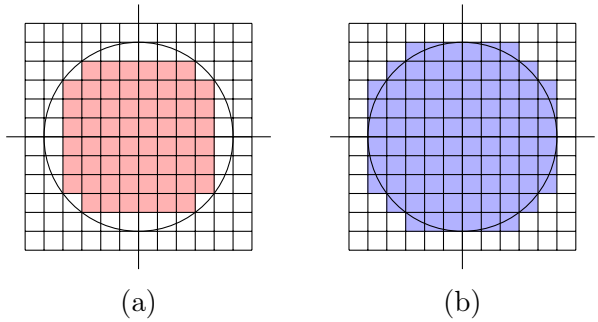

Figure 4.2: (a) Inside and (b) outside discretisations of a circle in a Cartesian mesh

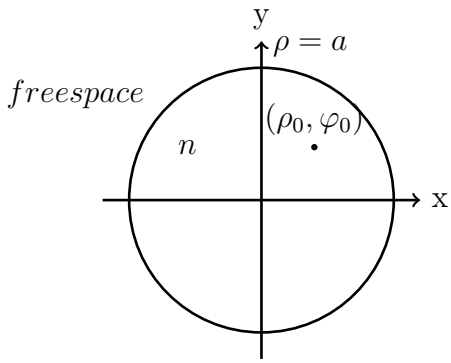

Figure 4.3: Infinite cylinder ($\rho = a$) when exited with an infinite line source placed at $\mathbf{r_0} = (\rho_0, \varphi_0)$.

The spectrum of the total energy is defined in terms of the Fourier transform $\mathcal{F}$ as,

$$E_{res}(f) = \int_{\Omega} \mathcal{F}\{E_z(\mathbf{r}, t)\}\mathcal{F}\{E_z(\mathbf{r}, t)\}^* d\mathbf{r} \tag{4.27}$$

where Ω is the domain of the resonator (i.e cylinder). The spectrum of energy for inside and outside discretisations are plotted alongside the analytical result for resonant frequency for E waves in figure 4.5. It is not immediately obvious from this plot which peak in the spectrum corresponds to which analytic resonant frequency. This information can be deduced from the corresponding modal fields pattern by Fourier transforming the time signal at every point

Table 4.3: Simulation parameters of the infinite cylinder in air excited by a pulsed line source

Refractive Index (As_2Se_3)	n	2.82
Radius	r	$1.35\mu m$
Domain step size	Δl	$0.05\mu m$
Time step	Δt	$\sqrt{2}\Delta l/c$
Domain Size		$10\mu m \times 10\mu m$
Domain Truncation		TLM Matched Boundary
Source position	ρ_0	$1.13\mu m$
relative to center	φ_0	$\pi/4$
Width of Gaussian Pulse	w	$5fs$
Centre frequency of excitation	f_0	$200THz$
Centre wavelength in medium	λ_m	$0.5319\mu m$

and observing the field pattern in space at a frequency close to the centre of the peak. Some of the field patterns for inside and outside discretisations are shown in figure 4.4.

For these standard methods of discretisations, the frequency shifts reported by Boriskin *et. al* [1] can be confirmed from figure 4.5. But the two extreme discretisations shift the curve in opposite directions. This indicates that minute variations at the boundary can change/shift the response of the resonators significantly.

The variation of these shifts are then observed for finer meshes with space steps of $0.025\mu m$ and $0.0125\mu m$. Figures 4.6 and 4.7 show the energy spectrum of E waves for step sizes of $0.025\mu m$ and $0.0125\mu m$ respectively.

From figures 4.6 and 4.7, it should be noted that the difference between the resonances predicted using the inside and the outside discretisations is not only limited to a frequency shift. The relative amplitudes of resonances are different, indicating that discretisation plays an important role in modelling resonators.

There is a significant error in resonant frequency predicted in $\lambda/10$ ($0.05\mu m$) step size towards the higher frequencies. This effect can be related to mesh

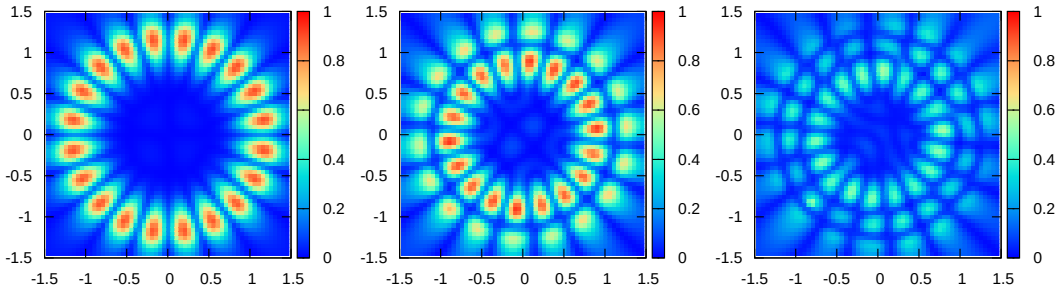

(a) WGM(10,1) inside (b) WGM(9,2) inside (c) WGM(9,3) outside

Figure 4.4: The Resonant Magnitude Mode Shapes of (a)WGM(10,1) in inside (b)WGM(9,2) in inside (c)WGM(9,3) in outside discretisations.

dispersion which is the intrinsic error of the TLM mehod [7]. The mesh dispersion occurs in TLM due to the small amount of magnetic susceptibility coupled when representing electric susceptibilities [7]. The amount of magnetic susceptibility decreases with decreasing step size; hence the error should diminish rapidly when the step size is decreased. However, in this case it does not and there exists a significant frequency shift even at $\lambda_{min}/40$ step size in figure 4.7. The shifts in resonant frequency observed in these graphs from the analytical result confirms the non converging frequency shift reported by Boriskin *et. al* [1].

However, this is not necessarily due to the boundary as the authors of [1] suspected. As can be seen from figures, 4.5, 4.6 and 4.7, the shift is nearly symmetric about the analytical resonant frequencies and the direction of the shift depends upon the discretisation method. If the shift was solely due to the boundary, the shift should be assymetric about the analytical resonant frequencies affecting both geometries alike. Therefore, the results indicate that the discretised area should be chosen carefully in order to obtain accurate results for the resonant frequency (i.e. spectrum) when simulating non-Cartesian geometries using a Cartesian mesh.

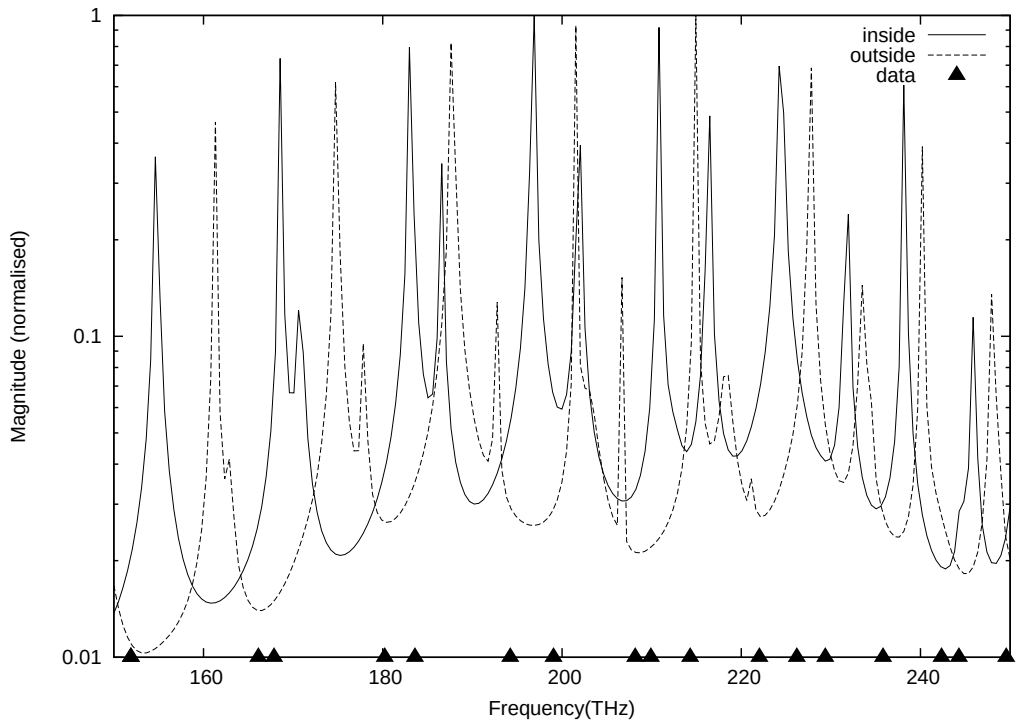

Figure 4.5: The energy spectrum of E type waves supported by an infinite cylinder excited by a line source inside the resonator for inside and outside discretisation with a space step of $0.05\mu m$ along with the analytical resonant frequencies.

4.5 Alternative methods of Discretisation

The above discussion leads towards an intermediate discretisation method in order to accurately model non-Cartesian geometries using structured TLM meshes. The most obvious solutions that spring to mind would be graded meshing [8] and multi meshing [9] in order to use finer meshes to describe boundary regions without compromising on computational demand.

The graded meshing technique enables higher resolution and rectangular cell sizes to represent finer details of the geometry as illustrated in figure 4.8a. The graded meshing maintains one-to-one links to neighbouring cells, by applying the grading along vertical and/or horizontal lines. In order to match

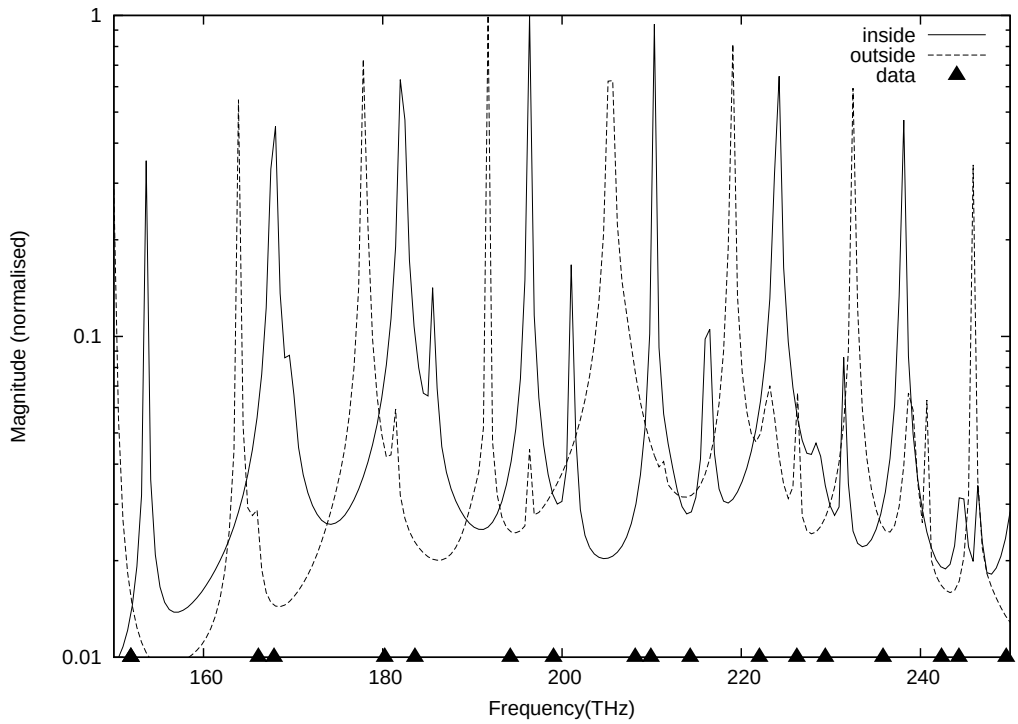

Figure 4.6: The energy spectrum of an infinite cylinder excited by a line source inside the resonator of E type waves for inside and outside discretisation along with the analytical resonant frequencies for step size of $0.025\mu m$.

the Courant criteria, the time step is reduced to match the smallest space step in the mesh, demanding more computational effort. Hence, for a given total simulation time the number of time steps will be doubled when the smallest step size is halved, but this approach does not result in a significant increase in the total number of cells. Therefore, the grading operation results in a linear increase in computational complexity, whereas a usual mesh refinement on the entire spatial domain results in a cubic increase in complexity of a 2D simulation.

A similar but a computationally less intensive method is to incorporate multi-grid technique where mesh refinement is applied to areas with fine details as illustrated in figure 4.8b. In this method, only the required cells need

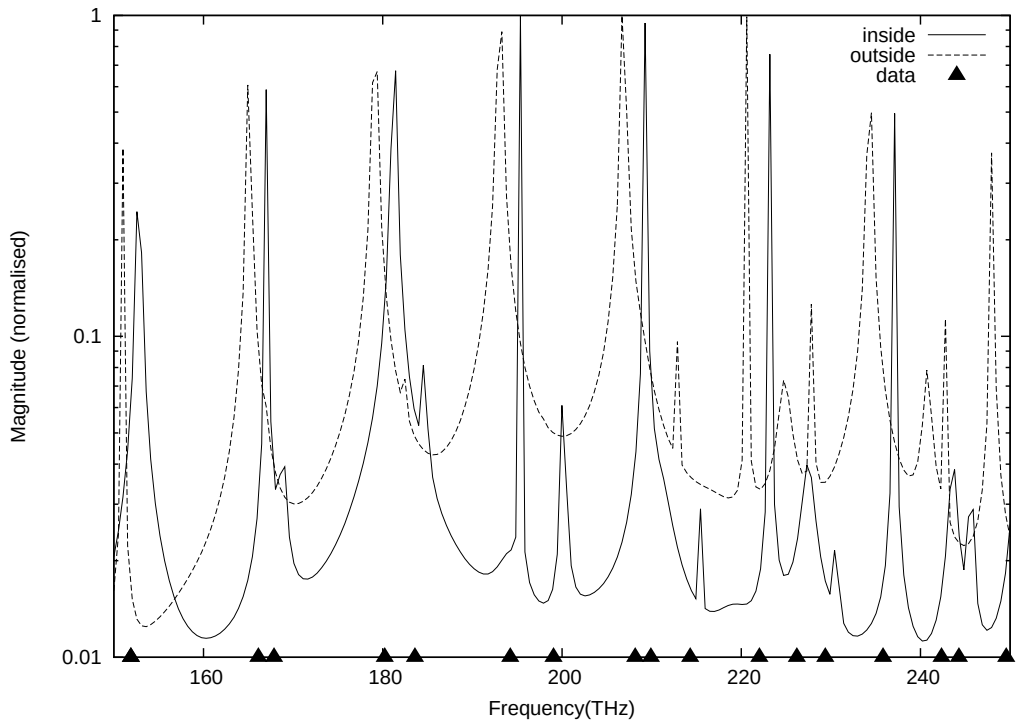

Figure 4.7: The energy spectrum of an infinite cylinder excited by a line source inside the resonator of E type waves for inside and outside discretisation along with the analytical resonant frequencies for step size of $0.0125\mu m$.

to be refined. The compromise of this method is that an approximation has to be made in connecting multiple links to multiple links of neighbouring cells. This disconnection applies to the time-step as well. The time-steps of smaller cells are smaller and that of the larger cells are larger and are multiples of powers of 2. These two approximations if handled properly lead to an efficient mesh refinement method.

CST Microwave Studio [10], a commercial implementation of TLM with a further optimised multi mesh (as of 2012), was use to observe the accuracy improvements obtainable by partially refining the mesh as mentioned above. CST simulation parameters were the same as the parameters given above except the space step and time step. The space step was allowed to vary

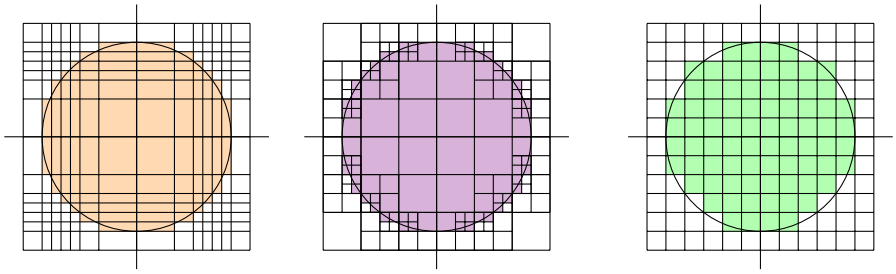

(a) Graded Mesh (b) Multi Mesh (c) Same Area

Figure 4.8: Alternative Meshing Techniques

between $\lambda_{min}/10$ and $\lambda_{min}/100$, where $\lambda_{min} = 1.2\mu m$. Since the CST is a 3D TLM implementation, the time step is at least $\sqrt{2}$ times smaller than that used in the 2D simulation throughout this study. However, the time complexity of the this CST simulation was similar to that of the 2D simulation for the step size of $0.025\mu m$ ($\approx \lambda_{min}/20$). The energy spectrum of the infinite cylinder obtained from the time domain CST simulation is given in figure 4.9.

The resonances were extracted from the time signals with a duration of $18000fs$ using difference Prony method. The medians of the resonant frequencies and Q factors obtained for each resonance are given in table 4.4. It should be noted that, when the resonances are extracted using matrix pencil and harmonic inversion, the resonant Q factors varied from that given in table 4.4. No two methods agreed with each other indicating that the approximations used in CST simulation imposes irregular noise affecting each resonant extraction method differently. Since the results from the difference Prony method were similar for time duration of $4000fs$, $8000fs$ and $18000fs$ its results were chosen to be presented here.

The error in the obtained resonant frequencies and Q factors compared to the analytical results presented in table 4.1 are plotted against theoretical values in figures 4.10 and 4.11 respectively. In table 4.1, WGM stands for whispering gallery modes and the mode number pair represent the azimuthal order and the radial order respectively.

As can be observed, the resonant frequency could be obtained with an er-

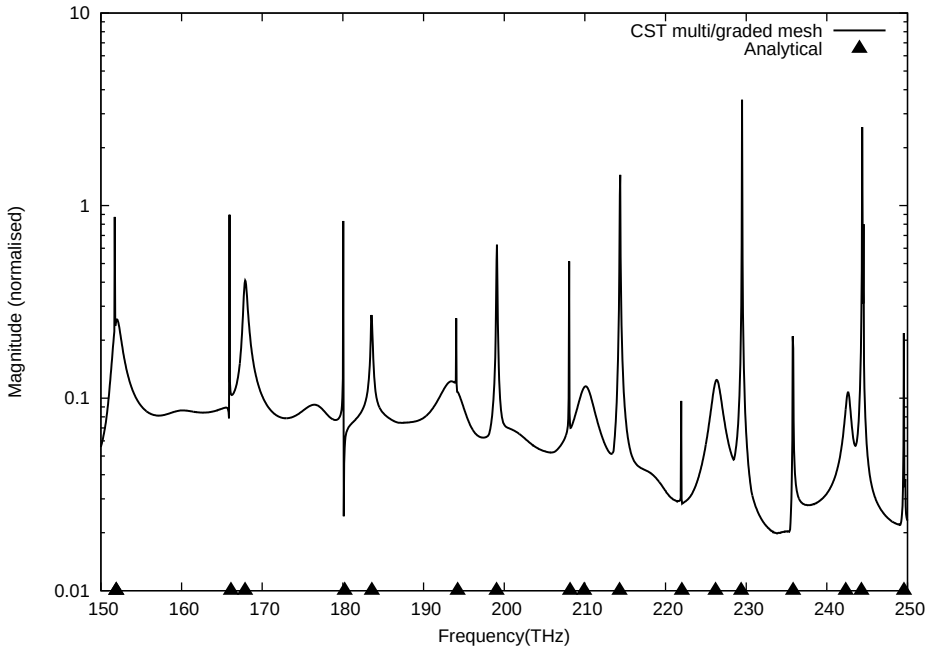

Figure 4.9: The spectrum of an infinite cylinder ($n = 2.82, r = 1.35\mu m$) excited by a line source inside the resonantor of E type waves as simulated by CST Microwave Studio with an optimised multi mesh with varying stepsize between $0.04\mu m$ and $0.004\mu m$.

ror less than 0.2% for all resonances of concern. However, a pattern for the resonance shifts cannot readily be observed. Hence, it is difficult to characterise the observed resonance shift and provide an explanation for cause of this error. This non uniform behaviour is mainly due to the non uniformity of the mesh. Therefore, it is difficult to predict the accuracy improvement obtainable by refining the mesh further.

On the other hand, the Q factor has a general trend of increasing error with the increasing theoretical Q factor. As observed, Q factors up to 10^5 could be obtained to within 10% error. In figure 4.11, the general trend of the error in Q factor of WGM(x,1) modes (i.e. 1st radial order modes) is lower than the general error trend in Q factor of WGM(x,2) modes (2nd radial order modes). The error trend of WGM(x,2) is lower than that of WGM(x,3), though this is not that clearly visible. This is opposite to what one would expect from

Table 4.4: The resonances obtained (using difference Prony method) from time responses of an infinite cylinder of $n = 2.82$ and $r = 1.35\mu m$ of a length of $18000fs$ simulated with CST Microwave Studio.

Resonance	Frequency	Q factor
WGM(9,1)	151.72	38496
WGM(6,2)	151.90	137
WGM(10,1)	165.938	217218
WGM(7,2)	167.871	305
WGM(11,1)	180.054	66684
WGM(8,2)	183.529	757
WGM(12,1)	194.551	25606
WGM(9,2)	199.09	1994
WGM(13,1)	208.047	4640860
WGM(10,2)	214.361	5681
WGM(14,1)	221.97	2713
WGM(8,3)	226.313	169
WGM(11,2)	229.489	15163
WGM(15,1)	235.797	443718
WGM(9,3)	242.666	324
WGM(12,2)	244.393	13022
WGM(16,1)	249.549	180252

a uniform mesh where WGM(x,1) Q factors are underestimated more than WGM(x,2) Q factors, etc since the stair-step approximation affects the modal volume of WGM(x,1) more. In multi mesh techniques, the opposite is true. The meshing becomes finer away from the centre towards the boundary. The TLM errors are then higher for coarse meshes further inside but lower for finer meshes closer to the boundary. This is a possible explaination of the results obtained using CST MW studio.

In conclusion, these mesh refinement techniques can be thought of as efficient alternatives to complete mesh refinement. Despite being able to obtain a resonably accurate result with comparatively small computational demand, the techniques' error characteristics vary from one situation to another.

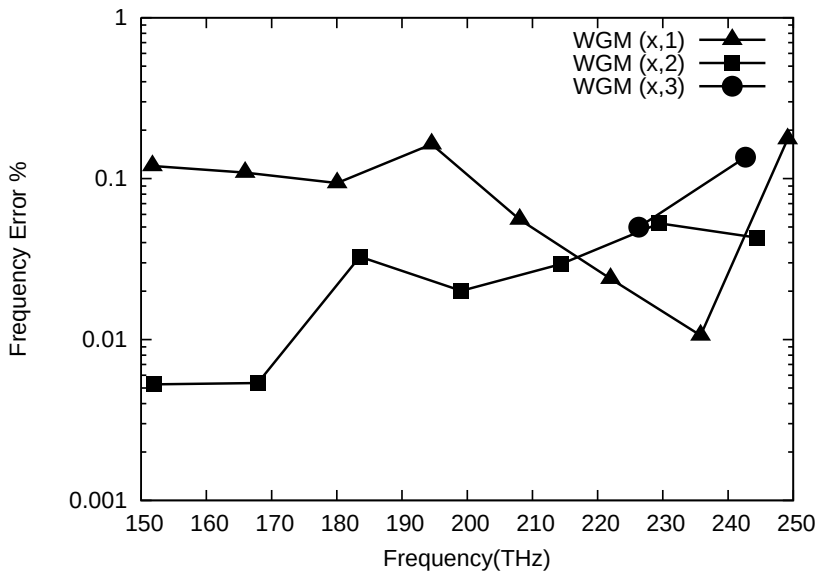

Figure 4.10: The percentage error of the resonant frequencies of the E wave modes supported by an infinite cylinder ($n = 2.82, r = 1.35\mu m$) modelled by CST Microwave Studio with a multi mesh with space step size varying between $0.04\mu m$ and $0.004\mu m$. 1st radial order modes are deonted by WGM(x,1), 2nd order modes by WGM(x,2) and 3rd order modes by WGM(x,3).

Hence, one cannot deduce the amount of refinement required to obtain a given accuracy level.

Therefore, in the next section some alternative discretisation techniques are explored that can be used to model non-Cartesian geometries using a Cartesian grid. It is shown that they behave slightly more predictively for the illustrative example of the infinite dielectric cylinder.

4.6 Same area Discretisation

An intermediate approximation, in which the modelled area is made closest to the actual area of the geometry was also considered and is illustrated in figure 4.8c. In this method, boundary cells are included in the geometry selectively according to the distance of the cell-centre to the actual boundary of the

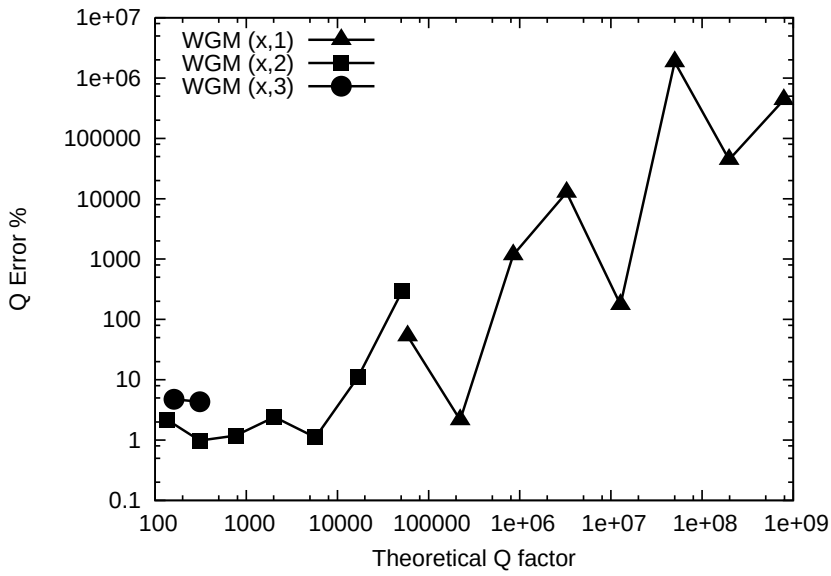

Figure 4.11: The percentage error of resonant Q factor of the E wave modes supported by an infinite cylinder ($n = 2.82, r = 1.35\mu m$) modelled by CST Microwave Studio with a multi mesh with space step size varying between $0.04\mu m$ and $0.004\mu m$. 1st radial order modes are deonted by WGM(x,1), 2nd order modes by WGM(x,2) and 3rd order modes by WGM(x,3).

geometry until the modelled geometry fulfils the aforementioned criterion. For a circle of radius r at $\mathbf{r_0} = (x_0, y_0, z_0)$, the distance to a cell-centre at $\mathbf{r_c} = (x_c, y_c, z_c)$ from the boundary will be $|\mathbf{r_c} - \mathbf{r_0}| - r$. A downside which soon becomes obvious is that geometries that are meant to be symmetrical might become assymetric due to the non uniform operation of selecting some boundary cells. Further it is unsuitable for situations illustrated by figure 4.1b, where it might produce a staggered edge. However, this approximation is now persued for circular geometries. The spectrum of the total energy inside the infinite cylinder defined previously is presented in figure 4.12 for three step sizes $0.05\mu m$, $0.025\mu m$ and $0.0125\mu m$ using the same area technique with a computational domain of $10\mu m \times 10\mu m$ truncated by TLM matched boundaries.

As can be seen from figure 4.12, unlike inside and outside discretisations,

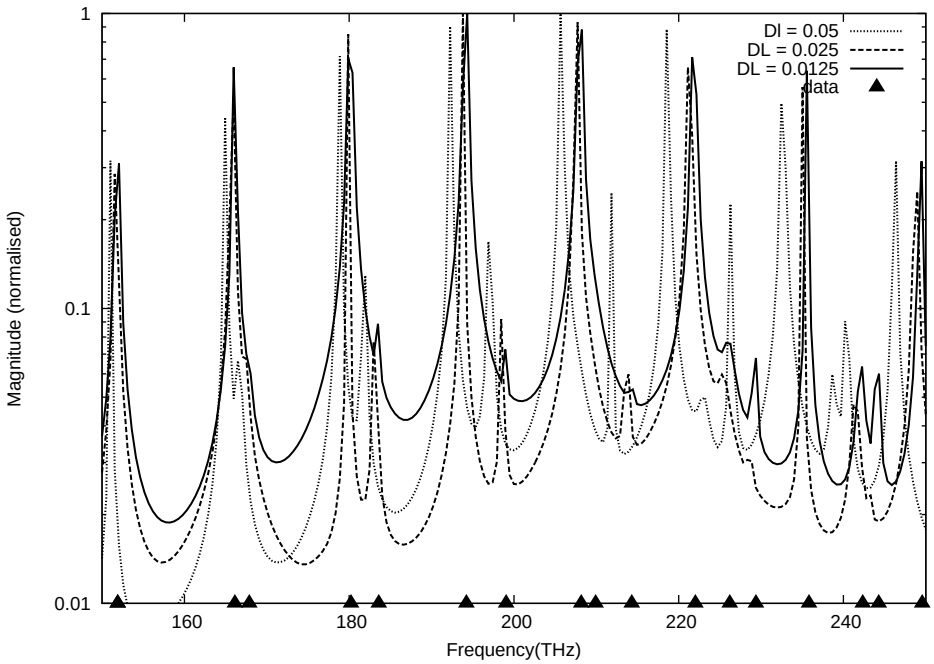

Figure 4.12: The energy spectrum of an infinite cylinder excited by a line source inside the resonator of E type waves for same area discretisation along with the analytical result for step sizes of $0.05\mu m$, $0.025\mu m$, and $0.0125\mu m$.

the same area results tend to converge to the analytical resonant frequencies. The amplitude of the baseline seems to be slightly higher for $\lambda/40$ ($0.0125\mu m$) step size indicating that the power loss is generally smaller. There is a significant error in resonant frequency predicted in $\lambda/10$ ($0.05\mu m$) step size towards the higher frequencies. This effect can be related to mesh dispersion, previously observed even when using inside and outside discretisations at the same step size. However, the curves seem to converge towards the analytical resonant frequencies when the step size is decreased. Therefore, the same area technique accurately represents the domain so that the resonant frequencies converges with decreasing step size.

Now that each resonant frequency is resonably accurately modelled as observed from the energy spectrum, the complex resonances (resonant frequency and Q factor) are extracted using the modified difference Prony method. The

complex resonances are extracted from all the time signals of duration of $4000fs$ at each measurable space point within the resonator, individually. The median of the complex resonances over the resonator is then calculated for each resonance and are presented in table 4.5. The error percentages in resonant frequency and Q factor are given in figures 4.13 and 4.14 respectively.

Table 4.5: Resonant frequencies and Q factors extracted from time signals of duration of $4000fs$ for an infinite cylinder ($n = 2.82, r = 1.35\mu m$) modelled with same area technique for step sizes of $0.05\mu m$, $0.025\mu m$, $0.0125\mu m$.

	Δl	$= 50nm$	Δl	$= 25nm$	Δl	$= 12.5nm$
WGM order	Res. Freq. (THz)	Q factor	Res. Freq. (THz)	Q factor	Res. Freq. (THz)	Q factor
WGM(6,2)	150.954	156	151.815	153	151.908	156
WGM(9,1)	151.048	3572	151.696	24641	151.843	53497
WGM(10,1)	165.004	1381	165.834	38395	165.987	146327
WGM(7,2)	166.668	342	167.607	331	167.807	326
WGM(11,1)	178.799	2092	179.868	17549	180.122	402087
WGM(8,2)	181.804	835	183.136	764	183.500	751
WGM(12,1)	192.341	3575	193.764	25952	194.126	646188
WGM(9,2)	197.094	2109	198.571	2157	198.922	2135
WGM(13,1)	205.783	21613	207.610	153406	208.004	129674
WGM(7,3)	207.495	106	209.291	98	209.444	101.409
WGM(10,2)	211.873	2977	213.728	6407	214.194	5247
WGM(14,1)	218.660	16066	221.319	363019	221.850	107892
WGM(8,3)	223.039	185	225.406	173		
WGM(11,2)	226.366	3073	228.629	10588	229.168	16314
WGM(15,1)	232.660	7124	235.019	239323	235.601	965641
WGM(9,3)	238.761	351	241.458	301	242.104	291
WGM(12,2)	240.400	832	243.372	5182	244.07	43075
WGM(16,1)	246.249	5435	248.767	40255	249.312	303433

According to figure 4.13, the error in resonant frequency is between 0.6-1% for a space step of $0.05\mu m$, 0.1-0.3% for a space step of $0.025\mu m$ and 0.03-0.1%

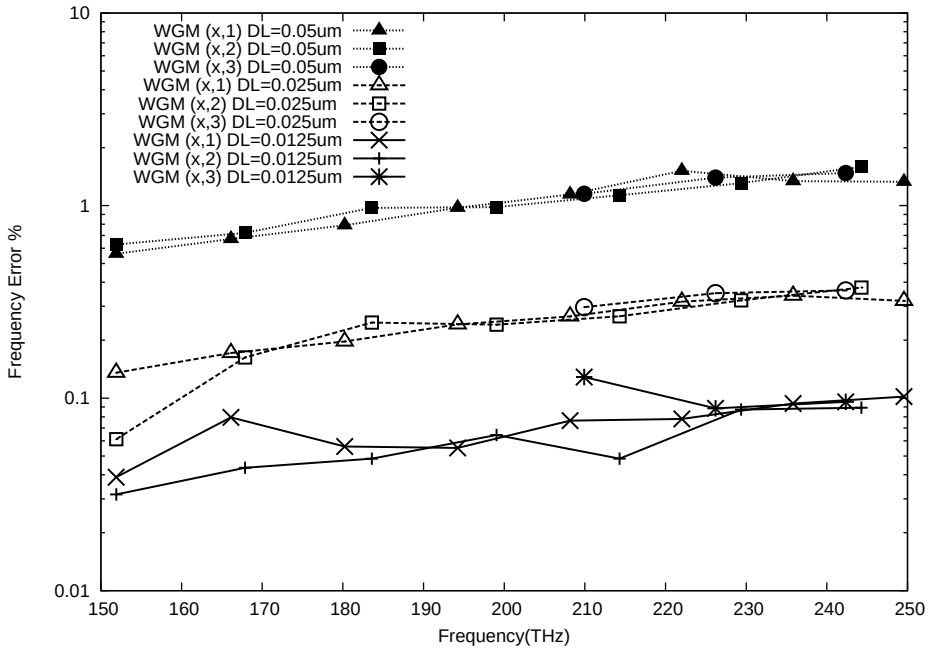

Figure 4.13: The percentage error of resonant frequencies of the an infinite cylinder ($n = 2.82, r = 1.35\mu m$) modelled by same area method with space steps of $0.05\mu m$, $0.025\mu m$ and $0.0125\mu m$.

for a space step of $0.0125\mu m$. The resonant frequency has a clear dependency on the space step and the error is decreased almost in proportion to the space step. The error in E waves observed using the finest mesh ($0.0125\mu m$) has some resonances (at $\approx 165THz$ and $210THz$) with slightly deviated error values from the general trend, which may have resulted from the extraction method's error in resolving close resonances.

The error in Q factor increases with the analytical Q factor over around 1000 according to figure 4.14. The error decreases by almost one order of magnitude when the space step is halved. The error is less than 10% for Q's of 2000 for $0.05\mu m$, 8000 for $0.025\mu m$ and 60000 for $0.0125\mu m$ step sizes. The Q factors tend to decrease with the surface roughness [11] with practical resonators. In this instance, the stair step approximation presented by the mesh is the source of an effective surface roughness in the structure simulated.

However, the errors obtained for the resonant frequency and Q factor are

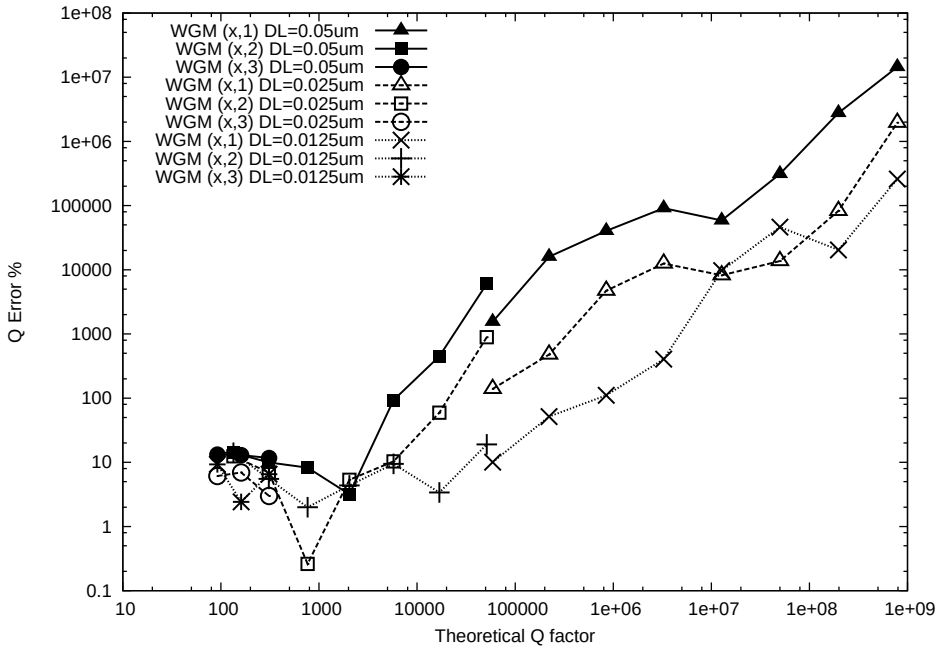

Figure 4.14: The percentage error of resonant Q factors of the an infinite cylinder ($n = 2.82, r = 1.35\mu m$) modelled by same area method with space steps of $0.05\mu m$, $0.025\mu m$ and $0.0125\mu m$.

higher than those observed using multi-mesh technique. Yet, the results are more orderly, and can be predicted to produce slightly better results than the multi-mesh approach when the space step is halved further ($\lambda_{min}/80$). But, the computation time complexity would in this case be 8 times that of the finest mesh used in this study.

In conclusion so far, the same area method provides an improvement over the inside and outside discretisations considering the resonant frequency. The simulated resonant frequency converge to the analytical values as the step size decreases. However, the Q factors are underestimated due to surface roughness still present in the same area discretisation technique. Hence, other discretisation techniques are considered next to solve the factor of the surface roughness and its detrimental effects on simulated Q factor.

4.7 Anti aliasing Discretisation

When a continuous signal is sampled, the samples should be able to represent the underlying continuous function. In other words, when a continuous function is reconstructed from the samples, it should be as close as possible to the original continuous function.

Nyquist's theorem states that if the original function's bandwidth is higher than twice the sampling frequency, the reconstructed signal from an infinite number of samples will not contain the higher frequency components present in the original function. In the following sub sections anti aliasing filtering in the spatial domain is discussed.

4.7.1 Reconstruct Rectangular Signal

Let us sample a rectangular function with a sampling interval of $T = 1/N$ within a domain of $[-1, 1]$. Samples between $-N/2$ and $N/2$ will have a value of 1. In total there will be $2N + 1$ samples.

A signal can be reconstructed from a set of samples using Nyquist interpolation defined by equation 4.28.

$$x(t) = \sum_{n=-N}^{n=N} x[n] \times \mathrm{sinc}_\pi \left(\frac{t - nT}{T} \right) \tag{4.28}$$

For example, the Nyquist interpolation method is used to reconstruct a continuous signal from the sampled rectangular function defined above. The reconstructed signal along with the original rectangular function is shown in figure 4.15 for a sampled rectangular signal of $N = 20$.

Figure 4.15 shows Gibbs oscillations at the discontinuities. The error of the reconstructed signal is maximum at the discontinuities and minimum at the point farthest from discontinuities. If the refractive index function in the spatial domain is represented as a rectangular function with sharp

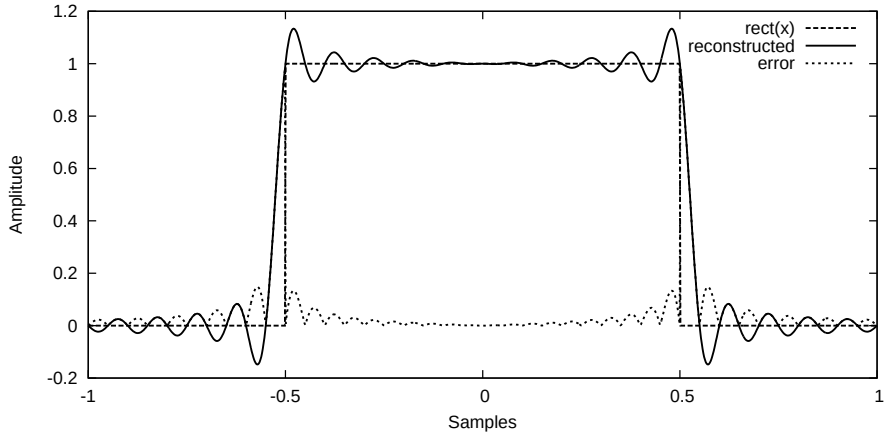

Figure 4.15: Reconstruction of a rectangular function sampled at 1/20 sampling interval, and the error of reconstruction compared to the original rectangular function

discontinuities, the underlying shape represented will model an error at the boundaries. In order to minimise this effect anti alias filtering is performed in digital signal processing of audio, images and video.

4.7.2 Anti-alias Filtering

The rectangular function therefore must pass through an anti-aliasing filter before sampling in order to avoid such oscillations. The resulting signal will have smooth edges instead of sharp variations. The anti aliasing filter should be selected so that the reconstruction best represents the original signal while eliminating high frequency signal components. In this section a sinc function, an Airy function, and a Gaussian function are compared to identify an anti-aliasing filters that preserves maximum detail.

Sinc Filter

The sinc filter is the normalised sinc function compressed by N as given by equation 4.29. Sinc filter has a sharp cut-off and so rejects high frequency components. While doing so, it introduces Gibbs oscillations at discontinuities,

which overshoot and undershoot. Even though overshoot is not particularly problematic, the undershoot becomes a problem if the lower level is zero, since negative material parameters are some times non-physical. However, in the spatial frequency domain, it acts as the benchmark.

$$sinc_{aaf}(x) = \mathrm{sinc}_{\pi}(Nx) \tag{4.29}$$

Lanczos Filter

Even-though the sinc filter is the ideal "brick wall" filter to let all frequencies within the bandwidth to pass though with uniform amplitude, it has some shortcomings. The Gibbs oscillations at step changes are unavoidable no matter how high the sampling rate is. The second problem is a limitation of applying the filter to arbitrary signal shapes via discrete convolution, because the filter extends to infinity. To overcome this second limitation, Lanczos filters are used. They are essentially sinc functions windowed by the main lobe of another sinc function to restrict its spread. The Lanczos filters are defined as,

$$L(x) = \begin{cases} \mathrm{sinc}_{\pi}(x)\,\mathrm{sinc}_{\pi}(x/a) & -a < x < a \\ 0 & \text{otherwise} \end{cases} \tag{4.30}$$

where $a = 1, 2, 3, \ldots$ controls the width of the filter. The Lanczos filter for a values larger than unity produces small undershoots to allow for more frequency content [12]. Therefore, only the $a = 1$ case is considered in this work. Since the filter for $a = 1$ defined as it is, the frequency rejection was poor. Hence, the filter is stretched by a factor of 2. Figures 4.16a and 4.16b shows the spacial domain and frequency domain characteristics of Lanczos filter for $a = 1$ defined as it is and when scaled by a factor of 2. This shows that the stretched Lanczos filter has the correct cut-off at 0.5. Hence, the

filter used is,

$$L_1(x) = \begin{cases} \text{sinc}_\pi \left(\frac{x}{2}\right)^2 & -2 < x < 2 \\ 0 & \text{otherwise} \end{cases} \tag{4.31}$$

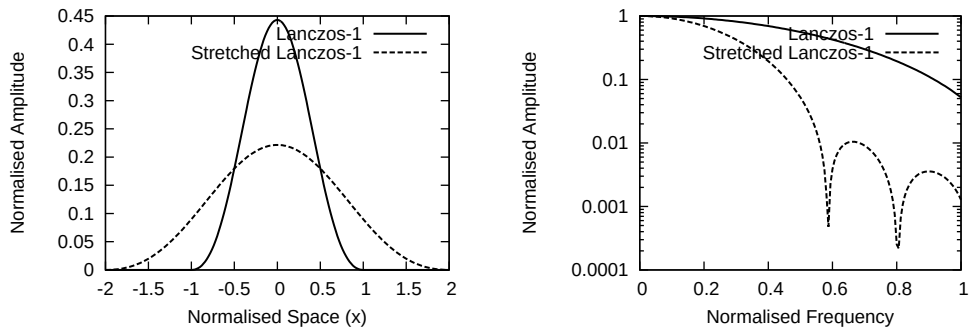

(a) Spacial Domain (b) Frequency Domain

Figure 4.16: Lanczos filter for $a = 1$ and the stretched Lanczos filter to improve frequency domain characteristics.

Airy Disc based Filter

The Airy disc is the most popular anti-aliasing filter in optical instruments since it is the natural diffraction pattern of a circular hole [12]. The Airy disc is thus propotional to the Franhouffer diffraction pattern. However, the Airy filter must be scaled by a factor of 1/2 in order to retain more low order frequencies. Figures 4.17a and 4.17b shows the spacial domain and frequency domain characteristics of the Airy filter and its stretched (compressed) function. The compressed function has the cut-off frequency near 0.5, whereas as the Airy filter does not. Hence, the filter can be defined by,

$$Ai_f(x) = \frac{J_1^2(2x)}{4x^2}$$

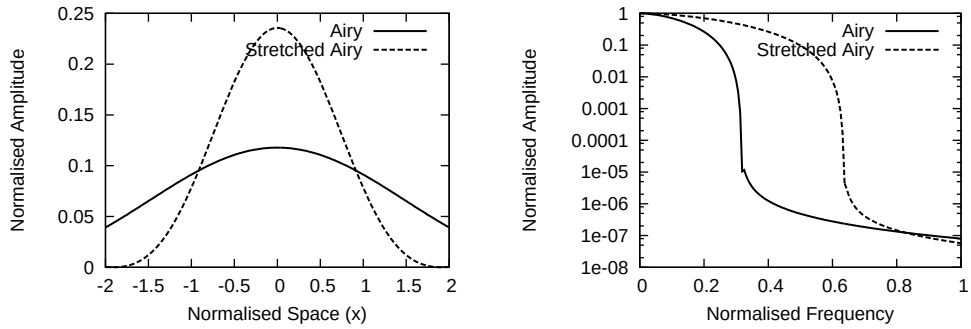

(a) Spacial Domain (b) Frequency Domain

Figure 4.17: Airy filter the stretched(compressed) Airy filter to improve frequency domain characteristics.

Gaussian Filter

The Gaussian function can also be used as an anti aliasing filter. However its practicality is only limited due to its broad frequency response. Stretching or compressing the Gaussian filter did not improve its poor frequency characteristics. Hence, the Gaussian filter is defined as,

$$\frac{1}{\sqrt{2\pi}}e^{-x^2} \tag{4.32}$$

Frequency Response of Filters

In order to preserve maximum detail (i.e. sharpest possible transition from zero to one in spacial domain) of the step response while cutting off the high frequencies. The frequency response of each filter is presented in figure 4.18.

According to figure 4.18, the sinc filter produces the best response in the frequency domain as the sinc filter exhibits a sharp cut-off at 0.5. The Airy filter seems to be a good alternative, but has inferior characteristics near cut-off. The Lanczos filter has similar characteristics as the Airy filter in the pass band and the cut-off region. The Gaussian filter is the worst of all showing no distinction between the pass and stop bands. Lanczos filter was chosen to be implemented over the Airy filter merely because the sinusoidal function is

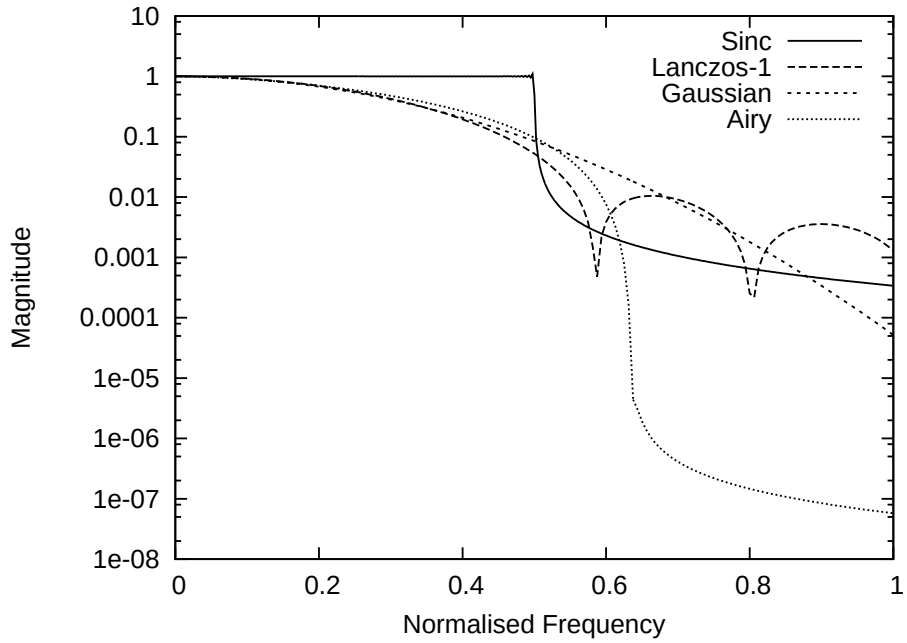

Figure 4.18: The normalised frequency response of the anti-aliasing filters

less resource intensive than the Bessel function to implement in a computer code. In general both of them are equally well suited.

4.7.3 Anti Aliasing in TLM

In two dimensional TLM, a normalised anti aliasing filter was used to determine the electrical susceptibility modelled at the centre (x_0, y_0) of a given cell (x_n, y_n). The filter is assumed to be truncated in the x,y directions at $-X/2$, $X/2$ and $-Y/2$, $Y/2$ expressed in space step units, respectively.

$$\chi_e[x_n, y_n] = \int_{-X/2}^{X/2} \int_{-Y/2}^{Y/2} f_{aa}(x, y) \chi_e(x\Delta l + x_0, y\Delta l + y_0)\, dx\, dy \tag{4.33}$$

where f_{aa} is the anti-aliasing filter function defined in the previous subsection.

The spread X and Y depends on the anti alias filter used. For a bounded filter such as Lanczos filter $a = 1$ the boundary is defined by $X = 4, Y = 4$. If the filter is unbounded, such as Gaussian or Airy filter, the filter must be

truncated.

Unlike same area discretisation, anti-aliasing discretisation can be used in both situations depicted in figures 4.1a and 4.1b. Note that this method also smoothes the edges of mesh conforming geometries. This is all in accordance with the sampling theorem.

4.7.4 Study of an Infinite Cylinder

The same cylinder studied throughout this chapter is now discretised using the anti aliasing method with the Lanczos filter and simulated with the parameters summarised in table 4.3 for a uniform mesh of step sizes of $0.05\mu m$, $0.025\mu m$, $0.0125\mu m$ The total energy within the resonator is presented in figure 4.19.

As observed with the same area technique, the resonances seem to converge to the analytical resonant frequency when the space step is decreased. Further, for the coarse mesh ($0.05\mu m$), there exists a significant error in predicting resonant frequencies at high frequencies due to modelling errors. These diminish when the mesh is made finer. The resonant frequencies and Q factors were extracted from the time signals of duration of $4000fs$ over the cylinder using the difference Prony method and the median value for each resonance is presented in table 4.6. The error of the resonant frequency and Q factor modelled by the anti aliasing method is given in figure 4.20 and 4.21 respectively for the same step sizes used previously.

The error in resonant frequency follows the same pattern observed in the same area method (i.e. increase with frequency and is proportional to the space step) but with slightly lower errors for each step size. In addition, except for the WGM(6,2) resonance at $\approx 150THz$, the error in resonant frequency for all resonances increases monotonically with resonant frequency.

The error in Q factor is significantly improved compared to both same area method and CST Microwave Studio muti mesh simulation. Even for a coarse mesh of $0.05\mu m$ (i.e. $\lambda_{min}/10$), the Q factor has a smaller error compared to the other two mesh refining techniques, despite the nearly 1% error in

Table 4.6: Resonant frequencies and Q factors extracted from time signals of duration of $4000fs$ within the cylinder ($n = 2.82, r = 1.35\mu m$) modelled with same area technique for step sizes of $0.05\mu m$, $0.025\mu m$, $0.0125\mu m$.

	Δl	$= 0.05\mu m$	Δl	$= 0.025\mu m$	Δl	$= 0.025\mu m$
WGM order	Res. Freq. (THz)	Q factor	Res. Freq. (THz)	Q factor	Res. Freq. (THz)	Q factor
WGM(6,2)	151.302	1.47×10^2	151.814	1.42×10^2	151.930	1.51×10^2
WGM(9,1)	151.440	4.92×10^4	151.792	5.86×10^4	151.865	5.93×10^4
WGM(10,1)	165.469	1.23×10^5	165.962	1.94×10^5	166.069	2.05×10^5
WGM(7,2)	166.983	3.26×10^2	167.669	3.25×10^2	167.822	3.25×10^2
WGM(11,1)	179.358	2.41×10^5	180.015	7.41×10^5	180.160	8.57×10^5
WGM(8,2)	182.405	7.53×10^2	183.303	7.46×10^2	183.507	7.46×10^2
WGM(12,1)	193.105	4.00×10^5	193.963	2.40×10^6	194.154	3.56×10^6
WGM(9,2)	197.527	2.15×10^3	198.681	2.15×10^3	198.944	2.12×10^3
WGM(13,1)	206.725	6.16×10^5	207.815	5.56×10^6	208.063	1.23×10^7
WGM(7,3)	207.774	9.90×10^1	209.486	9.73×10^1	209.771	9.61×10^1
WGM(10,2)	212.372	6.41×10^3	213.832	6.47×10^3	214.168	6.23×10^3
WGM(14,1)	220.242	1.03×10^6	221.584	1.07×10^7	221.899	4.09×10^7
WGM(8,3)	223.446	1.95×10^2	225.581	1.68×10^2	226.030	1.69×10^2
WGM(11,2)	226.976	1.37×10^4	228.793	1.72×10^4	229.211	1.65×10^4
WGM(15,1)	233.622	8.54×10^5	235.284	1.53×10^7	235.673	7.22×10^7
WGM(9,3)	239.159	3.20×10^2	241.553	2.94×10^2	242.122	2.88×10^2
WGM(12,2)	241.351	2.42×10^4	243.588	4.48×10^4	244.100	4.62×10^4
WGM(16,1)	246.884	5.12×10^6	248.915	8.73×10^6	249.389	9.54×10^7

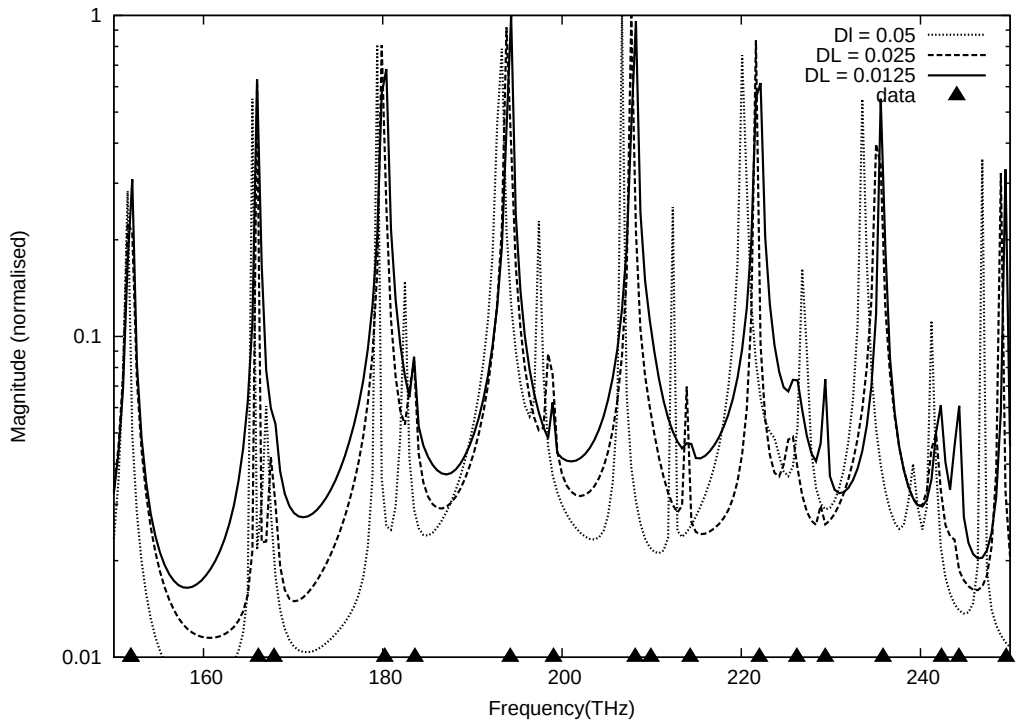

Figure 4.19: The energy spectrum of an infinite cylinder excited by a line source inside the resonator of E type waves for anti aliasing discretisation along with the analytical result for step sizes of $0.05\mu m$, $0.025\mu m$, and $0.0125\mu m$.

resonant frequency at that discretisation level. Further, the error in resonant frequency is reduced by a factor of 10, when the step size is halved.

By using anti aliasing methods, the influenced artificial surface roughness on high Q resonances is reduced for relatively coarse meshes. However coarse meshes produce a resonant frequency shift due to the inherent modelling errors such as TLM mesh dispersion [7].

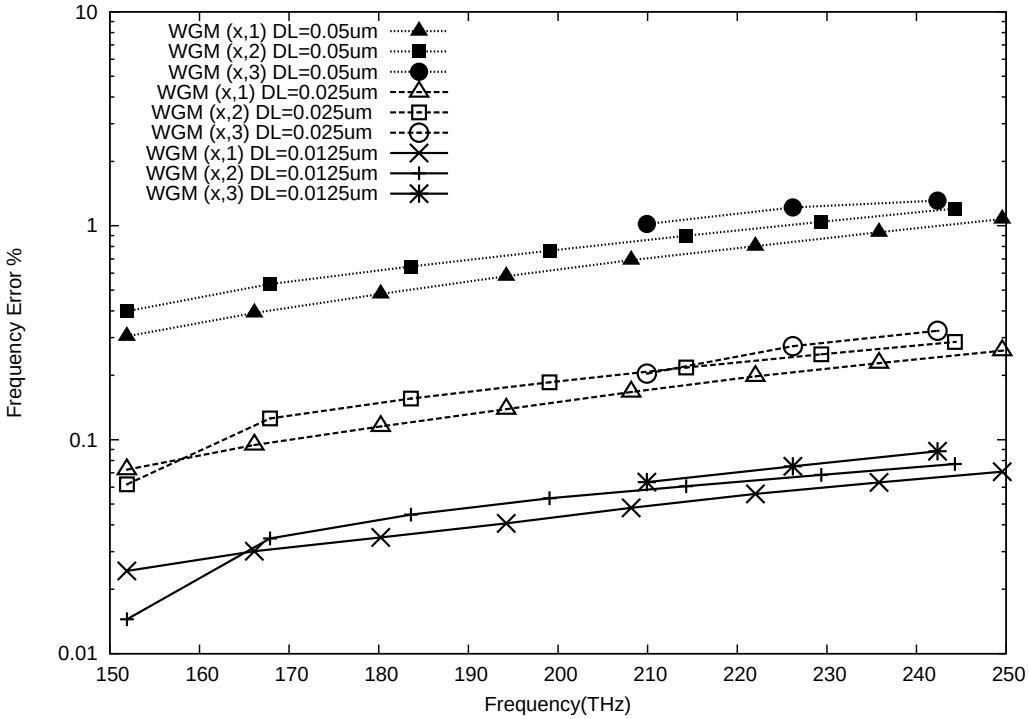

Figure 4.20: The percentage error of resonant frequencies of the an infinite cylinder ($n = 2.82, r = 1.35\mu m$) modelled by anti aliasing method with space steps of $0.05\mu m$, $0.025\mu m$ and $0.0125\mu m$.

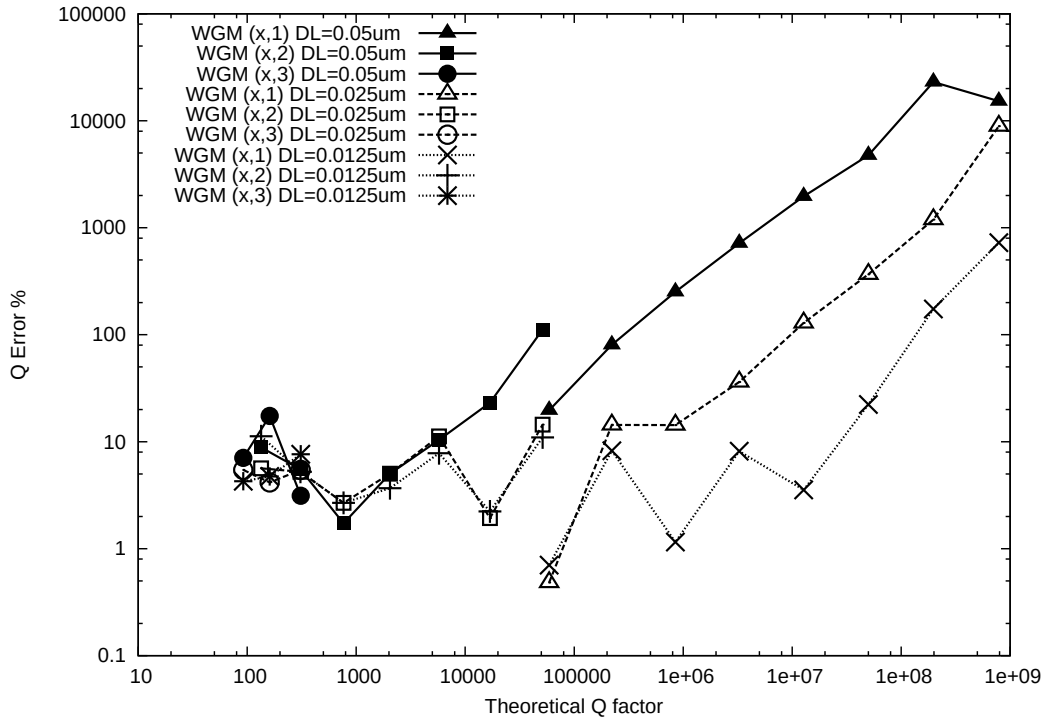

Figure 4.21: The percentage error of resonant Q factors of the an infinite cylinder ($n = 2.82, r = 1.35\mu m$) modelled by anti aliasing method with space steps of $0.05\mu m$, $0.025\mu m$ and $0.0125\mu m$.

4.8 Conclusions

In this chapter, the modelling of an infinite cylinder using TLM was considered. The problem was first solved analytically and the resonant frequencies and Q factors of an illustrative structure were obtained from the characteristic equation so obtained. Then using these results as a benchmark, the influence of certain well established limitations was investigated such as TLM mesh dispersion and stair case error in Cartesian meshes. Using standard discretising techniques, the cylinder was descretised and simulated to identify specific limitations regarding circular resonators as discussed in the literature. In the path to overcome these limitations, an optimised multi-mesh technique as used by CST Microwave Studio was considered. It produced reasonable results for the resonant frequency with an accuracy up to 0.2%, but the Q factor was severly underestimated despite using $\lambda/100$ as the smallest step size. In addition, the variation of the accuracy with the step size was unpredictable as the represented geometry affects different resonances differently and no pattern for the affects could be found. Therefore, a simpler method using standard TLM mesh was sought.

First a same area discretisation method, where the discretised geometry's area is made as close to the physical geometry as possible for the given mesh size, was considered. This provided results with lower accuracy than that of the multi-mesh method but was orderly and the affects were explainable. The error in Q factor was due to the stair stepping error which reduced in proportion to the mesh size. The resonant frequency was a function of TLM dispersion, which again could be reduced in proportion to the mesh size.

Then "anti-aliasing" the complete structure was considered. Initially the idea was to reduce the high frequency noise introduced by the stair step. A Lanczos filter was considered as the anti aliasing filter due to its good frequency and time domain (spatial domain) characteristics. The results were promising, in that it showed the same predictability as the same area method, but had much higher accuracy in the predicted Q factor. It is quite remarkable

that even with a coarse discretisation of $\lambda/10$, Q factor predicted using the anti aliased mesh was more accurate than using a $\lambda/100$ multi-mesh. The error in resonant frequency however, is of the same order as with the same area method. This provides further evidence that this error is a direct result of the TLM dispersion error.

Having established that TLM with antialiasing as an accurate numerical modelling technique the problem initiated by Boriskin *et. al* [1] can be reconsidered. Their concerns of resonance shift and Q factor estimation is well addressed by the studies in this chapter. However, it should be borne in mind that in the present study, the exact problem was not considered due to the boundary reflections in TLM matched boundaries used throughout this chapter to terminate the simulation domain. Therefore, in the next chapter, perfect matched layers are developed for TLM in order to provide better radiating boundary conditions at the edge of the simulation domain.

References

[1] A. V. Boriskin, S. V. Boriskina, A. Rolland, R. Sauleau, and A. I. Nosich, "Test of the FDTD accuracy in the analysis of the scattering resonances associated with high-Q whispering-gallery modes of a circular cylinder," *J. Opt. Soc. Am. A*, vol. 25, pp. 1169–1173, May 2008.

[2] A. N. Oraevsky, "Whispering-gallery waves," *Quantum Electronics*, vol. 32, no. 5, pp. 377–400, 2002.

[3] C. Müller, *Foundations of the mathematical theory of electromagnetic waves*. Springer Berlin, Heidelberg, New York, 1969.

[4] P. Debye, "Der lichtdruck auf kugeln von beliebigem material," *Annalen der Physik*, vol. 335, no. 11, pp. 57–136, 1909.

[5] P. Sewell, T. M. Benson, A. Vukovic, and A. A. Jarro, "The challenges for numerical time domain simulations of optical resonators," in *Trans-*

parent Optical Networks (ICTON), 2010 12th International Conference on, pp. 1–4, 2010.

[6] S. Boriskina, T. Benson, P. Sewell, and A. Nosich, "Spectral shift and q change of circular and square-shaped optical microcavity modes due to periodic sidewall surface roughness," *JOSA B*, vol. 21, no. 10, pp. 1792–1796, 2004.

[7] C. Christopoulos, *The transmission-line modeling method: TLM.* Institute of Electrical and Electronics Engineers, 1995.

[8] V. Trenkic, C. Christopoulos, and T. Benson, "Generally graded TLM mesh using the symmetrical supercondensed node," *Electronics Letters*, vol. 30, no. 10, pp. 795–797, 1994.

[9] J. Herring and C. Christopoulos, "Solving electromagnetic field problems using a multiple grid transmission-line modeling method," *Antennas and Propagation, IEEE Transactions on*, vol. 42, no. 12, pp. 1654–1658, 1994.

[10] M. Studio, "CST-computer simulation technology," *Bad Nuheimer Str*, vol. 19, p. 64289, 2008.

[11] M. L. Gorodetsky, A. A. Savchenkov, and V. S. Ilchenko, "Ultimate Q of optical microsphere resonators," *Optics Letters*, vol. 21, no. 7, pp. 453–455, 1996.

[12] M. Sonka, V. Hlavac, R. Boyle, *et al.*, "Image processing, analysis, and machine vision," 1999.

5

Perfectly Matched Layers for TLM

All numerical simulation techniques require truncation of the finite simulation domain. In some frequency domain techniques, the boundary can be defined to satisfy the radiating condition [1], [2]. In these formulations, the edge of the computational domain can be as small as the boundary of the geometrical objects of interest. However, for most time domain formulations including FDTD, FEM, TLM, the boundary of the simulation window is selected to cover the region of interest including extra space not belonging to geometrical objects of interest. Special treatment at the edge of computational domain is then required to impose a radiating condition.

The current most popular method is to terminate the simulation domain with perfect matched layers (PMLs), which consist of artificial absorbing material [3]. They are perfectly matched theoretically (hence the name), but in numerical models they can deviate from the ideal. PMLs have been proven to work exceptionally well in FDTD, but in TLM, their efficiency is significantly lower [4], [5]. Even though there exists several formulations for PMLs in TLM, their usage in everyday simulation problems is not yet widely accepted unlike in FDTD.

In this chapter, perfectly matched layers are implemented using a method originally proposed by J.Paul[6, 7] for 2D H waves and 3D. Some of its capabilities are studied for 2 dimensional E wave propagation and oblique angles of incidence. In addition, uniaxial PML and Convolutional PML, which have not yet been reported for TLM are studied as probable candidates for PML.

5.1 Motivation and Background

Until now in the simulation of optical resonators, a simple TLM matched boundary was used, where the end link is terminated with an impedance matched to the material of the end node. This has been able to produce adequate results in the case of the internally excited resonator. When the excitation is outside the resonator, most of the field will be scattered and the post-scattered results will include fields back scattered from the edge of the simulation domain. This problem applies to all excitation techniques including omni directional line sources, plane waves, and coupled waveguides.

In general, back-scattering from the edge of the computational domain is applicable to all wave simulation problems in TLM, but can be minimised or made irrelavent by making the computational domain large enough to isolate the problem of interest from the backscattered waves. In the case of optical resonators such isolation is ineffective due to the long run times required for resonators, during which time the scattered waves from the edge of the simulation domain find their way into resonators. Therefore, better boundary conditions are required when simulation tools are used in the context of optical resonators.

5.1.1 TLM Matched Boundary

Unlike FDTD, TLM computational domains can be terminated by an impedance matched to the material at the edge of the domain. However, due to TLM mesh dispersion, the impedance is not the same in every direction [8]. Therefore, it is unable to obtain matching condition for arbitrary angle of incidence.

As a guideline, the wave absorbing performance of simple TLM matched boundaries is now measured for varying angles of incidence.

For obtaining varying angles of wave incidence at the edge of the computational domain, a metal waveguide was truncated by the matched boundary. A metal waveguide of height h will propagate TE waves (E polarisation in z-direction, propagation along x, transverse axis y) waves in the fundamental mode TE01 when the wavelength λ satisfies $h < \lambda < 2h$ [1]. These waves at each wavelength (frequency) travel with different group velocities ($\lambda = 2h$ is the slowest, $\lambda = h$ is the fastest) and different ray angles θ. Figure 5.1 illustrates such a metal waveguide truncated by a TLM matched boundary.

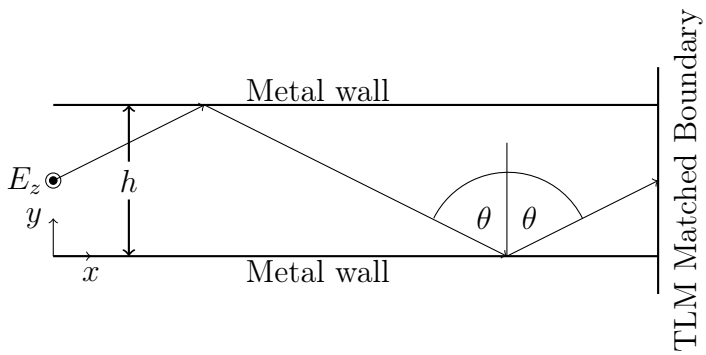

Figure 5.1: Illustration of a metal waveguide and ray representation of a TE polarised wave with a TLM matched boundary

The well-known relationship between wavelength and ray angle for the fundamental TE01 mode is given by [1],

$$\cos\theta = \frac{\lambda}{2h} \tag{5.1}$$

Hence, a pulsed wave consisting of different frequencies propagating in the fundamental mode will be incident at $(90^\circ - \theta)$ to the boundary. Therefore, reflection of the 2D TLM matched boundary can be observed for varying angles of incidence by observing the reflection of a pulse.

A waveguide of height $h = 1\mu m$, and length $l = 400\mu m$ filled with air was modelled in TLM with a space step size $\Delta l = 0.05\mu m$. The top and bottom

(y-plane) boundaries were defined as metal by a short circuiting the end links (i.e. reflection coefficient of -1). The left hand size x-plane boundary was kept at matched condition, but it does not affect the simulation since the waveguide is long. The waveguide was excited with a pulsed line source at $x = 300\mu m, y = 0.5\mu m$ with a centre frequency of $225THz$, and Gaussian pulse width of $10fs$. The field was observed in the plane of $x = 350\mu m$. The simulation was run for $1600fs$. The incident (E_z^i) and the reflected waves (E_z^r) were seperated from the time domain, and the reflection was calculated according to,

$$\Gamma(f) = \frac{\sum_{y=0}^{y=1\mu m} \mathcal{F}\{E_z^r(x = 350\mu m, y)\}}{\sum_{y=0}^{1\mu m} \mathcal{F}\{E_z^i(x = 350\mu m, y)\}} \tag{5.2}$$

where $\mathcal{F}\{\}$ is the discrete Fourier transform calculated with an fast Fourier transform (FFT), and f is frequency. Figure 5.2 shows the reflection at the matched boundary against frequency, along with the angle of incidence relationship with frequency.

According to figure 5.2, the reflection is minimum when the angle of incidence is 45°. At this angle, the 2D TLM matched boundary is completely matched, since the mesh dispersion is minimum at 45° [8]. From figure 5.2, it is evident that the reflection increases when the angle of incidence moves away from 45°. This agrees with TLM mesh dispersion, which is maximum along the principal axes [8].

This suggests that for extreme angles the reflection is more than $-20dB$ in general and specially between 44° - 46°, the reflection is well below $-40dB$. Since, optical resonators radiate energy in all directions (not necessarily equally), better boundary conditions are required to achieve $-120dB$ for the simulation of the externally excited cylindrical resonator [9].

5.1.2 Berenger's Perfectly Matched Layers

In contrast to the approach taken by the TLM matched boundary, Berenger proposed to add layers of absorbing material outside the boundary so that the

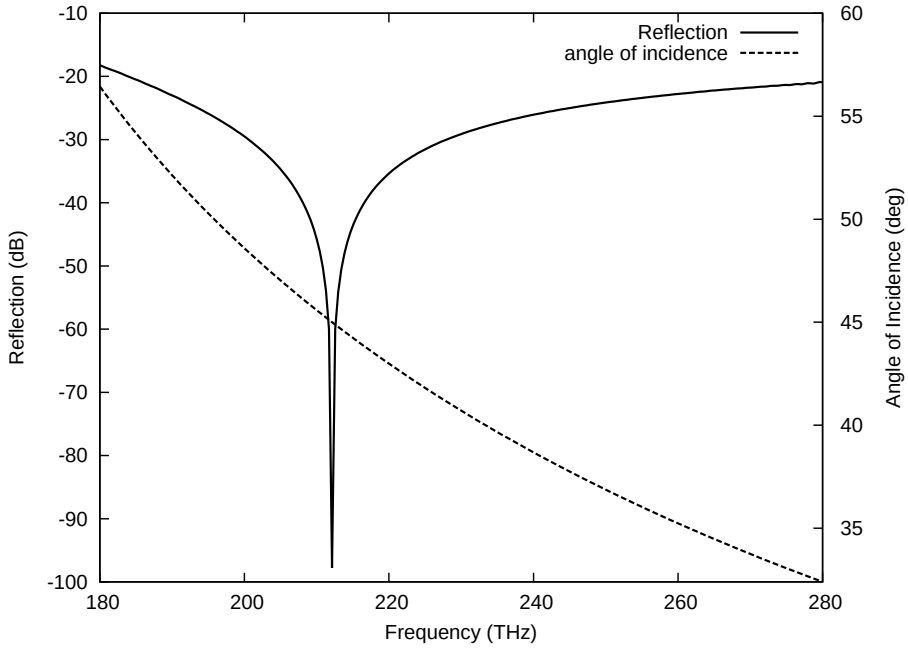

Figure 5.2: Reflection of a metal slab waveguide of height $h = 1\mu m$, supporting the fundamental TE01 mode, at a TLM matched boundary along with angle of incidence relationship with frequency.

field attenuates within the absorbing material [10], [11], given that the wave impedances of the materials on either side of the boundary are the same. In order to match the wave impedance of a non-magnetic material to a material with loss (conductance), one should satisfy the following condition within the absorbing layer [10].

$$\frac{\sigma_e}{\varepsilon} = \frac{\sigma_m}{\mu_0} \tag{5.3}$$

where σ_e, σ_m are electrical and magnetic conductances respectively. However, due to modelling error in ε, σ_e and σ_m, which varies with wavelength, the condition cannot be satisfied at all frequencies in a numerical method. Therefore, one must also make sure that the conductance is increased gradually in space to minimise reflection to an acceptable level. In FDTD, parabolic profiles are widely used even though better profiles are obtained using a fourth order polynomial or a geometric profile [12].

When considering a two or three dimensional PML, waves propagating normal to the boundaries must be absorbed without affecting the wave propagating tangential to the boundaries. In the method proposed by Berenger, each field component is split into two orthogonal directions, which are also orthogonal to the direction of the field component (e.g. E_z is split as $E_{zx} + E_{zy}$) [10]. This allows one to absorb only the component normal to the boundary plane (e.g. for an x-plane boundary only E_{zx} is absorbed keeping E_{zy} intact). Therefore, the conductances are split between two components to represent this anisotropic absorption. For instance, the x directed electric and magnetic conductances are split as, $\sigma_e = \sigma_{ex} + \sigma_{ey}$ and $\sigma_m = \sigma_{mx} + \sigma_{my}$.

The material types to be used in a two dimensional TLM model is illustrated in figure 5.3.

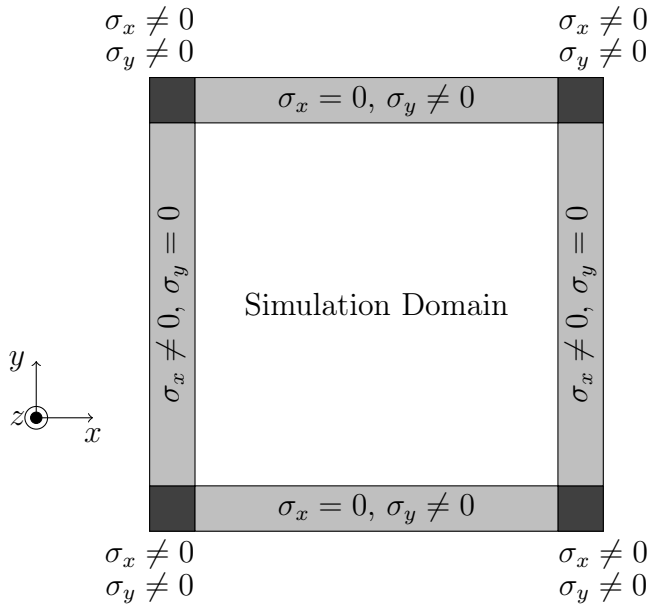

Figure 5.3: Illustration of PML material properties at the boundary

This formulation was proposed and implemented for the finite difference time domain (FDTD) method in both 2D and 3D [10], [11]. PMLs were first employed in TLM via interfacing it with an FDTD PML at the mesh boundary using TLM to FDTD field transformations [13], [14]. Pena *et.*

al first implemented a TLM implementation of a PML using an anisotropic node and a source term to cancel out the extra conductance modelled [4]. All of these implementations in TLM report reflections of $-55dB$ (FDTD interfacing) to $-60dB$ (anisotropic TLM) with 25 PMLs at the end of a WR-28 metal waveguide for a range of angles of incidence at the boundary. Equivalent FDTD PMLs have shown reflections around $-100dB$. A 3D Symmetrical Condensed Node (SCN) was formulated by Dubard *et. al* [5] with an approach similar to that taken in FDTD formulation and reported some improvement over the method proposed by Pena *et. al* [4]. This method was further characterised with various conductivity profiles by Maguier *et. al* , who report about $-70dB$ reflection with 20 PMLs, which is again far less efficient compared to the FDTD PMLs. Most importantly, for some profiles, the TLM method has shown some instability [15]. On an entirely different path, a split field implementation by Paul [6, 7] was used to observe the response of 3D freespace cubic cavity below $-60dB$, with 5 PMLs. However, further characterisations (with varying angles of incidence) were not followed.

In this study, the latter mentioned method was formulated for E-waves following a similar path in order to characterise and better understand the split field method.

5.1.3 Uniaxial Perfect Matched Layers

One of the main concerns raised following the proposal of Berenger's PML was that the splitting of field components is non-Maxwellian. Further, its application was limited to structured coordinate systems [16]. A Maxwellian PML was introduced by Gedney [16] as a solution which has since then been known as Uniaxial PML, which was shown to be equivalent to Berenger's PML. The method was also later explained by stretching of spatial coordinates to the complex domain [17] and this extended formulation is known as the complex frequency shifted (CFS) PML.

Considering a plane wave incident on the z boundary, let the Maxwell's

equations within the nonmagnetic PML material be,

$$\nabla \times \mathbf{E} = \omega\mu_0\bar{\bar{\mu}}\mathbf{H} \tag{5.4}$$

$$\nabla \times \mathbf{H} = -\omega\varepsilon_0\varepsilon_r\bar{\bar{\varepsilon}}\mathbf{E} \tag{5.5}$$

where $\bar{\bar{\mu}}$ and $\bar{\bar{\varepsilon}}$ are diagonal tensors representing the anisotropy, ε_r is the common factor of relative permittivity. By solving the Maxwell's equations and separating the modal solutions as transverse electric(TE) and transverse magnetic(TM), Gedney has obtained the conditions for zero reflection for both TE and TM modes at the boundary [16] as,

$$\bar{\bar{\varepsilon}} = \bar{\bar{\mu}} = \begin{bmatrix} a & & \\ & a & \\ & & \frac{1}{a} \end{bmatrix} \tag{5.6}$$

where a can be arbitrarily chosen to represent an absorbing material and, in [16], Gedney has selected $1+\sigma/j\omega\varepsilon_0$. It was also mentioned that one could use $\kappa + \sigma/j\omega\varepsilon_0$ to attenuate evanescent waves further. In order to generalise the material parameters for x, y boundaries and for corner regions, the following parameters are used

$$\bar{\bar{\varepsilon}} = \bar{\bar{\mu}} = \begin{bmatrix} \frac{s_y s_z}{s_x} & & \\ & \frac{s_x s_z}{s_y} & \\ & & \frac{s_x s_y}{s_z} \end{bmatrix} \tag{5.7}$$

where $s_i = 1 + \sigma_i/j\omega\varepsilon_0$ inside PML bounded by i-directed plane ($i = x, y, z$), and $s_i = 1$ elsewhere.

Due to the inferior performance of Berenger's PML in TLM despite a proven equivalence between FDTD and TLM [18] in 2D, this method was also implemented in TLM in this study as it has been successful in FEM and in other coordinate systems.

5.2 Berenger's PML Formulation

Considering E-waves let the electric field component $E_z = E_{zx}+E_{zy}$. Maxwell's equations for E-waves can then be re-expressed in condensed form as [10],

$$\begin{bmatrix} \frac{\partial H_y}{\partial x} \\ -\frac{\partial H_x}{\partial y} \\ -(\nabla \times E)_x \\ -(\nabla \times E)_y \end{bmatrix} = \frac{\partial}{\partial t} \begin{bmatrix} \varepsilon_0 E_{zx} \\ \varepsilon_0 E_{zy} \\ \mu_0 H_x \\ \mu_0 H_y \end{bmatrix} + \begin{bmatrix} \sigma_{ex} * E_{zx} \\ \sigma_{ey} * E_{zy} \\ \sigma_{my} * H_x \\ \sigma_{mx} * H_y \end{bmatrix} + \frac{\partial}{\partial t} \begin{bmatrix} \varepsilon_0 \chi_e E_{zx} \\ \varepsilon_0 \chi_e E_{zy} \\ 0 \\ 0 \end{bmatrix} \tag{5.8}$$

where $\sigma_{e(x,y)}$ and $\sigma_{m(x,y)}$ are the electrical and magnetic conductivities inside x and y plane boundaries, χ_e is dielectric susceptibility. In the frequency domain (s-domain) with usual normalisations, the condensed equation becomes,

$$\begin{bmatrix} \frac{\partial i_y}{\partial \bar{x}} \\ -\frac{\partial i_x}{\partial \bar{y}} \\ -(\bar{\nabla} \times V)_x \\ -(\bar{\nabla} \times V)_y \end{bmatrix} = \bar{s} \begin{bmatrix} 2V_{zx} \\ 2V_{zy} \\ i_x \\ i_y \end{bmatrix} + \begin{bmatrix} g_{ex} V_{zx} \\ g_{ey} V_{zy} \\ r_{my} i_x \\ r_{mx} i_y \end{bmatrix} + \bar{s} \begin{bmatrix} 2\chi_e V_{zx} \\ 2\chi_e V_{zy} \\ 0 \\ 0 \end{bmatrix} \tag{5.9}$$

Using Stokes' theorem to express spatial derivatives in terms of V_1, V_2, V_3, V_4,

$$\begin{bmatrix} (V_1 + V_2) \\ (V_3 + V_4) \\ -(V_3 - V_4) \\ -(V_1 - V_2) \end{bmatrix} = \bar{s} \begin{bmatrix} 2V_{zx} \\ 2V_{zy} \\ i_x \\ i_y \end{bmatrix} + \begin{bmatrix} g_{ex} V_{zx} \\ g_{ey} V_{zy} \\ r_{my} i_x \\ r_{mx} i_y \end{bmatrix} + \bar{s} \begin{bmatrix} 2\chi_e V_{zx} \\ 2\chi_e V_{zy} \\ 0 \\ 0 \end{bmatrix} \tag{5.10}$$

In the travelling wave format it becomes,

$$2 \begin{bmatrix} (V_1 + V_2) \\ (V_3 + V_4) \\ -(V_3 - V_4) \\ -(V_1 - V_2) \end{bmatrix}^i = \begin{bmatrix} (4 + g_{ex} + 2\bar{s}\chi_e) V_{zx} \\ (4 + g_{ey} + 2\bar{s}\chi_e) V_{zy} \\ (2 + r_{my}) i_x \\ (2 + r_{mx}) i_y \end{bmatrix} \tag{5.11}$$

From the normalisations $g_e = \sigma_e \Delta l \eta_0 \sqrt{2}$ and $r_m = \sigma_m \Delta l/(\eta_0\sqrt{2})$ [6], the perfect matching relationship becomes,

$$g_e = 2r_m(\chi_e + 1) \tag{5.12}$$

Note that this applies to separate x, y components of g_e and r_m.

5.2.1 Implementation Validity

The PML formulation given above now needs to be validated after implementing in TLM. The most important theoretical assumptions made in Berenger's PML formulation [10] is the wave velocity and the impedance matching between freespace and the PML absorbing material. In TLM the impedance and the phase velocity depend on frequency as well as the direction of propagation. To this end, the impedance and the phase velocity of freespace angles varying between zero and 45° are considered first, as given in figure 5.4. The impedance was calculated by observing the electric and magnetic fields emitted by a line source in freespace at specific angles. For transverse electric and magnetic fields, i.e. TEM mode, the wave impedance is given by,

$$Z(\theta, f) = \frac{E(\theta, f)}{H(\theta, f)} \tag{5.13}$$

where θ is the angle of propagation, and $Z(\theta, f)$ takes a value of $\sqrt{\mu_0/\varepsilon_0} \approx 120\pi\Omega$ for freespace in theory [1].

As can be seen from figure 5.4, the wave impedance of the TLM mesh at 45° is the closest to the theoretical value of 376.7Ω. The wave impedance increases when the angle deviates from 45° with maximum error when propagating parallel to Mesh axes. This complies with the TLM dispersion as discussed in [8]. Therefore, a theoretical PML can only be perfectly matched at 45° with minimum reflection; the relationship between g_e and r_m obtained previously ($g_e = 2r_m$) is only valid at 45°. Every angle of incidence has a unique relationship between g_e and r_m, for which the reflections are mini-

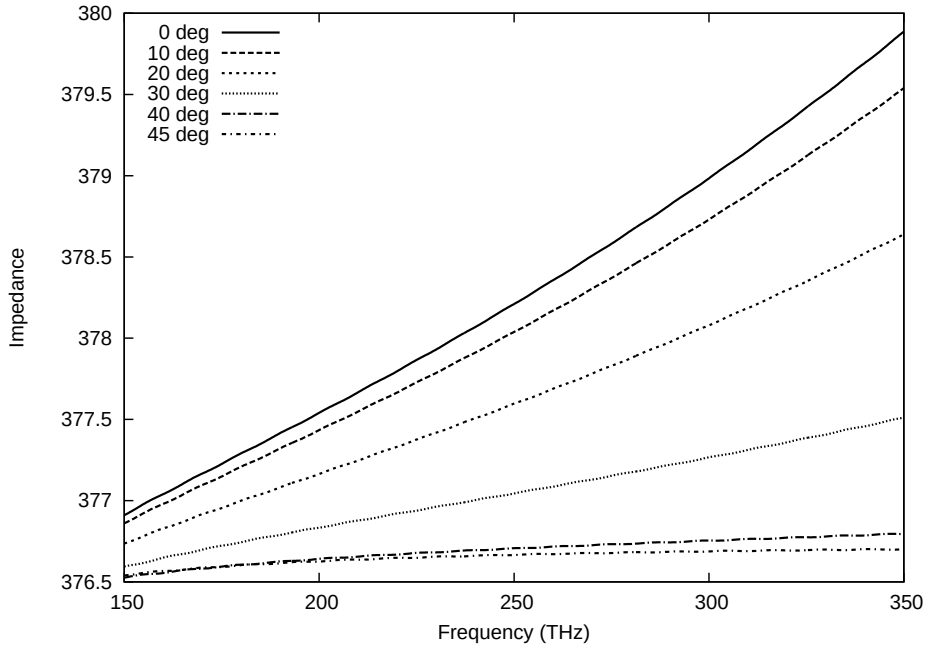

Figure 5.4: The impedance of freespace as modelled by 2D TLM with a space step of $0.05\mu m$ at various angles of propagation.

mum at the freespace-PML boundary. At 0°, this relationship is $g_e = 4r_m$.

In this light, the wave impedance mismatch between freespace and the PML was calculated. At a given frequency and direction both deviate from the theory, but if the mismatch can be minimised, the reflection at the freespace-PML boundary can be minimised. The error value at each frequency was calculated as,

$$Z_{err}(f) = \sqrt{\frac{\int_0^{2\pi} \left(Z_{fs}(\theta, f) - Z_{pml}(\theta, f)\right)^2 \, d\theta}{2\pi}} \tag{5.14}$$

where Z_{fs} is the impedance of freespace as modelled by TLM, Z_{pml} is the impedance of PML as modelled by TLM.

The electrical conductivity σ_e of the PML was set as $\approx 9.76(mho/nm)$, where $\Delta l = 0.05\mu m$. The mismatch in wave impedance measured when $g_e = 2r_m$ (as per the theoretical relationship), and when $g_e = 4r_m$ is given in

figure 5.5. The factor of 4 was chosen for reasons, which will become clear in the next subsections.

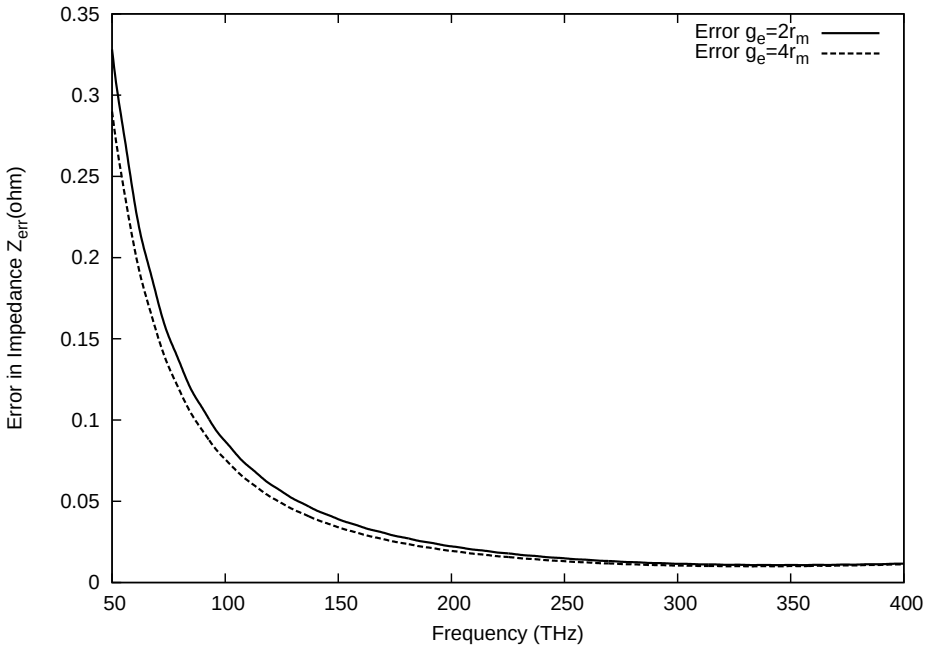

Figure 5.5: Impedance mismatch between freespace and PML integrated over propagating angles as a function of frequency when the normalised electrical and magnetic conductivities are related by $g_e = 2r_m$ and $g_e = 4r_m$.

As can be seen, the impedance mismatch is worse for the theoretical $g_e = 2r_m$ (when all angles are given uniform importance). The mismatch increases for low frequencies and flattens out with finite error and increases slowly again at high frequencies.

In addition to impedance, phase velocity is another factor affecting the reflection at the freespace-TLM boundary. The error in phase velocity was calculated by measuring the phase change observed between two close spacial positions for zero and 45° propagation for g_e/r_m ratio of 1,2,4 and are given in figures 5.6 and 5.7.

According to figure 5.6, when the propagation is parallel to a mesh axis, the phase velocity error is smallest when the theoretical relationship between

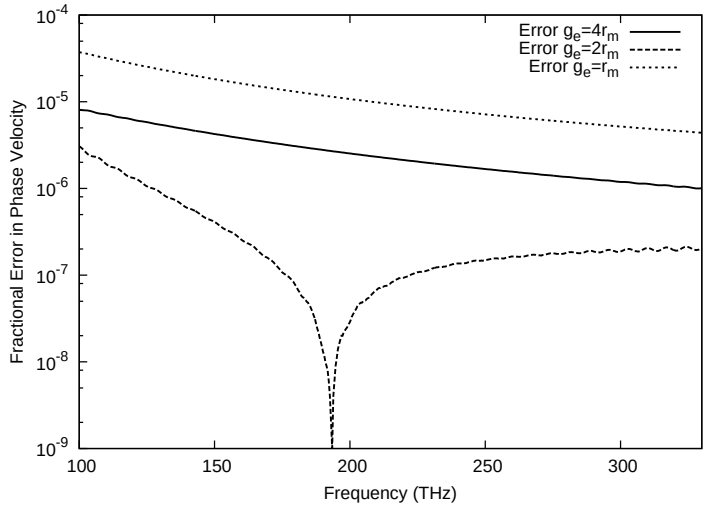

Figure 5.6: The error in phase velocity relative to that of TLM freespace phase velocity, when propagating parallel to an axis

g_e and r_m is obeyed. The phase velocity error is a minimum at a particular frequency and it was observed that the particular frequency at which this happens depends on the conductivity of the PML.

According to figure 5.7, the phase velocity error at 45° propagation is still minimum when $g_e = 2r_m$. In this case, the velocity error has improved both at the low frequency and high frequency ends. The other curves haven't changed much from the axial propagation case.

The error in phase velocity is higher when $g_e = 4r_m$ for both parallel and 45° propagation. The magnitude of the error however is small,less than 0.01%. Hence, the PML material is shown to be nearly matched to the free space considering the phase velocity.

According to the results obtained so far, a clear winning relationship between g_e and r_m could not be obtained, as impedance matching is better when $g_e = 4r_m$ and the phase velocity matching is better when $g_e = 2r_m$. Next, the conductivity profile and the reflection at the freespace-PML boundary is considered.

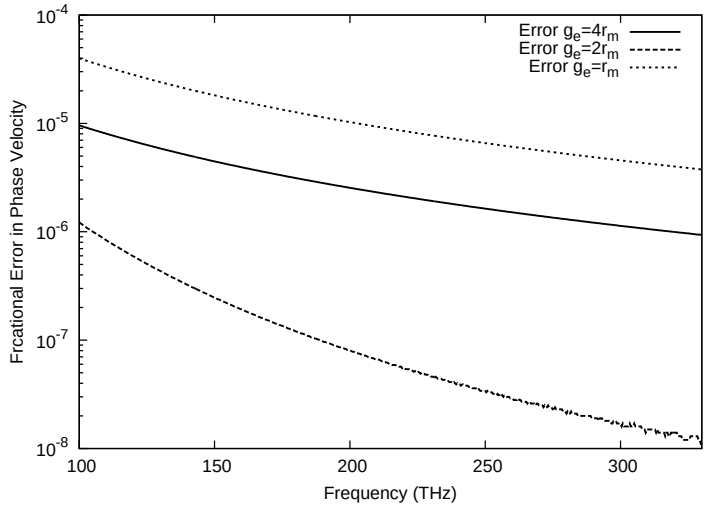

Figure 5.7: The error in phase velocity relative to that of TLM freespace phase velocity, when propagating at 45° to main axes.

5.2.2 PML Conductivity Profile

Since theoretically, the material into PML interface is matched, there should be no reflection back into the simulation domain. However, due to modelling error existing in all numerical techniques, there exists a reflection whenever the material parameters differ. Since the reflection is dependant on frequency and direction, a universal perfect matching condition does not exist.

This also makes clear that, if there is no material parameter change, there exists no reflection. Hence, for a uniform conductivity profile in the PML region only an initial reflection will be present if the PML absorbing region is significantly long. Thus, reflections at the boundary between freespace and PML with a uniform conductivity profile are initially studied. Table 5.1 shows the simulation parameters, where a 2 dimensional simulation window with periodic boundary conditions in the y-direction was excited with a Gaussian pulsed plane wave in freespace to observe the reflections.

Figures 5.8a and 5.8b shows the reflection back to freespace and the amplitude of the field after 25 PML layers.

When a constant conductivity profile is used within the PML, the reflection

Table 5.1: Simulation parameters used in order to observe the reflections at a freespace-PML boundary at normal incidence

Window Size	$X = 50\mu m$
	$Y = \infty$
PML Width	$X_{PML} = 25\mu m$
Space step	$0.05\mu m$
Excitation line	$x = 30\mu m$
Excitation Centre Frequency	$f_0 = 200THz$
Gaussian Pulse width	$t = 1fs$
Measurement line (incident + reflection)	$x = 40\mu m$
Measurement line (absorption + transmission)	$x = 52.5\mu m$

at the boundary decreases in proportion to the conductivity. According to figure when conductivity is decreased by a factor of 10, the reflection reduces by -20dB indicating the proportionality. The amount of absorption however decreases exponentially when conductivity decreases, which is the expected behaviour theoretically. If one requires at least $-R_{pml}$ (dB) reflection from the PML boundary, the conductivity of the first PML cell must be selected so that the freespace-PML reflection is below the required reflection level. This is a necessary condition regardless of the conductivity profile or the depth of the PML. Since this reflection arises due to discretisation (i.e. non-ideal) of Maxwell's equations, the reflection should diminish when the step size is decreased. The reflection at three space step sizes are shown in figure 5.9.

The reflection at the freespace-PML boundary decreases by 6dB when the step size is decreased by a factor of 2. This shows that, the reflection is proportional to the step size. The formula for freespace-PML reflection in the discretised case can thus be presented as,

$$R_D \propto \sigma \Delta l \tag{5.15}$$

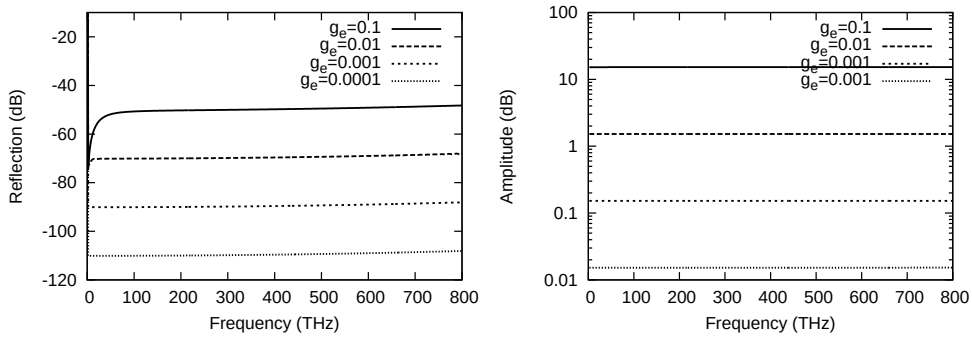

(a) Reflection (b) Amplitude after 25 PMLs

Figure 5.8: The Reflection and the Amplitude after 25 PML layers for a constant conductivity profile when $g_e = 4r_m$

Therefore, the total reflection from the PML boundary can be written as,

$$R_{pml} = R_D + R_C R_B \tag{5.16}$$

$$R_C = exp\left[-\frac{2}{\varepsilon_0 c}\int_0^\delta \sigma(\rho)\, d\rho\right] \tag{5.17}$$

where R_C is the attenuation of the field through the PML layer of depth δ, R_D is the reflection due to discretisation error, and R_B is the reflection at the end of the PML. Usually in FDTD $R_B = 1$ since, a perfect electric conductor is used at the end of the PML. But in TLM, a matched boundary condition can be used, which will give an additional attenuation of $10 - 15$ dB as observed in subsection 5.1.1. For a uniform conductivity profile R_D is almost uniform as observed in figure 5.8a. The optimum conductivity profile $\sigma(\rho)$ should then produce minimum R_D for a given R_C.

Let a normalised conductivity profile be,

$$\hat{\sigma}(\rho) = \frac{\sigma(\rho)}{\int_0^\delta \sigma(\rho)\, d\rho} = \frac{\sigma(\rho)}{\sigma_0} \tag{5.18}$$

Then,

$$R_C = exp\left[-\frac{2}{\varepsilon_0 c}\sigma_0\right] \tag{5.19}$$

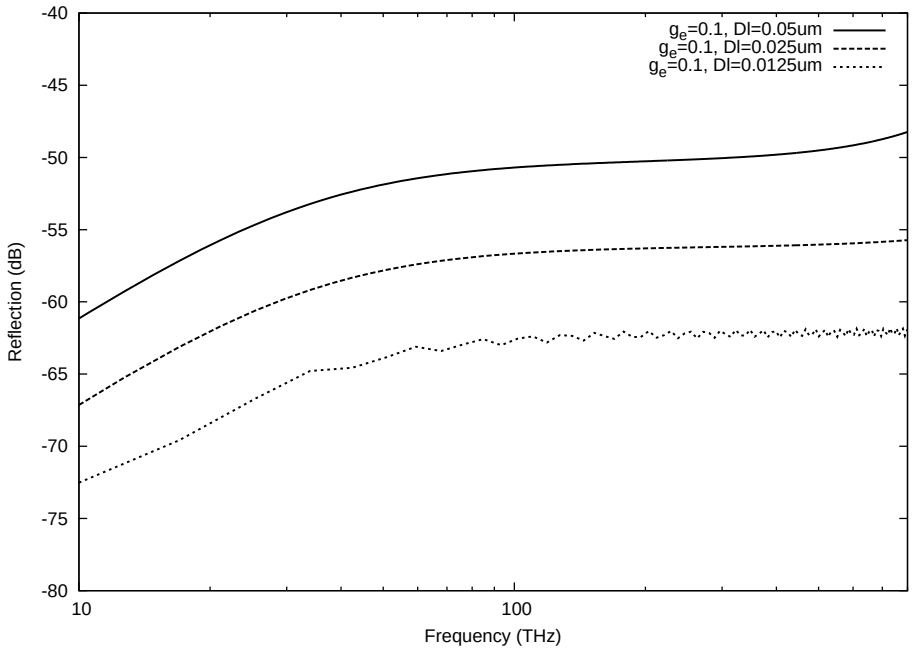

Figure 5.9: The reflection at the freespace-PML boundary for space step sizes of $0.05\mu m$, $0.025\mu m$, and $0.0125\mu m$ when g_e=0.1, r_m=0.025;

where R_C is the required attenuation through the PML layer. The conductivity profile $\sigma(\rho) = ln(R_C)\hat{\sigma}(\rho)$

$$\sigma_0 = \frac{-R_{C(dB)}}{40\eta_0 \log_{10}(e)} \tag{5.20}$$

Hence, the TLM conductivity $g_e(\rho) = g_{e0}\hat{\mathbf{g}}_e(\rho)$ is obtained by normalising σ_0, where

$$g_{e0} = \left(\frac{-R_{C(dB)}}{40\log_{10}(e)}\right)\sqrt{2} \tag{5.21}$$

$$\hat{\mathbf{g}}_e(\rho) = \hat{\sigma}(\rho)\Delta l \tag{5.22}$$

For a given PML cell, the spatial average of $g_e(\rho)$ within the cell is used as the conductivity value $g_e(\rho_n)$ of the cell.

For a polynomial conductivity profile of the form ρ^m,

$$\hat{\mathbf{g}}_e(\rho_n) = \frac{(n+1)^{m+1} - n^{m+1}}{N^{m+1}} \tag{5.23}$$

where N is the depth of the PML in integer number of cells.

The effectiveness of this approach is discussed in the next subsection.

5.2.3 Reflection at Freespace-PML Boundary

The reflection at the freespace-PML junction is the most important factor in PML-characteristics. If the reflection is low enough, the wave energy transmitted into the PML in principle can be absorbed with a large enough number of layers to reduce subsequent reflections. Since reflections for various angles of incidence needs to be considered, the metal waveguide used previously in this chapter to benchmark matched boundary is used to represent angles within the range 30° - 60°. A plane wave propagating in an equivalent 1D mesh (i.e. 2D mesh with periodic boundary conditions in y-direction) is used to represent normal incidence. The initial plane wave reflection for a quadratic profile of 25 layers when R_C is $10dB, 20dB, 30dB$ and $40dB$ was evaluated for normal incidence for $g_e = 2r_m$ and $g_e = 4r_m$, and the results are given in figure 5.10. The initial reflection was observed by extending the profile at the conductance value at the 25th layer uniformly for a long distance. The metal waveguide reflection was measured when $R_C = 10dB, 20dB$ and the results are given in figure 5.11.

The figures 5.10 and 5.11 show the best possible reflection obtainable from a quadratic profile of 25 layers. From the figure 5.10, it is evident that the PML is highly effective above a certain frequency. When the the overall conductivity (i.e. requird attenuation) of a given profile is decreased, this "threshold" frequency is decreased. For $g_e = 4r_m$, all profiles could produce a reflection better than $-65dB$ for normal incidence beyond the threshold. For $g_e = 2r_m$, this value is about $-45dB$. It was found by numerical experiment that out of many relationships, $g_e = 4r_m$ seems to produce the smallest

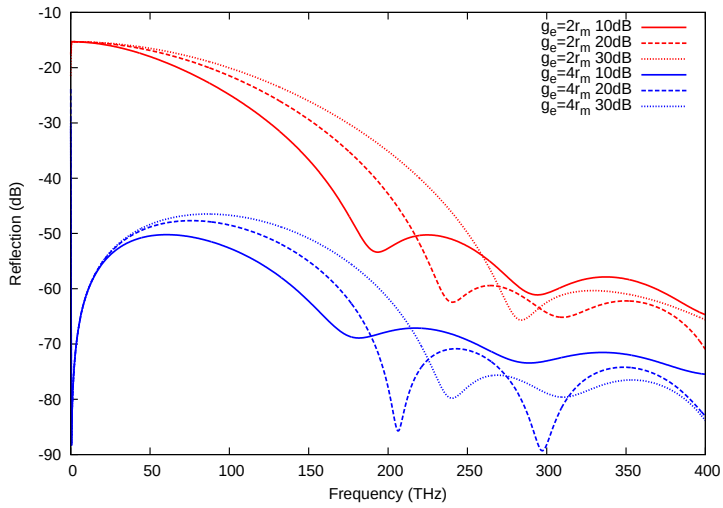

Figure 5.10: Reflection of a plane wave for $R_C = 10dB, 20dB, 30dB, 40dB$ and $g_e = 2r_m$, $g_e = 4r_m$ when the conductivity profile is quadratic and 25 PML layers are used.

reflection for any given profile for normal incidence. Therefore, when 1D propagation is modelled with 2D TLM by periodic boundary conditions in one dimension, it is advantageous to use $g_e = 4r_m$.

The reflection results for 2D waveguide propagation according to figure 5.11 indicates that $g_e = 2r_m$ relationship is better. As shown in figure 5.2, in the case of a matched boundary, for $g_e = 2r_m$, at 45° propagation, the reflection is at its smallest. In this test $g_e = 4r_m$ behaves relatively poorly. In general, the reflection is higher when the angle of incidence is higher. This property though mentioned in general for FDTD for split field formulation [16], is not evident in the PML formulations presented by Pena and Ney [4] or Dubard and Pompei [5]. This may be partly due to the fact that their formulations are Maxwellian and anisotropic but the split field term is achieved by other means (such as a compensating source). The quadratic conductivity profile they have used had a maximum of $10S/m$. For the space step of $0.23mm$ their maximum $g_e = 1.226$, whereas in the case of $R_C = -10dB$ in the presented model maximum $g_e = 0.188$, which is more than 6 times smaller when the conductivity value they have used is normalised. If the conductivity

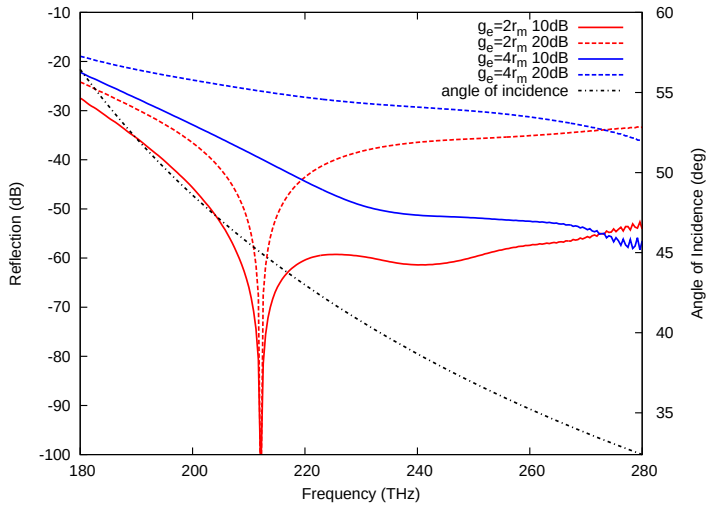

Figure 5.11: Reflection of TE01 mode from a metal waveguide PML junction for $R_C = 10dB, 20dB$ and $g_e = 2r_m$, $g_e = 4r_m$ along with the angle of incident at each wavelength when the conductivity profile is quadratic.

is increased to the value give by Pena and Ney, the initial reflection will be much higher than -55dB (value for $R_C = -10dB$). This indicates that the performance of their PMLs is much better than that presented here.

Despite the small error in impedance and velocity demonstrated in section 5.2.2, the presented PML is not well suited for large angles of incidences. It can however provide a better boundary condition to TLM than the matched boundary provided enough PML layers are used. But its efficacy is much less compared to that previously presented by Pena and Ney [14, 4] and Dubard and Pompei[5]. The only advantage in this formulation is its simplicity in formulation and implementation.

5.3 Uniaxial PML Formulation

Having done the literature review of uniaxial PML technique, in this section the method is implemented in TLM.

Consider an x-directed boundary plane. For a frequency independent σ,

the relative permittivity tensor is given by [16],

$$\bar{\bar{\varepsilon}} = \bar{\bar{\mu}} = \begin{bmatrix} 1 - \frac{\sigma}{j\omega\varepsilon_0+\sigma} & & \\ & 1 + \frac{\sigma}{j\omega\varepsilon_0} & \\ & & 1 + \frac{\sigma}{j\omega\varepsilon_0} \end{bmatrix} \tag{5.24}$$

In the relative permittivity and permeability tensor, the real part corresponds to refraction while the imaginary part corresponds to conductance. As can be seen, the x-directed conductivity is negative indicating that the x-directed components are amplified. This also has an implication on stability. In stub loaded TLM, including z-domain models, the time step is at its maximum satisfying the Courant condition ($\Delta l/\Delta t \leq \sqrt{2}c$). Hence, any negative conductivity increases the phase velocity causing instability. This does not directly affect 1D propagation as the Courant condition becomes $\Delta l/\Delta t \leq c$, which can be satisfied by the 2D mesh up to some values of conductivity.

In order to find the limiting condition for stability, the phase velocity in the y-direction (direction transverse to the x-boundary plane) is formulated as follows.

$$v_p = \frac{1}{\sqrt{\mu\varepsilon}} = \frac{1}{\sqrt{\mu_0\varepsilon_0}\left(1 - \frac{\sigma}{j\omega\varepsilon_0+\sigma}\right)} = \frac{c}{\left(1 - \frac{\sigma}{j\omega\varepsilon_0+\sigma}\right)} \tag{5.25}$$

According to equation 5.25, at very high frequency the wave velocity within the PML material becomes closer to that of freespace. At very low frequency wave velocity becomes infinite indicating zero permittivity and permeability.

Assume a relationship between Δl and Δt in the mesh as,

$$u_{TLM} = \frac{\Delta l}{\Delta t} = \zeta c \tag{5.26}$$

where ζ is a "slowing down" parameter. Hence,

$$\zeta > \sqrt{2\left(1 + \frac{\sigma^2}{\omega^2\varepsilon_0^2}\right)} \tag{5.27}$$

Several techniques can be used to decrease the time step in TLM. The simplest but the least efficient method is using the stub loaded symmetric condensed node(SCN) [19]. The hybrid symmetric condensed node(HSCN)[19] and Super symmetric condensed node(SSCN)[19] are better alternatives to achieve stability. Since a stub loaded SCN was used throughout this study, extension of this seemed to be the path of least resistance. Therefore a stub loaded 2D symmetric condensed node was used to implement the uniaxial PML in TLM.

5.3.1 TLM Formulation

In the stub loaded 2D mesh, let

$$u_{TLM} = \frac{\Delta l}{\Delta t} = \sqrt{2} v_r c \tag{5.28}$$

$$Z_{TL} = \sqrt{2} \frac{\eta_0}{v_r} \tag{5.29}$$

where $v_r \geq 1$ is the scaling factor for Δt required for stability for the given conductivity. Until now, v_r was unity, representing freespace (ε_0, μ_0) as the background material. The permittivity and the permeability modelled by the link lines (see chapter 2) when $v_r > 1$ are,

$$\varepsilon = \frac{2\Delta t}{Z_{TL}\Delta l} = \varepsilon_0 \tag{5.30}$$

$$\mu = \frac{Z_{TL}\Delta t}{\Delta l} = \frac{\mu_0}{v_r^2} \tag{5.31}$$

When $v_r > 1$ to satisfy the Courant condition for the negative conductivity, the deficit in the permeability can be added by short circuited stubs (representing inductance) for each direction to match the material properties. The characteristic inductance of a short circuited stub is $Z_L = 2L/\Delta l$, where L is the inductance represented by the short circuited stub [8]. In order to represent a permeability of μ_0 , the inductance per unit length in one direction

with the stub should be equal to μ_0,

$$L_d = \frac{Z_{TL}\Delta t}{\Delta l} + \frac{Z_L \Delta t}{2\Delta l} = \mu_0 \tag{5.32}$$

Hence, the characteristic impedance of the added stub is given by,

$$Z_L = 2Z_{TL}(v_r^2 - 1) \tag{5.33}$$

The voltage equation 2.21 for the stub formulation given in chapter 2 will be unaltered while the current equations 2.22 and 2.23 are modified [8]. Hence the field calculation equations become,

$$V_z = \frac{V_1^i + V_2^i + V_3^i + V_4^i}{2} \tag{5.34}$$

$$I_x = \frac{2V_2^i - 2V_1^i + 2V_{Lx}^i}{2Z_{TL} + Z_L} \tag{5.35}$$

$$I_y = \frac{2V_3^i - 2V_4^i + 2V_{Ly}^i}{2Z_{TL} + Z_L} \tag{5.36}$$

where V_{Lx}^i and V_{Ly}^i are the incident voltages of x directed and y directed inductive stubs respectively. The scattered voltages of the inductive stubs are given by,

$$V_{L(x,y)}^r = Z_{L(x,y)} I_{(x,y)} - V_{L(x,y)}^i \tag{5.37}$$

When deriving the above equations, loss-free conditions are assumed as followed previously in chapter 2. The z-domain model given in chapter 2 includes conductivity as g_e and r_m. Since both formulations are identical for freespace, by analogy with the equations 5.34, 5.35 and 5.36 the stub loaded equations in the z-domain can be obtained as,

$$2\begin{bmatrix} (V_1 + V_2 + V_3 + V_4) \\ -(V_3 - V_4 - V_{Lx}) \\ -(V_1 - V_2 - V_{Ly}) \end{bmatrix}^i = \begin{bmatrix} (4 + g_{ez} + \bar{s}2\chi_e)V_z \\ (2 + (\frac{Z_L}{Z_{TL}}) + r_{mx} + \bar{s}\chi_m)i_x \\ (2 + (\frac{Z_L}{Z_{TL}}) + r_{my} + \bar{s}\chi_m)i_y \end{bmatrix} \tag{5.38}$$

where the normalised z-directed electrical conductivity $g_{ez} = \sigma_{ezz}\Delta l Z_{TL}$, the normalised x-directed magnetic conductivity $r_{mx} = \sigma_{mxx}\Delta l/Z_{TL}$, the normalised y-directed magnetic conductivity $r_{my} = \sigma_{myy}\Delta l/Z_{TL}$, σ_{ezz} is the z directed electrical conductivity, σ_{mxx} is the x directed magnetic conductivity, σ_{myy} is the y directed magnetic conductivity.

Let us now consider the relative permittivity and permeability tensor of UPML material of a general boundary (i.e. x-directed, y-directed, corner) using equation 5.7.

$$\bar{\bar{\varepsilon}} = \bar{\bar{\mu}} = \begin{bmatrix} 1 + \frac{\sigma_y - \sigma_x}{j\omega\varepsilon_0 + \sigma_x} & & \\ & 1 + \frac{\sigma_x - \sigma_y}{j\omega\varepsilon_0 + \sigma_y} & \\ & & 1 + \frac{\sigma_x\sigma_y}{j^2\omega^2\varepsilon_0^2} + \frac{\sigma_x + \sigma_y}{j\omega\varepsilon_0} \end{bmatrix} \tag{5.39}$$

The Maxwell's equations for the PML material for a 2 dimensional E-wave formulation in the frequency domain are now given by,

$$\begin{bmatrix} -(\nabla \times \mathbf{H})_z \\ (\nabla \times \mathbf{E})_x \\ (\nabla \times \mathbf{E})_y \end{bmatrix} = \begin{bmatrix} j\omega\varepsilon_0 E_z \\ j\omega\mu_0 H_x \\ j\omega\mu_0 H_y \end{bmatrix} + \begin{bmatrix} \varepsilon_r \left(\frac{\sigma_x\sigma_y}{j\omega\varepsilon_0} + \sigma_x + \sigma_y \right) E_z \\ j\omega\mu_0 \left(\frac{\sigma_y - \sigma_x}{j\omega\varepsilon_0 + \sigma_x} \right) H_x \\ j\omega\mu_0 \left(\frac{\sigma_x - \sigma_y}{j\omega\varepsilon_0 + \sigma_y} \right) H_y \end{bmatrix} + \begin{bmatrix} j\omega\varepsilon_0\chi_e E_z \\ 0 \\ 0 \end{bmatrix} \tag{5.40}$$

where σ_x, σ_y are conductivities as illustrated in figure 5.3. In equation 5.40, the first vector on the R.H.S represents field in freespace, the second vector on the R.H.S represents field due to conductivities, and the third vector on the R.H.S represents field due to susceptibilities. Hence,

$$\sigma_{ezz} = \varepsilon_r \left(\frac{\sigma_x\sigma_y}{j\omega\varepsilon_0} + \sigma_x + \sigma_y \right) \tag{5.41}$$

$$\sigma_{mxx} = j\omega\mu_0 \left(\frac{\sigma_y - \sigma_x}{j\omega\varepsilon_0 + \sigma_x} \right) \tag{5.42}$$

$$\sigma_{myy} = j\omega\mu_0 \left(\frac{\sigma_x - \sigma_y}{j\omega\varepsilon_0 + \sigma_y} \right) \tag{5.43}$$

After conductivity normalisations and substituting $j\omega = s = \bar{s}/\Delta t$ [6],

$$g_{ez}(\bar{s}) = \varepsilon_r \left(\frac{\gamma_x \gamma_y}{2} \frac{1}{\bar{s}} + \gamma_x + \gamma_y \right) \tag{5.44}$$

$$r_{mx}(\bar{s}) = \frac{\bar{s}(\rho_y - \rho_x) v_r^2}{\bar{s} + \rho_x} \tag{5.45}$$

$$r_{my}(\bar{s}) = \frac{\bar{s}(\rho_x - \rho_y) v_r^2}{\bar{s} + \rho_y} \tag{5.46}$$

$$\gamma_x = \frac{\sigma_x \Delta l \sqrt{2} \eta_0}{v_r} \qquad \rho_x = \frac{\gamma_x}{2} \tag{5.47}$$

$$\gamma_y = \frac{\sigma_y \Delta l \sqrt{2} \eta_0}{v_r} \qquad \rho_y = \frac{\gamma_y}{2} \tag{5.48}$$

Transforming to the z-domain ($\bar{s} = 2(1 - z^{-1})/(1 + z^{-1})$) results in,

$$g_{ez}(z) = g_{ez0} + z^{-1} \left\{ \frac{g_{ez1}}{1 - z^{-1}} \right\} \tag{5.49}$$

$$r_{mx}(z) = r_{mx0} - z^{-1} \left\{ \frac{r_{mx1}}{(2 + \rho_x) + z^{-1}(\rho_x - 2)} \right\} \tag{5.50}$$

$$r_{my}(z) = r_{my0} - z^{-1} \left\{ \frac{r_{my1}}{(2 + \rho_y) + z^{-1}(\rho_y - 2)} \right\} \tag{5.51}$$

where

$$g_{ez0} = \varepsilon_r \left(\gamma_x + \gamma_y + \frac{\gamma_x \gamma_y}{2} \right) \qquad g_{ez1} = \varepsilon_r \gamma_x \gamma_y \tag{5.52}$$

$$r_{mx0} = 2 v_r^2 \frac{(\rho_y - \rho_x)}{2 + \rho_x} \qquad r_{mx1} = 4 \rho_x v_r^2 \frac{(\rho_y - \rho_x)}{(2 + \rho_x)} \tag{5.53}$$

$$r_{my0} = 2 v_r^2 \frac{(\rho_x - \rho_y)}{2 + \rho_y} \qquad r_{my1} = 4 \rho_y v_r^2 \frac{(\rho_x - \rho_y)}{(2 + \rho_y)} \tag{5.54}$$

By substituting in equation 5.38, one can obtain the field calculation steps

for freespace ($\chi_e = 0$)as,

$$V_z = \frac{2V_z^i - z^{-1}S_{ez}}{4 + g_{ez0}} \qquad S_{ez} = g_{ez1}V_z + z^{-1}S_{ez} \tag{5.55}$$

$$i_x = \frac{2i_x^i + z^{-1}S_{mx}}{2 + \frac{Z_L}{Z_{TL}} + r_{mx0}} \qquad S_{mx} = \frac{r_{mx1}i_x + (2-\rho_x)S_{mx}}{2+\rho_x} \tag{5.56}$$

$$i_y = \frac{2i_y^i + z^{-1}S_{my}}{2 + \frac{Z_L}{Z_{TL}} + r_{my0}} \qquad S_{my} = \frac{r_{my1}i_y + (2-\rho_y)S_{my}}{2+\rho_y} \tag{5.57}$$

$$\tag{5.58}$$

where $V_z^i = V_1^i + V_2^i + V_3^i + V_4^i$, $i_x^i = -(V_3^i - V_4^i - V_{Lx}^i)$ and $i_y^i = -(V_1^i - V_2^i - V_{Ly}^i)$. In the case of a material with constant electrical susceptibility χ_e equation 5.55 is changed to

$$V_z = \frac{2V_z^i + z^{-1}(S_{\chi ez} - S_{ez})}{4 + g_{ez0} + 4\chi_e} \tag{5.59}$$

where $S_{\chi ez} = 8\chi_e V_z - z^{-1}S_{\chi ez}$.

Instability of UPML in TLM

In this study, a value of $\sqrt{2}$ was used for the scaling factor v_r. This also identical to a 3D TLM mesh reduced to a 2D mesh with periodic boundary conditions at z-plane boundaries. Further, PMLs in TLM are terminated with a TLM matched boundary in this study unless noted otherwise. The UPML model became universally unstable due to the negative conductivity present as mentioned in the beginning of this sub-section.

It was noted that when the excitation was higher in frequency compared to $f = c/\Delta l$, longer time was taken to gain instability. When the conductivity is decreased, again the method took longer time to gain instability. But the reflection at the boundary was well below -100dB until it became unstable. Even though this method is not further studied, it is suggested that this method could provide significant improvement in TLM if the source of instability could be found. Instead convolutional PML(CPML), which has a similar equations but relates back to the split field formulation [17] was

studied next.

5.4 Convolutional PML Formulation

Convolution PML is an alternative method derived to obtain a perfect matching interface between two material mediums, one of which is intended to be absorbing [20] to form the perfect matched layer. Considering plane wave propagation in a material, coordinate stretching was proposed by Chew and Weedon [20] so that wave absorbing is achieved by coordinate transformation rather than changing material properties.

Maxwell's equations in the new coordinates is defined as [20],

$$\nabla_e \times \mathbf{E} = j\omega\mu\mathbf{H} \tag{5.60}$$

$$\nabla_h \times \mathbf{H} = -j\omega\varepsilon\mathbf{E} \tag{5.61}$$

$$\tag{5.62}$$

where,

$$\nabla_e = \hat{\mathbf{x}}\frac{1}{e_x}\frac{\partial}{\partial x} + \hat{\mathbf{y}}\frac{1}{e_y}\frac{\partial}{\partial y} + \hat{\mathbf{z}}\frac{1}{e_z}\frac{\partial}{\partial z} \tag{5.63}$$

$$\nabla_h = \hat{\mathbf{x}}\frac{1}{h_x}\frac{\partial}{\partial x} + \hat{\mathbf{y}}\frac{1}{h_y}\frac{\partial}{\partial y} + \hat{\mathbf{z}}\frac{1}{h_z}\frac{\partial}{\partial z} \tag{5.64}$$

A plane wave propagates undisturbed by a coordinate transformation (i.e. the wave impedance at the boundary is constant at $\sqrt{\mu/\varepsilon}$) if $e_x = h_x$, $e_y = h_y$, and $e_z = h_z$ irrespective of the values of $e_i, i = x, y, z$ [20].

Let $e_i = h_i = s_i, i = x, y, z$. Then in two dimensions and in frequency domain for E-waves, component wise Maxwell's equations can be written as,

$$\begin{bmatrix} \frac{1}{s_x}\frac{\partial H_y}{\partial x} - \frac{1}{s_y}\frac{\partial H_x}{\partial y} \\ -\frac{1}{s_y}\frac{\partial E_z}{\partial y} \\ \frac{1}{s_x}\frac{\partial E_z}{\partial x} \end{bmatrix} = \begin{bmatrix} j\omega\varepsilon E_z \\ j\omega\mu H_x \\ j\omega\mu H_y \end{bmatrix} \tag{5.65}$$

where $s_x = 1 + \frac{\sigma_x(x)}{j\omega\varepsilon_0}$ and $s_y = 1 + \frac{\sigma_y(y)}{j\omega\varepsilon_0}$.

The equation can be rearranged as after substituting for s_x, s_y,

$$\begin{bmatrix} \left(1+\frac{\sigma_y}{j\omega\varepsilon_0}\right)\frac{\partial H_y}{\partial x} - \left(1+\frac{\sigma_x}{j\omega\varepsilon_0}\right)\frac{\partial H_x}{\partial y} \\ -\frac{\partial E_z}{\partial y} \\ \frac{\partial E_z}{\partial x} \end{bmatrix} = \begin{bmatrix} j\omega\varepsilon_0 E_z \\ j\omega\mu_0 H_x \\ j\omega\mu_0 H_y \end{bmatrix} + \begin{bmatrix} \varepsilon_r\left(\sigma_x + \sigma_y + \frac{\sigma_x\sigma_y}{j\omega\varepsilon_0}\right)E_z \\ \sigma_y\eta_0^2 H_x \\ \sigma_x\eta_0^2 H_y \end{bmatrix} + \begin{bmatrix} j\omega\varepsilon_0\chi_e E_z \\ 0 \\ 0 \end{bmatrix} \tag{5.66}$$

After normalisations for 2D, one obtains,

$$2\begin{bmatrix} \left(1+\frac{\gamma_y}{2\bar{s}}\right)(V_1+V_2) + \left(1+\frac{\gamma_x}{2\bar{s}}\right)(V_3+V_4) \\ -(V_3-V_4) \\ -(V_1-V_2) \end{bmatrix}^i = \begin{bmatrix} (4+g_{ez}(\bar{s})+2\bar{s}\chi_e)V_z \\ (2+r_{mx})i_x \\ (2+r_{my})i_y \end{bmatrix} \tag{5.67}$$

where

$$g_{ez}(\bar{s}) = \varepsilon_r\left(\gamma_x + \gamma_y + \frac{\gamma_x\gamma_y}{2\bar{s}}\right) \tag{5.68}$$

$$r_{mx}(\bar{s}) = \rho_y \tag{5.69}$$

$$r_{my}(\bar{s}) = \rho_x \tag{5.70}$$

$$\gamma_i = \sigma_i \Delta l \eta_0 \sqrt{2} \quad , i = x, y \tag{5.71}$$

The current update equations are given by the standard equation for 2D TLM. The voltage update equation can be obtained by using the z-transform.

$$V_z = \frac{\left(1+\frac{\gamma_y}{4}\right)2V_{zx}^i + \left(1+\frac{\gamma_x}{4}\right)2V_{zy}^i + z^{-1}(S_{\chi ez} + S_{ez})}{4 + g_{ez0} + 4\chi_e} \tag{5.72}$$

where $V_{zx} = V_1 + V_2$,
$V_{zy} = V_3 + V_4$,
$S_{ez} = \gamma_y V_{zx}^i + \gamma_x V_{zy}^i - g_{ez1}V_z + z^{-1}S_{ez}$

5.4.1 Implementation

Convolutional PML method, when implemented as formulated becomes unstable for a 2D mesh. It was found out that the integrating term on the L.H.S (i.e. the convolutional term) is causing the instability. However, this term is also the key in obtaining the perfect matching condition. In order to retain the amplification while eliminating the integrating term, S_{ez} was modified to contain terms from the R.H.S of the equation. Therefore, $S_{ez} = -g_{ez1}V_z + z^{-1}S_{ez}$. This stabilised the material, but some reflection was also observed..

In order to characterise the PML medium, the reflection at the end of a metal waveguide is used in the next section.

5.4.2 Reflection

The reflection at the end of the metal waveguide presented in section 3.1.1 was truncated with 25 CPML layers. In FDTD a similar structure in microwave frequencies and millimetre length space steps, a reflection between $-90dB$ to $-110dB$ was observed [4]. By using a constant conductivity profile and with different conductivity values given by the required attenuation $R_C = 5dB, 10dB, 15dB, 20dB$ was used as the PML. For a Gaussian pulse excitation at $225THz$ with a pulse width of $10fs$, the reflection observed is shown in figure 5.12.

According to figure 5.12, the best reflection properties were obtained when $R_C = 10dB$ for 25 CPML layers. When required attenuation R_C is smaller, the initial reflection from the freespace-CPML boundary is smaller but the wave is not attenuated enough, resulting in a higher reflection. When R_C is larger, the initial reflection from the freespace-CPML boundary is higher producing a higher overall reflection. Thus, from 25 layers, with required attenuation $R_C = 10dB$ an overall reflection of $-35dB$ was observed throughout the frequency spectrum. Even with other values of R_C, a reflection of $-30dB$ could be obtained. This is an achievement compared to the TLM matched boundary, but is not as good as the reflection characteristics observed for

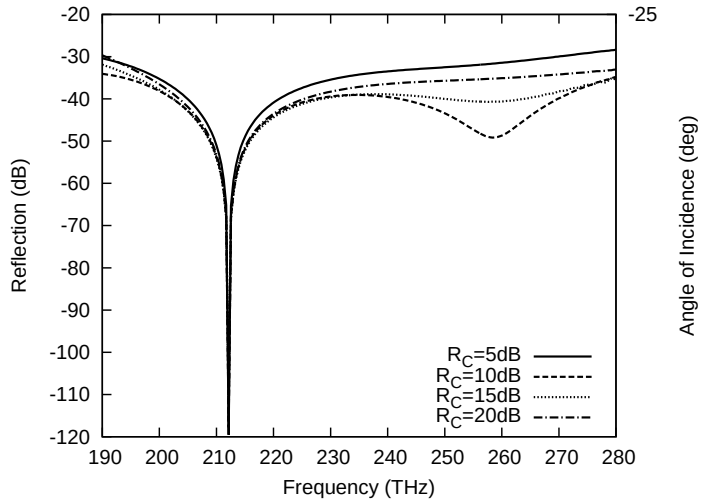

Figure 5.12: The reflection at the end of metal waveguide of width $1\mu m$ truncated by 25 CPML layers of constant conductivity profile with $R_C = 5dB$ (solid), $R_C = 10dB$ (dashed), $R_C = 15dB$ (dotted), $R_C = 20dB$ (dot-dash).

other PML formulations in TLM [4], [5].

Then, the reflection obtained by different conductivity profiles were considered. In figure 5.13, the metal waveguide reflection for 25 CPML layers of a constant, linearly increasing, quadratically increasing, and logarithmically increasing profiles with a required attenuation $R_C = 10dB$, are shown.

According to figure 5.13, the logarithmic profile produced better reflection of $-40dB$ than that obtained from the constant profile. The quadratic profile provided the worst reflection. This is contradictory to the observations by Pena and Ney [4], where quadratic profile had given the best reflection properties.

Then the number of CPML layers were doubled to observe how well CPML can be used to absorb incident waves. If the reflection is significantly smaller for a longer CPML layer then it can be used to truncate boundaries though not efficient as other PML formulations. In figure 5.14, the reflection at the metal waveguide was observed for a CPML of 50 layers with a logarithmic conductivity profile and the required attenuation of $R_C = 10dB, 15dB, 20dB$.

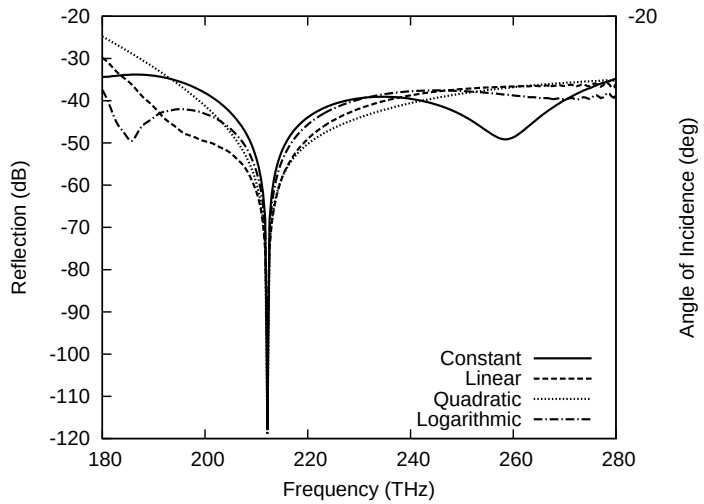

Figure 5.13: The reflection at the end of metal waveguide of width $1\mu m$ truncated by 25 CPML layers of constant (solid), linear (dashed), quadratic (dotted) and logarithmic (dot-dash) conductivity profiles with $R_C = 10dB$.

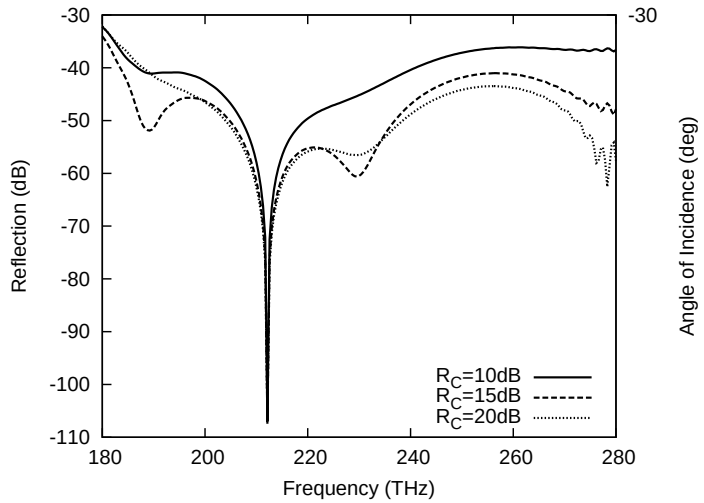

Figure 5.14: The reflection at the end of metal waveguide of width $1\mu m$ truncated by 50 CPML layers of logarithmic conductivity profile with $R_C = 10dB$ (solid), $R_C = 15dB$ (dashed), $R_C = 20dB$ (dotted).

The reflection has slightly improved upto $-45dB$ by using 50 CPML layers when $R_C = 15dB$. The reflection for $R_C = 10dB$ and $R_C = 20dB$ are both larger than that obtained for $R_C = 15dB$. This is evident that doubling of CPML layers does not decrease the reflection by a significant amount. This indicates that the CPML is not an effective method to truncate boundaries. This is because PML materials require several extra variable in computer code resulting in significant increase in omputation time if large number of layers are to be used to obtained the required reflection.

5.5 Conclusions

In the last chapter an accurate discretisation technqiue was presented for optical resonators. The main aim of this chapter was to find better simulation domain tructation methods, so that resonators can be externally excited.

To this end PML formulations by Berenger were implemented, but proved very inefficient when the angle of incidence is larger than 45°. A uniaxial PML formulation was implemented next. This formulation was unstable despite trying to satisfy Courant condition by slowing down the TLM mesh. Convolutional PML formulation was considered and was also unstable. By ignoring some delay terms, the convolutional PML became stable, and reflection at a metal waveguide was then observed. The results have shown that a logarithmic profile could obtain better reflections with CPML at about $-35dB$ for 25 layers, $-45dB$ for 50 layers. It was noted that significantly increasing the number of layers does not result in a significant attenuation of the reflected waves. This indicates that the CPML formulation is also inefficient.

As a future direction it is suggested to investigate the stability issues of UPML, where good attenuation could be observed before going into an unstable state. CPML can be used until such a time. In order to model chalcogenide microresonators dispersion and nonlinearity should be modelled in TLM. Hence, the next chapter aims at modelling dipersion characteristics of

several chalcogenide materials.

References

[1] R. Collin, *Field theory of guided waves*, vol. 2. IEEE press New York, 1991.

[2] S. Kirkup and S. Amini, "Solution of the helmholtz eigenvalue problem via the boundary element method," *International journal for numerical methods in engineering*, vol. 36, no. 2, pp. 321–330, 1993.

[3] J. Bérenger, *Perfectly Matched Layer (PML) for Computational Electromagnetics*. Synthesis Lectures on Computational Electromagnetics, Morgan & Claypool Publishers, 2007.

[4] N. Peña and M. Ney, "A new TLM node for Berenger's perfectly matched layer," *Microwave and Guided Wave Letters, IEEE*, vol. 6, pp. 410 –412, Nov 1996.

[5] J. Dubard and D. Pompei, "Optimization of the PML efficiency in 3-d TLM method," *Microwave Theory and Techniques, IEEE Transactions on*, vol. 48, no. 7, pp. 1081–1088, 2000.

[6] J. Paul, *Modelling of General Electromagnetic Material Properties in TLM*. PhD thesis, The University of Nottingham, 1998.

[7] J. Paul, C. Christopoulos, and D. Thomas, "Perfectly matched layer for transmission line modelling (TLM) method," *Electronics Letters*, vol. 33, no. 9, pp. 729–730, 1997.

[8] C. Christopoulos, *The transmission-line modeling method: TLM*. Institute of Electrical and Electronics Engineers, 1995.

[9] A. V. Boriskin, S. V. Boriskina, A. Rolland, R. Sauleau, and A. I. Nosich, "Test of the FDTD accuracy in the analysis of the scattering resonances

associated with high-Q whispering-gallery modes of a circular cylinder," *J. Opt. Soc. Am. A*, vol. 25, pp. 1169–1173, May 2008.

[10] J. Berenger, "A perfectly matched layer for the absorption of electromagnetic waves," *Journal of computational physics*, vol. 114, no. 2, pp. 185–200, 1994.

[11] J. Berenger, "Three-dimensional perfectly matched layer for the absorption of electromagnetic waves," *Journal of computational physics*, vol. 127, no. 2, pp. 363–379, 1996.

[12] C. Li, C. Liu, and S. Chen, "Optimization of a PML absorber's conductivity profile using FDTD," *Microwave and Optical Technology Letters*, vol. 37, no. 5, pp. 380–383, 2003.

[13] C. Eswarappa and W. Hoefer, "Implementation of Berenger absorbing boundary conditions in TLM by interfacing FDTD perfectly matched layers," *Electronics Letters*, vol. 31, no. 15, pp. 1264–1266, 1995.

[14] N. Pena and M. M. Ney, "Absorbing-boundary conditions using perfectly matched-layer (PML) technique for three-dimensional TLM simulations," *Microwave Theory and Techniques, IEEE Transactions on*, vol. 45, pp. 1749–1755, Oct 1997.

[15] S. Le Maguer and M. M. Ney, "Extended PML-TLM node: an efficient approach for full-wave analysis of open structures," *International Journal of Numerical Modelling: Electronic Networks, Devices and Fields*, vol. 14, no. 2, pp. 129–144, 2001.

[16] S. Gedney, "An anisotropic perfectly matched layer-absorbing medium for the truncation of FDTD lattices," *Antennas and Propagation, IEEE Transactions on*, vol. 44, no. 12, pp. 1630–1639, 1996.

[17] J. Roden and S. Gedney, "Convolutional PML (CPML): An efficient FDTD implementation of the CFS-PML for arbitrary media," *Microwave and optical technology letters*, vol. 27, no. 5, pp. 334–338, 2000.

[18] M. Krumpholz and P. Russer, "On the dispersion in tlm and fdtd," *Microwave Theory and Techniques, IEEE Transactions on*, vol. 42, no. 7, pp. 1275–1279, 1994.

[19] V. Trenkic, C. Christopoulos, and T. Benson, "Generally graded TLM mesh using the symmetrical supercondensed node," *Electronics Letters*, vol. 30, no. 10, pp. 795–797, 1994.

[20] W. Chew and W. Weedon, "A 3D perfectly matched medium from modified Maxwell's equations with stretched coordinates," *Microwave and optical technology letters*, vol. 7, no. 13, pp. 599–604, 2007.

6

Dispersive Models for Chalcogenide Glasses

The microresonators and waveguides considered so far have a myriad of applications in optical devices. Many of the devices studied experimentally to date are based in silica glass, especially when it comes to microresonators. Silica being an amorphous glass material has been widely used due to its morphability into spheres by thermal reflux [1]. However, the refractive index and nonlinearities are low in silica glasses compared to other semiconductor materials. Chalcogenide glass materials are inherently superior to silica for microresonator applications because of their higher index of refraction and nonlinearities compared to silica [2]. However, their physical characteristics and chemical reactions with atmospheric elements make them delicate and prone to contamination.

The refractive index and nonlinearities of chalcogenide glasses also vary with frequency (wavelength) [3]. This leads to dispersion (pulse broadening) in optical systems because the phase velocity at each frequency becomes different within the material. Pulse broadening also occurs due to the guiding structure [4]. Sometimes dispersion acts to advantage, such as when balancing pulse spreading with nonlinearity to form solitons [5]. Whether dispersion

is desired or undesired applications require accurate knowledge of dispersion, as well as nonlinearities, in materials as a first step to understanding how pulses propagate through waveguide structures made using them.

In this chapter, refractive index and dispersion models are presented for some chalcogenide glass materials. The same models are then implemented in TLM z-models. These models are then validated in the context of plane wave reflection.

6.1 Refractive Index Models

6.1.1 Complex Refractive Index and Permittivity

The permittivity of a material can generally be complex i.e. $\varepsilon = \varepsilon_1 + j\varepsilon_2$. The refractive index $n + j\kappa$ and the electrical susceptibility $\chi_e = \chi_{e1} + j\chi_{e2}$ are also complex valued. The relationship between the complex permittivity, susceptibility and the complex refractive index are,

$$\varepsilon_1 = \chi_{e1} + 1 = n^2 - \kappa^2 \qquad \varepsilon_2 = \chi_{e2} = 2n\kappa \tag{6.1}$$

where n is the real part of refractive index and κ is the extinction coefficient (imaginary part of refractive index).

Maxwell's curl equations for nonmagnetic materials can be expressed in the form [6],

$$\begin{aligned} \nabla \times \mathbf{H} &= -j\omega\varepsilon_0\mathbf{E} - j\omega\chi_e\mathbf{P} \\ \nabla \times \mathbf{E} &= j\omega\mu_0\mathbf{H} \end{aligned} \tag{6.2}$$

where $\mathbf{P}$ is the electrical polarisation vector and a time variation of $e^{-j\omega t}$ has been assumed. The real part of the susceptibility (χ_e) in equation 6.2, results in refraction while the imaginary part results in absorption. The real part and the imaginary parts of the susceptibility are not independent of each other

and are related by the Kramer's Kronig relation given by [7],

$$\chi_{e1}(\omega) = \frac{2}{\pi}\wp\int_0^\infty \frac{\xi\chi_{e2}(\xi)}{\xi^2-\omega^2}d\xi \qquad \chi_{e2}(\omega) = -\frac{2\omega}{\pi}\wp\int_0^\infty \frac{\chi_{e1}(\xi)}{\xi^2-\omega^2}d\xi \tag{6.3}$$

where ξ is the angular frequency and the integration variable, $\wp$ denotes the Cauchy principal part [7]. Hence, once the real or imaginary part is known the other can be obtained. From these relations it is evident that refraction is linked with absorption/transparency and that the Maxwell's equations given above model both refractive index and absorption simultaneously.

Further, in a general complex permittivity model [7], the conductance σ_e is given by,

$$\sigma_e(\omega) = \varepsilon_0\omega\varepsilon_2(\omega) \tag{6.4}$$

There exists many models for refractive index. Most methods model only the real part of the refractive index, such as the Cauchy model and Sellmeier model [7]. On the other hand models such as Drude model [7], and the Tauc-lorentz model [8] describe both real and the imaginary part of the refractive index. Most materials are modelled using Drude and Sellmeir equations [4, 7] and these coefficients are well documented [9].

6.1.2 Cauchy Model

The Cauchy dispersion models is the most simplified and the very first model developed. However, the Cauchy model approximation is only valid away from band gaps, where the imaginary part of refractive index is very small. In other words, the model is valid in the optically transparent regions. The Cauchy model defines the real part of permittivity (ε_1) as,

$$\chi_{e1} = A + \frac{B}{\lambda^2} + \frac{C}{\lambda^4} \tag{6.5}$$

where A, B, C are the model parameters and λ is the wavelength [7, 9].

The model according to the equation 6.5, assumes that the band gap, where a resonance in refractive index occurs is at zero frequency. Hence, the Cauchy

model is not appropriate if multiple bandgaps fall within or close to the frequency range of interest.

6.1.3 Sellmeier Model

The Sellmeier model is the most widely used and documented model as it models the refractive index to a high degree of accuracy. Similar to the Cauchy model, the Sellmeier model is valid away from band gaps. But unlike the Cauchy method, the Sellmeier model can be used to model materials with more than one band gap in the frequency range of interest. The Sellmeier model of real electrical susceptibility (χ_e) is given by,

$$\chi_e = A_0 + \sum_{j=1}^{N_s} \frac{A_j \lambda^2}{\lambda^2 - a_j^2} \tag{6.6}$$

where A_j, a_j are model parameters, and N_s is the number of Sellmeier coefficients.

The equation 6.6 models multiple infinite material resonances at a_j wavelengths. According to [10], two Sellmeier terms (N_s=2), one in the ultraviolet (UV) and other in the infrared (IR) are sufficient for most solid materials for a wade frequency range away from absorption peaks.

6.1.4 Drude Model

The Drude model is built on the basis of electron hole transitions within a material. By considering the movement of an electron in the presence of an external electric field, and the resultant polarisation, the Drude model of complex permittivity can be obtained as [7].

$$\chi_e(\omega) = \chi_{e\infty} + \frac{A\omega_0^2}{\omega_0^2 + j\gamma\omega - \omega^2} \tag{6.7}$$

where ω_0 is the frequency of absorption peak, γ is the damping of an absorption peak, defining its width, and A is the strength of the absorption peak.

Hence the real part and the imaginary parts of the model are,

$$\chi_{e1}(\omega) = \chi_{e\infty} + \frac{A\omega_0^2(\omega^2 - \omega_0^2)}{(\omega^2 - \omega_0^2)^2 + \gamma^2\omega^2} \qquad \chi_{e2}(\omega) = \frac{A\omega_0^2\gamma\omega}{(\omega^2 - \omega_0^2)^2 + \gamma^2\omega^2} \tag{6.8}$$

In metals, electrons can move freely in the conduction band; hence, the ω_0 term in the denominator vanishes producing,

$$\chi_e(\omega) = \chi_{e\infty} - \frac{A\omega_p^2}{\omega^2 + j\gamma\omega} \tag{6.9}$$

where ω_p is the plasma frequency [7].

6.1.5 Tauc-Lorentz Model

The Tauc-Lorentz model describes the imaginary part of the permittivity. It is mostly used for amorphous materials. It is reported to be very accurate compared to other refractive index models [8, 11]. It takes the form

$$\varepsilon_2(E) = \frac{AE_0C(E - E_g)^2}{(E^2 - E_0^2)^2 + C^2E^2}\frac{1}{E} \tag{6.10}$$

where A, E_0, C, E_g are model parameters and, along with $E = hc/\lambda$, all parameters have units of energy in eV.

From the Kramer's Kronig rule, the real part of permittivity can be obtained as follows [8, 11].

$$\varepsilon(E) = \varepsilon_1(\infty) + \frac{A_1E^2 + A_2 + A_3/E\{(E + E_g)^2\ln(E + E_g)^2 - (E - E_g)^2\ln(E - E_g)^2\}}{E^4 + E^2(C^2 - 2E_0^2) + E_0^4} \tag{6.11}$$

where,

$$A_1 = a_{ln}(E_g^2 - E_0^2) - a_{tan}(E_0^2 + E_g^2) + a_{tan2} \tag{6.12}$$

$$A_2 = a_{ln}(E_g^2 C^2 - E_0^4 - 3E_0^2 E_g^2) - a_{tan}(E_g^2 C^2 - E_g^2 E_0^2 - E_0^4) - a_{tan2}\gamma^2 - a_{ln2} \tag{6.13}$$

$$A_3 = \frac{AE_0 C}{2\pi} \tag{6.14}$$

$$a_{ln} = \frac{AC}{2\pi\alpha E_0} \ln\left(\frac{E_0^2 + E_g^2 + \alpha E_g}{E_0^2 + E_g^2 - \alpha E_g}\right) \tag{6.15}$$

$$a_{ln2} = 2\frac{AE_0 C}{2\pi} E_g \ln((E_0^2 - E_g^2)^2 + E_g^2 C^2) \tag{6.16}$$

$$a_{tan} = \frac{A}{\pi E_0}\left[\pi - \tan^{-1}\left(\frac{2E_g + \alpha}{C}\right) + \tan^{-1}\left(\frac{-2E_g + \alpha}{C}\right)\right] \tag{6.17}$$

$$a_{tan2} = 2\frac{AE_0 E_g}{\pi\alpha}\left[\pi + 2\tan^{-1}\left(2\frac{\gamma^2 - E_g^2}{\alpha C}\right)\right] \tag{6.18}$$

$$\alpha = \sqrt{4E_0^2 - C^2} \tag{6.19}$$

$$\gamma = \sqrt{E_0^2 - C^2/2} \tag{6.20}$$

Since, the Tauc-Lorentz model fits to the imaginary part of the refractive index(or permittivity), it is a model of absorption peaks.

6.2 Refractive Index Model for Chalcogenide Glasses

All the models presented in this chapter are rational functions except for the Cauchy model. Therefore, fitting these models to experimental data is sensitive to initial guess values. Further details regarding each model is given below.

For the Cauchy and the Sellmeier models, the fitting to experiment data for chalcogenide glasses was performed only for values where $\kappa \approx 0$. Otherwise, refractive index near the absorption peak affects the fitting accuracy for longer

wavelengths. Since the Cauchy model is a polynomial, least square fitting methods produce stable model parameters.

Sellmeier models have singularities at $a_1, a_2, \ldots$. This requires, the initial parameters of $a_1, a_2, \ldots$ to have values not within the fitting wavelength range(i.e. wavelengths for which $\kappa = 0$). If otherwise, this causes the matrices of the least square fitting method to be singular as well. Hence, values less than the material resonance are used as initial values for $a_1, a_2, \ldots$ According to [10], two Sellmeier terms (a_1 in UV and a_2 in IR) with a constant term is sufficient for most solid materials for a wide frequency range away from the absorption peaks. In order to verify this for chalcogenide glasses, Sellmeier I and Sellmeier II (one and two terms in the summation presented in equation 6.6) models were used with the constant term.

In this study refractive index and absorption data of three Chalcogenide glass materials formed in-house are used to obtain the dispersion models. Table 6.1 presents the fitting parameters obtained for each refractive index model. The raw refractive index and extinction coefficient data are presented in Z.G.Lian's thesis [12]. The model fittings of Cauchy, Sellmeier models obtained for $As_{40}Se_{60}$, $Ge_{10}As_{24.4}Se_{66.6}$ and $Ge_{17}As_{18}Se_{65}$ are plotted along with their refractive index measurements in figure 6.1 and fittings of Drude and Tauc-Lorentz model of the same glasses along with measurement data in figure 6.2.

For these three Chalcogenide glasses, the Drude model could not be used to model the refractive index for the whole range of refractive index values. The reason for this is that for wavelengths longer than that corresponding to the band gap energy ($approx 700nm$)the absorption reaches near zero. But the Drude model fitted for the whole wavelength range represents significant absorption even below band gap energy (i.e. at longer wavelengths), due to its slowly decaying Lorentzian shape. However, the Drude model can be fitted for wavelengths longer than $700nm$, in which case the absorption becomes small (i.e. $\gamma << \omega_0$) effectively coinciding with the Sellmeier I model.

The Tauc-Lorentz and the Drude models also represent the imaginary parts of the refractive index (κ). The modelled imaginary parts of refractive index

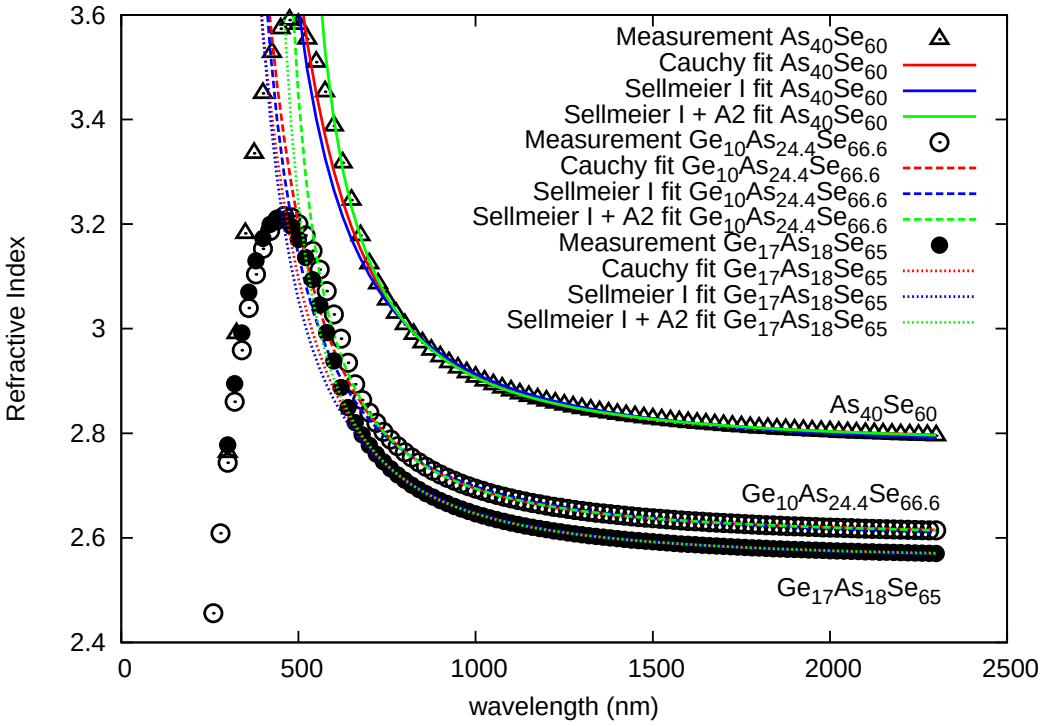

Figure 6.1: Cauchy (red), Sellmeier I (blue), Sellmeier I with Constant (green) fits to $As_{40}Se_{60}$ (solid), $Ge_{10}As_{24.4}Se_{66.6}$ (dashed), $Ge_{17}As_{18}Se_{65}$ (dotted) along with refractive index measurement data for the three glasses.

via the real part of the refractive index fits are presented in figure 6.3 along with the measured extinction coefficient κ.

According to figures 6.1 and 6.2, the Tauc-Lorentz (TL) fits best to the measurements within the whole wavelength range. Tauc-Lorentz model is known to accurately model semiconductor materials near band gaps [13, 14] and Chalcogenide glasses [15, 16]. The fact that the model corresponds to the physics of the amorphous material means that the TL coefficients are related to the material composition. This lets one design materials to satisfy refractive index (permittivity) criteria as pointed out in [15].

For wavelengths longer than $800nm$ all fittings model the refractive index close to the measured values. Sellmeier I model with a constant and the

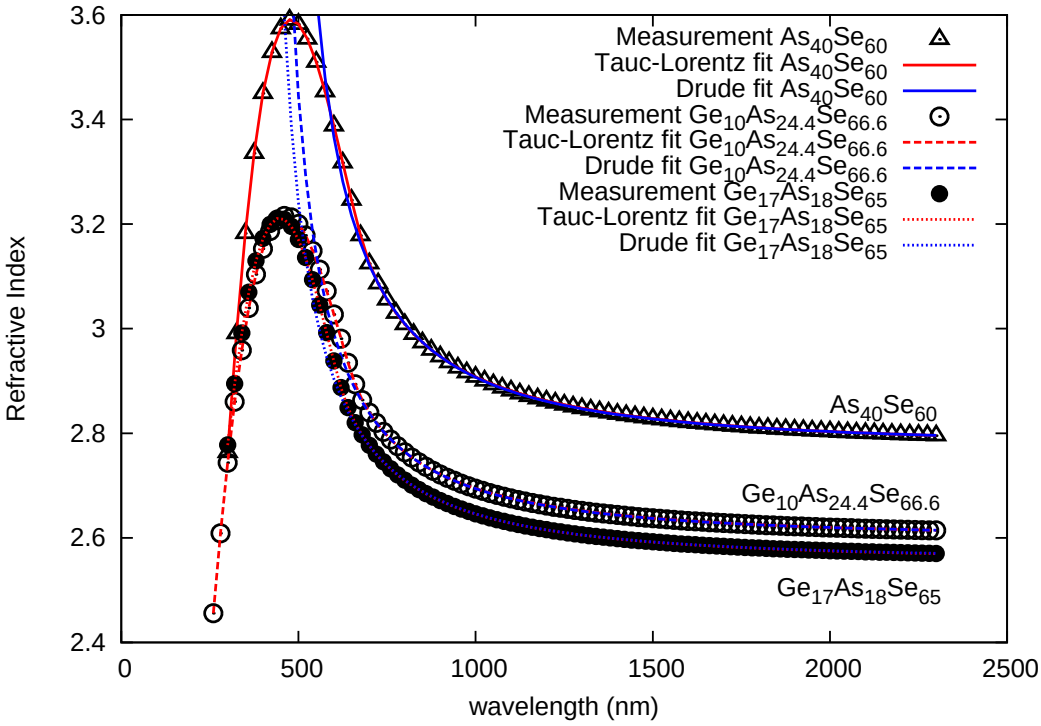

Figure 6.2: Drude (blue), Tauc-Lorentz (red) fits to $As_{40}Se_{60}$ (solid), $Ge_{10}As_{24.4}Se_{66.6}$ (dashed), $Ge_{17}As_{18}Se_{65}$ (dotted) along with refractive index measurement data for the three glasses.

Drude model more accurately model the refractive index up to $600nm$ than Cauchy and Sellmeier I model.

The Extinction coefficient is also well modelled by Tauc-Lorentz as shown in figure 6.3. The Drude model indicates the presence of a resonance peak, but the peak is not positioned or damped appropriately. Therefore, Drude model does not provide much of an advancement over Sellmeier models though it represents some form of absorption.

Since this study concentrates on modelling chalcogenide materials in electromagnetic simulations, it will be useful to identify fitting errors at this stage so that they can be compared with TLM modelling errors later. The percentage error in modelled refractive index for the three glasses for Cauchy and Sellmeier I models are presented in figure 6.4, whereas percentage error

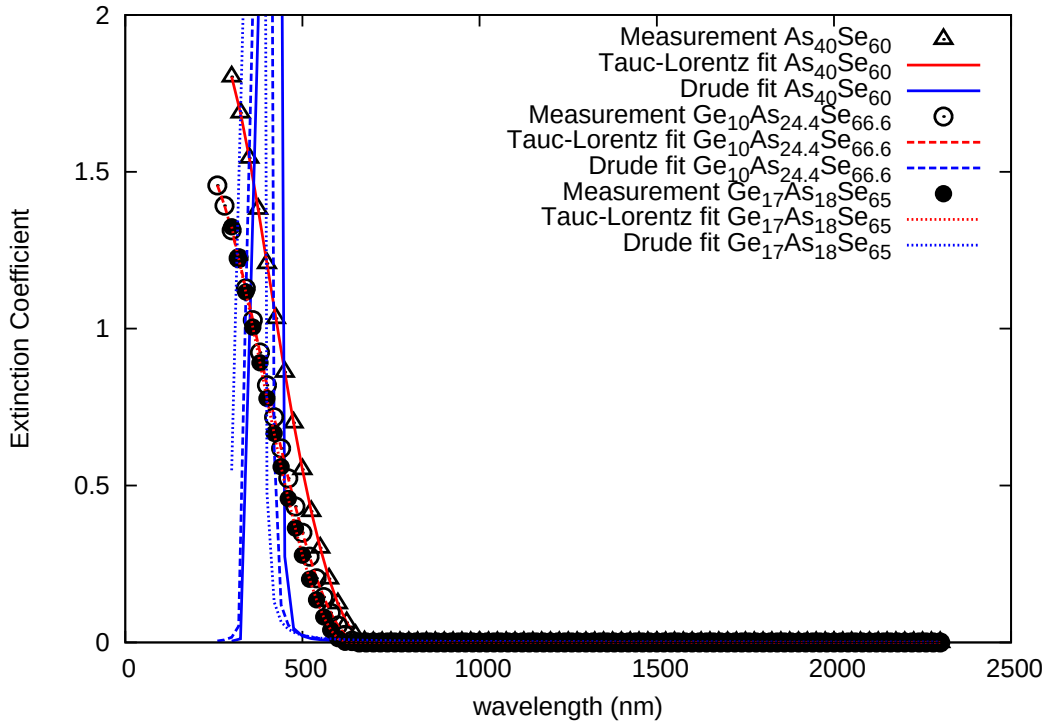

Figure 6.3: Extinction coefficient represented by Drude (blue), Tauc-Lorentz (red) model fits to $As_{40}Se_{60}$ (solid), $Ge_{10}As_{24.4}Se_{66.6}$ (dashed), $Ge_{17}As_{18}Se_{65}$ (dotted) along with extinction coefficient measurement data for the three glasses.

of Sellmeier I + constant, Drude and Tauc-Lorentz models are presented in figure 6.5.

As seen in figure 6.5, the Tauc Lorentz model's error is uniform over the interested frequency range at around 0.02-0.05%. The errors of all other models increase drastically for wavelengths below about $700nm$, mainly due to non zero κ (i.e. close to the absorption peak). The error of the Sellmeier I and Cauchy models are larger than that of others at 0.3% away from absorption peaks. The Sellmeier I with a constant and Drude models have an error close to the Tauc-Lorentz model away from absorption peaks.

Since addition of a constant rarely increases implementation complexities in general, from now on the Sellmeier I model with a constant is referred to as

Table 6.1: Cauchy, Sellmeier and Tauc Lorentz fitting to $Ge10As_{24.4}Se_{66.6}$ Cauchy, Sellmeier and Tauc Lorentz fitting to $Ge17As_{18}Se_{65}$ Cauchy, Sellmeier I, Sellmeier I + Constant, Drude, Tauc-Lorentz parameters for three Chalcogenide glasses $As_{40}Se_{60}$, $Ge_{10}As_{24.4}Se_{66.6}$,$Ge_{17}As_{18}Se_{65}$.

Model			$As_{40}Se_{60}$	$Ge_{10}As_{24.4}Se_{66.6}$	$Ge_{17}As_{18}Se_{65}$
Cauchy	A		6.7196	5.7642	5.5360
($> 700nm$)	B	$(\mu m)^2$	0.5045	0.3696	0.3674
	C	$(\mu m)^4$	0.2303	0.1252	0.09886
Sellmeier I	A_1		6.6482	5.7234	5.5065
($> 700nm$)	a_1	μm	0.3351	0.2976	0.2912
Sellmeier I	A_1		2.8748	2.4957	2.7056
+ Constant	a_1	μm	0.4542	0.4098	0.3856
($> 700nm$)	A_0		3.8275	3.2583	2.8232
Drude	A		3.1450	2.4887	2.7002
($> 700nm$)	γ	rad/ps	14.162	39.228	57.069
	ω_0	rad/ps	4290.1	4595.4	4884.5
	$\chi_e(\infty)$		3.5536	3.2654	2.8287
Tauc Lorentz	A		209.7	208.7	237.2
	C		4.509	6.773	6.579
	E_0		3.180	3.388	3.290
	E_g		1.804	1.881	1.986
	$\varepsilon_1(\infty)$		1.048	1.238	0.9566

the Sellmeier I model in this study. Further, when a Sellmeier II term model is used for these three glasses, the second resonance occurs at very small wavelength $< 0.01\mu m$, effectively representing a Sellmeier I model with a constant. The Sellmeier III model was not studied in detail as its convergence was found to depend mostly on the initial values indicating that the model has more free parameters than the experimental data.

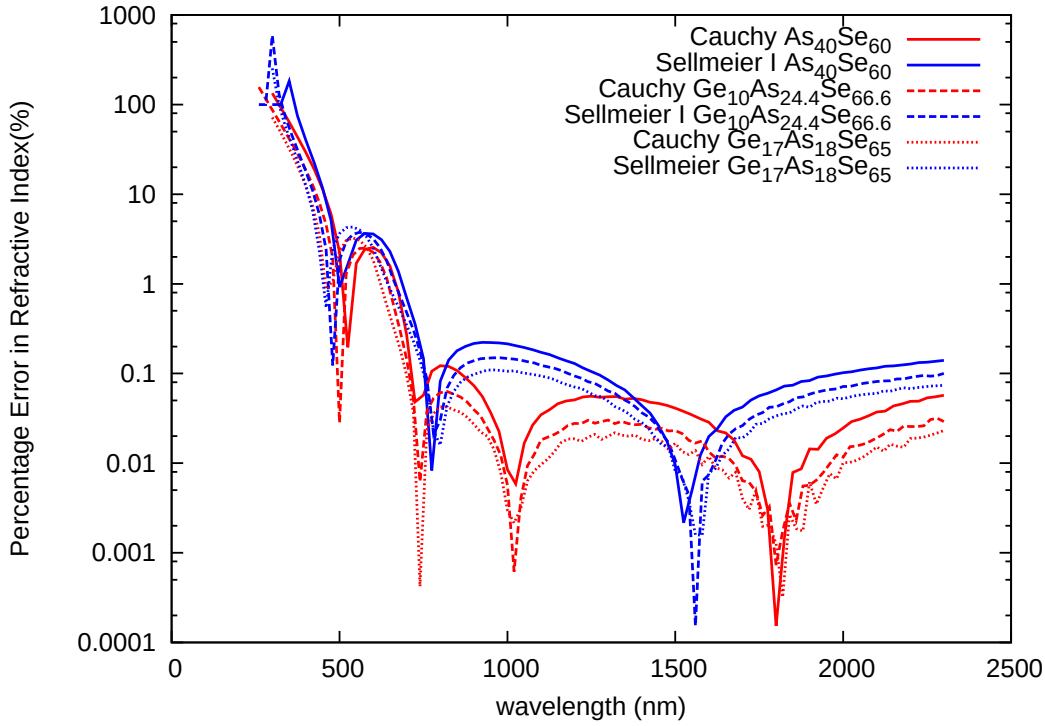

Figure 6.4: Percentage error of refractive index of Cauchy (red) and Sellmeier I (blue) models relative to the measured refractive indices of $As_{40}Se_{60}$ (solid), $Ge_{10}As_{24.4}Se_{66.6}$ (dashed), $Ge_{17}As_{18}Se_{65}$ (dotted).

6.3 Modelling Dispersion

The dispersion is the dependence of the phase velocity of a wave on frequency. This makes a pulse (collection of frequencies) to broaden or narrow while propagating. The broadening is caused by positive dispersion and occurs due to material dispersion and dispersion of the structure (usually waveguide). Narrowing is caused by negative dispersion (anomalous dispersion) and occurs due to self focusing effects of material nonlinearities and negative dispersive structures. Note that pulse narrowing with dispersive (linear frequency dependant) medium is only possible until the pulse becomes *transform limited pulse*, which is defined as a pulse with the minimum time duration for a given

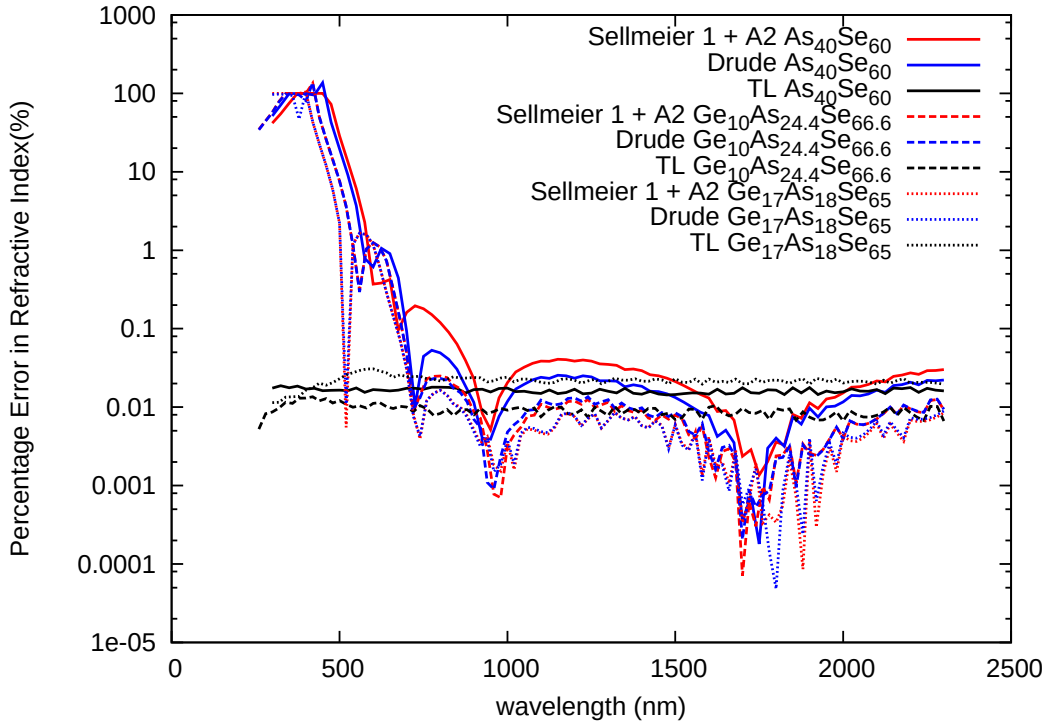

Figure 6.5: Percentage error of refractive index of Sellmeier I + constant (red), Drude (blue), Tauc-Lorentz (black) models relative to the measured refractive indices of $As_{40}Se_{60}$ (solid), $Ge_{10}As_{24.4}Se_{66.6}$ (dashed), $Ge_{17}As_{18}Se_{65}$ (dotted).

spectral content.

The dispersion parameter D is defined by,

$$D = -\frac{2\pi c}{\lambda^2}\frac{\partial^2 k}{\partial \omega^2} \tag{6.21}$$

where c is the speed of light in vacuum and $k = \omega\sqrt{\varepsilon_1}/c$. The same equation can be expressed in terms of ε_1 as,

$$D = -\frac{\lambda}{4c\sqrt{\varepsilon}}\left\{2\frac{\partial^2 \varepsilon_1}{\partial \lambda^2} - \frac{1}{\varepsilon_1}\left(\frac{\partial \varepsilon_1}{\partial \lambda}\right)^2\right\} \tag{6.22}$$

For the Cauchy equation,

$$\frac{\partial \varepsilon_1}{\partial \lambda} = -2\left\{\frac{B}{\lambda^3} + 2\frac{C}{\lambda^5}\right\} \tag{6.23}$$

$$\frac{\partial^2 \varepsilon_1}{\partial \lambda^2} = 2\left\{3\frac{B}{\lambda^4} + 10\frac{C}{\lambda^6}\right\} \tag{6.24}$$

For the Sellmeier I equation,

$$\frac{\partial \varepsilon_1}{\partial \lambda} = -2A_1 a_1^2 \frac{\lambda}{(\lambda^2 - a_1^2)^2} \tag{6.25}$$

$$\frac{\partial^2 \varepsilon_1}{\partial \lambda^2} = 2A_1 a_1^2 \frac{3\lambda^2 + a_1^2}{(\lambda^2 - a_1^2)^3} \tag{6.26}$$

6.4 Transmission Line Models of Dispersion

Dispersion (a frequency dependent refractive index model) can be included in the Maxwell's equation as the Polarisation vector $\mathbf{P} = \chi_e \mathbf{E}$, where χ_e is frequency dependant. This can be achieved in both stub model and the z-domain models [5, 17]. V.Janyani [5] suggests that it is easier to implement dispersion with a z-model than with a stub model once the refractive index model in the s-domain is known. The suggestion is due to the difficulty in determining the combination of electrical components (R,L,C). Janyani [5] has also based this on the Duffing model which includes nonlinearity. Regardless of the implementation path, one must first obtain the s-domain models of the refractive index models presented earlier in order to represent them in TLM.

6.4.1 Laplace Domain Models

Cauchy Model

Let us first consider the Cauchy model. The frequency response of the model in terms of angular frequency ω is,

$$\chi_e(\omega) = A + \frac{B}{(2\pi c)^2}\omega^2 + \frac{C}{(2\pi c)^4}\omega^4 \tag{6.27}$$

It is fairly straight forward to obtain the s-domain model since $s^2 = -\omega^2$ follows from $s = j\omega$. Hence the s-domain sucessptibility of the Cauchy model is,

$$\chi_e(s) = A - \frac{B}{(2\pi c)^2}s^2 + \frac{C}{(2\pi c)^4}s^4 \tag{6.28}$$

Sellmeier Model

Considering the Sellmeier I equation with a constant, the frequency response is,

$$\chi_e(\omega) = A_0 + \frac{A_1}{1 - \left(\frac{a_1}{2\pi c}\right)^2 w^2} \tag{6.29}$$

Even in this instance, the s-domain model can be obtained as,

$$\chi_e(s) = A_0 + \frac{A_1}{1 - \tau_1^2 s^2} \tag{6.30}$$

where $\tau_1 = a_1/2\pi c$.

6.4.2 Z domain Implementations

In order to implement the s-domain models presented above in TLM z domain model, one must use a z-transformation technique. Since direct transformation $s = \frac{1}{T}ln(z)$ cannot be used when the transfer function is a rational function of polynomials of s, one can use bilinear z-transform defined in chapter 2.

Let's consider the E_z component of equation 2.30 for E waves given in chapter 2. Assuming frequency dependant conductivity $g_e(s)$ and electrical susceptibility $\chi_{e1}(s)$, the equation becomes,

$$2(V_1^i + V_2^i + V_3^i + V_4^i) = 4V_z + g_e(s)V_z + 2\bar{s}\chi_{e1}(s)V_z \tag{6.31}$$

This formulation presented in J. Paul's thesis [17] can be used for arbitrary $g_e(s)$ and $\chi_{e1}(s)$.

However, as noted previously, the conductivity (from the imaginary part of permittivity/susceptibility) is not independent of the real part of the susceptibility except the frequency independent constants. The Kramer's Kronig relations does not relate the constant values $g_e(\infty)$ and $\chi_{e1}(\infty)$. Hence, linear materials can be divided into two categories.

- constant $\chi_e(\infty)$ and constant $g_e(\infty)$ (simple).
- frequency dependant $\chi_e(z)$ and constant $g_e(\infty)$ (dispersive).

The first is a simple lossy dielectric which was addressed in the beginning of this study. The second form represents materials with a frequency dependant real part of susceptibility ($\chi_{e1}(\omega)$) and frequency independent imaginary part of susceptibility (χ_{e2}) and materials with frequency dependant real and imaginary parts $\chi_e(\omega)$ inter-related by the Kramer's Kronig relations.

In order to illustrate this further, consider a material with general complex susceptibility $\chi_e(s) = \chi_{en}(s)/\chi_{ed}(s)$ expressed as a rational polynomial, where $\chi_{en}(s) = a_0 + a_1 s + a_2 s^2 + \ldots$ and $\chi_{ed}(s) = b_0 + b_1 s + b_2 s^2 + \ldots$. Then

$$\begin{aligned}\chi_{en}(\omega) &= (a_0 - a_2\omega^2 + a_4\omega^4 + \ldots) + j\omega(a_1 - a_3\omega^2 + a_5\omega^4 + \ldots) \\ &= \chi_{en}^r(\omega) + j\omega\chi_{en}^i(\omega) \qquad (6.32)\\ \chi_{ed}(\omega) &= (b_0 - b_2\omega^2 + b_4\omega^4 + \ldots) + j\omega(b_1 - b_3\omega^2 + b_5\omega^4 + \ldots) \\ &= \chi_{ed}^r(\omega) + j\omega\chi_{ed}^i(\omega) \qquad (6.33)\end{aligned}$$

where a superscript r denotes real part, a superscript i denote imaginary part and subscripts en and ed denote numerator and the denominator of the

complex electrical susceptibility. It should be noted that in determining the frequency response, from the s domain model by substituting s with $j\omega$, the real parts consist of even orders of ω whereas the imaginary parts consist of odd orders of ω.

The frequency dependant real part and imaginary part of susceptibility are given by,

$$\chi_{e1}(\omega) = \frac{\chi^r_{en}(\omega)\chi^r_{ed}(\omega) + \omega^2\chi^i_{en}(\omega)\chi^i_{ed}(\omega)}{\left(\chi^r_{ed}(\omega)\right)^2 + \left(\chi^i_{ed}(\omega)\right)^2} \tag{6.34}$$

$$\chi_{e2}(\omega) = \omega\frac{\chi^i_{en}(\omega)\chi^r_{ed}(\omega) - \chi^r_{en}(\omega)\chi^i_{ed}(\omega)}{\left(\chi^r_{ed}(\omega)\right)^2 + \left(\chi^i_{ed}(\omega)\right)^2} \tag{6.35}$$

The denominator of $\chi_{e1}(\omega)$ and $\chi_{e2}(\omega)$ now has only even order of ω. The numerator of $\chi_{e1}(\omega)$ have only even orders while that of $\chi_{e2}(\omega)$ contains only odd orders of ω.

From $\chi_{e2}(\omega)$, the conductance $\sigma_e(\omega)$ can be obtained as,

$$\sigma_e(\omega) = \varepsilon_0\frac{\omega^2\left\{\chi^i_{en}(\omega)\chi^r_{ed}(\omega) - \chi^r_{en}(\omega)\chi^i_{ed}(\omega)\right\}}{\left(\chi^r_{ed}(\omega)\right)^2 + \left(\chi^i_{ed}(\omega)\right)^2} \tag{6.36}$$

Now both the numerator and the denominator of $\sigma(\omega)$ have even orders of ω. As per the process in modelling $\chi_{e1}(\omega)$ and $\sigma_e(\omega)$, they are expressed in the s-domain by replacing ω^2 with $-s^2$, before fitting into the last two terms of equation 6.31. Note that by now, all the coefficients of the numerators and denominators of both $\chi_{e1}(s)$ and $\sigma_e(s)$ are real.

However, they have to be normalised using $g_e(s) = \sigma_e(s)\Delta l\eta_0\sqrt{2}$ and $s = \bar{s}/\Delta t$ noting from chapter 2 that $\Delta l/\Delta t = \sqrt{2}c$ for two dimensional TLM, where $\eta_0 = \sqrt{\mu_0}\varepsilon_0$. Hence, the last two terms of the equation 5.31 then

becomes,

$$\{g_e(s) + 2\bar{s}\chi_{e1}(s)\} V_z = \{2\Delta t\sigma_e(s)/\varepsilon_0 + 2s\Delta t\chi_{e1}(s)\} V_z \tag{6.37}$$

$$= 2\Delta t \left\{ -s^2 \frac{\chi^i_{en}(s)\chi^r_{ed}(s) - \chi^r_{en}(s)\chi^i_{ed}(s)}{\left(\chi^r_{ed}(s)\right)^2 + \left(\chi^i_{ed}(s)\right)^2} \right.$$

$$\left. +2s \frac{\chi^r_{en}(s)\chi^r_{ed}(s) - s^2\chi^i_{en}(s)\chi^i_{ed}(s)}{\left(\chi^r_{ed}(s)\right)^2 + \left(\chi^i_{ed}(s)\right)^2} \right\} V_z \tag{6.38}$$

$$= 2s\Delta t \left\{ \frac{\left(\chi^r_{ed}(s) + s\chi^i_{ed}(s)\right)\left(\chi^r_{en}(s) - s\chi^i_{en}(s)\right)}{\left(\chi^r_{ed}(s)\right)^2 + \left(\chi^i_{ed}(s)\right)^2} \right\} V_z \tag{6.39}$$

$$= 2\bar{s} \left\{ \frac{a_0 + a_1 s + a_2 s^2 + \dots}{b_0 + b_1 s + b_2 s^2 + \dots} \right\} V_z = 2\bar{s}\chi_e(s)V_z \tag{6.40}$$

This proves that using the complete susceptibility function in s is equivalent to using separate conductance and real part of susceptibility. In the second case, if they are implemented in separate paths to be added at a later stage, the cost of computation and storage will be doubled since the order of s in the numerator and denominator are doubled when separating the real part and imaginary part. However, it should be noted that this does not take into account any frequency independant conductivity present in the material which must be modelled via a constant g_e. Hence, the voltage equation is re written as follows,

$$2(V^i_1 + V^i_2 + V^i_3 + V^i_4) = 4V_z + g_e V_z + 2\bar{s}\chi_e(s)V_z \tag{6.41}$$

Once transformed to the z domain, the equation becomes,

$$2(V^i_1 + V^i_2 + V^i_3 + V^i_4) = 4V_z + g_e V_z + 4\left(\frac{1 - z^{-1}}{1 + z^{-1}}\right)\chi_e(z)V_z \tag{6.42}$$

In order to separate $\chi_e(z)$ into two parts, so that one part is independant of z^{-1} (i.e. only dependant on value at the current time step) and the other part is dependant on z^{-1} (i.e. dependant only on values at previous time steps)

partial fractions as follows [17],

$$(1 - z^{-1})\chi_e = \chi_e^0 - z^{-1}(\chi_e^1 + \bar{\chi}_e(z)) \tag{6.43}$$

By rearranging equation 6.42, and substituting the relations one eventually arrives at,

$$V_z = \kappa_{ez} \left\{ 2V_z^i + z^{-1}S_{ez} \right\} \tag{6.44}$$

$$S_{ez} = 2V_z^i - (4 + g_e - 4\chi_e^1)V_z + S_{er} \tag{6.45}$$

$$S_{er} = 4\bar{\chi}_e(z)V_z \tag{6.46}$$

where $\kappa_{ez} = 1/(4 + g_e + 4\chi_e^0)$ is a constant and $V_z^i = V_1^i + V_2^i + V_3^i + V_4^i$ is the incident link voltages into the node. In order to implment the $S_{er}(z)$ with the least number of variables to hold past information, one can express $S_{er}(z)$ as,

$$\begin{aligned} S_{er} &= \gamma_0 V_z + z^{-1}S_{er1} \\ S_{er1} &= \gamma_1 V_z + \delta_1 S_{er} + z^{-1}S_{er2} \\ &\vdots \\ S_{ern} &= \gamma_n V_z + \delta_n S_{er} \end{aligned}$$

given,

$$\bar{\chi}_e(z) = \frac{\gamma_0 + \gamma_1 z^{-1} + \ldots + \gamma_n z^{-n}}{1 + \delta_1 z^{-1} + \ldots + \delta_n z^{-n}} \tag{6.47}$$

In order to model the materials discussed previously Caucy, Sellmeier and Drude models are transformed into the z-domain and partial fractions χ_e^0, χ_e^1 and $\bar{\chi}_e(z)$ for each model are presented next.

Cauchy Model

From the s-domain model, one can obtain $\chi_{e,Cauchy}(z)$ by bilinear transform as,

$$\chi_{e,cauchy}(z) = A - B_z \left(\frac{1 - z^{-1}}{1 + z^{-1}}\right)^2 + C_z \left(\frac{1 - z^{-1}}{1 + z^{-1}}\right)^4 \tag{6.48}$$

where $B_z = B/(\pi c \Delta t)^2$ and $C_z = C/(\pi c \Delta t)^4$. From partial fractions one can obtain,

$$(1-z^{-1})\chi_{e,Cauchy}(z) = \chi_{e0,Cauchy} - z^{-1}\left\{\chi_{e1,Cauchy} + \frac{a_0 + a_1 z^{-1} + a_2 z^{-2} + a_3 z^{-3}}{1 + 4z^{-1} + 6z^{-2} + 4z^{-3} + z^{-4}}\right\} \tag{6.49}$$

where

$$\chi_{e0,Cauchy} = \chi_{e1,Cauchy} = A - B_z + C_z \tag{6.50}$$

$$a_0 = -a_3 = -4B_z + 8C_z \tag{6.51}$$

$$a_1 = -a_2 = -4B_z - 8C_z \tag{6.52}$$

Sellmeier Model

From the s-domain model, by bilinear z-transform as,

$$\chi_{e,Sellmeier}(z) = A_0 + A_1 \frac{(1+z^{-1})^2}{(1+z^{-1})^2 + \gamma_1^2(1-z^{-1})^2} \tag{6.53}$$

where $\gamma_1 = a_1/(\pi c \Delta t)$. From partial fractions,

$$(1-z^{-1})\chi_{e,Sellmeier} = \chi_{e0,Sellmeier} - z^{-1}\left\{\chi_{e1,Sellmeier} + \frac{a_0 + a_1 z^{-1}}{1 + b_1 z^{-1} + z^{-2}}\right\} \tag{6.54}$$

where

$$\chi_{e0,Sellmeier} = \chi_{e1,Sellmeier} = A_0 + \frac{A_1}{1+\gamma_1^2} \tag{6.55}$$

$$a_0 = -a_1 = -4A_1 \frac{\gamma_1^2}{(1+\gamma_1^2)^2} \tag{6.56}$$

$$b_1 = 2\left(\frac{1-\gamma_1^2}{1+\gamma_1^2}\right) \tag{6.57}$$

Drude Model

From s-domain model, by bilinear transform as,

$$\chi_{e,Drude}(z) = \chi_{e\infty} + \frac{A\Omega_0^2(1+z^{-1})^2}{(1-z^{-1})^2 + \Gamma(1-z^{-2}) + \Omega_0^2(1+z^{-1})^2} \tag{6.58}$$

where $\Omega_0 = \omega_0 \Delta t/2$ and $\Gamma = \gamma \Delta t/2$. From partial fractions,

$$(1-z^{-1})\chi_{e,Drude} = \chi_{e0,Drude} - z^{-1}\left\{\chi_{e1,Drude} + \frac{a_0 + a_1 z^{-1}}{1 + b_1 z^{-1} + b_2 z^{-2}}\right\} \tag{6.59}$$

where,

$$\chi_{e0,Drude} = \chi_{e\infty} + \frac{A\Omega_0^2}{1+\Gamma+\Omega_0^2} \tag{6.60}$$

$$\chi_{e1,Drude} = \chi_{e\infty} + \frac{A\Omega_0^2}{1-\Gamma+\Omega_0^2} \tag{6.61}$$

$$a_0 = \frac{2A\Omega_0^2}{1+\Gamma+\Omega_0^2}\left\{\frac{\Omega_0^2-1}{1+\Gamma+\Omega_0^2} - \frac{\Omega_0^2+1}{1-\Gamma+\Omega_0^2}\right\} \tag{6.62}$$

$$a_1 = \frac{2A\Omega_0^2}{1+\Gamma+\Omega_0^2}\left\{\frac{\Omega_0^2+1}{1+\Gamma+\Omega_0^2} - \frac{\Omega_0^2-1}{1-\Gamma+\Omega_0^2}\right\} \tag{6.63}$$

$$b_1 = 2\frac{\Omega_0^2-1}{1+\Gamma+\Omega_0^2} \tag{6.64}$$

$$b_2 = \frac{1-\Gamma+\Omega_0^2}{1+\Gamma+\Omega_0^2} \tag{6.65}$$

Notes on z-models

The Cauchy model implemented above becomes unstable for the A,B,C parameter values obtained for the three chalcogenide glasses. In the s-domain transfer function there contains only zeros. The zeros are given by,

$$s = \sqrt{\frac{B \pm \sqrt{B^2 - 4AC}}{2A}} \tag{6.66}$$

Both of these zeroes are real and positive for the A,B,C parameter values obtained for the three chalcogenide glasses.

6.5 Plane Wave Reflection of Dispersive Models

In this section, the implemented models are validated by plane wave propagation (1D propagation). The reflection and the transmission of a plane wave incident from free-space to a dispersive material were measured. The simulation parameters are given in table 6.2.

Table 6.2: Simulation parameters to observe reflection from a dispersive material junction

Window size	$X = 50\mu m$
	$Y = \infty$
Step size	$\Delta l = 0.05, 0.025\mu m$
Freespace to material planar boundary	$X = 25\mu m$
Materials	$As_{40}Se_{60}$
	$Ge_{10}As_{23.4}Se_{66.6}$
	$Ge_{17}As_{18}Se_{65}$
Excitation line	$x = 5\mu m$
Excitation Centre Frequency	$f_0 = 200THz$
Gaussian Pulse width	$t = 5fs$
Measurement plane	
Incident & Reflection	$x = 10\mu m$
Transmission	$x = 30\mu m$

The incident, reflection and the transmission waves were measured in the time domain and converted to the frequency domain by a fast Fourier transform (FFT). The reflection obtained from TLM Sellmeier I models for $As_{40}Se_{60}$, $Ge_{10}As_{23.4}Se_{66.6}$, and $Ge_{17}As_{18}Se_{65}$ are presented for TLM space step sizes of $0.05\mu m$ and $0.025\mu m$, along with the theoretical reflection obtained from the

Sellmeier I model, in figure 6.6. Similarly, the transmission obtained from the TLM Sellmeier models for the three glasses are presented along with theoretical transmission obtained for the Sellmeier model in figure 6.7. As a measure of TLM modelling error, the percentage error in reflection and transmission for the three glasses for the two TLM space step sizes are presented in figures 6.8 and 6.9 respectively.

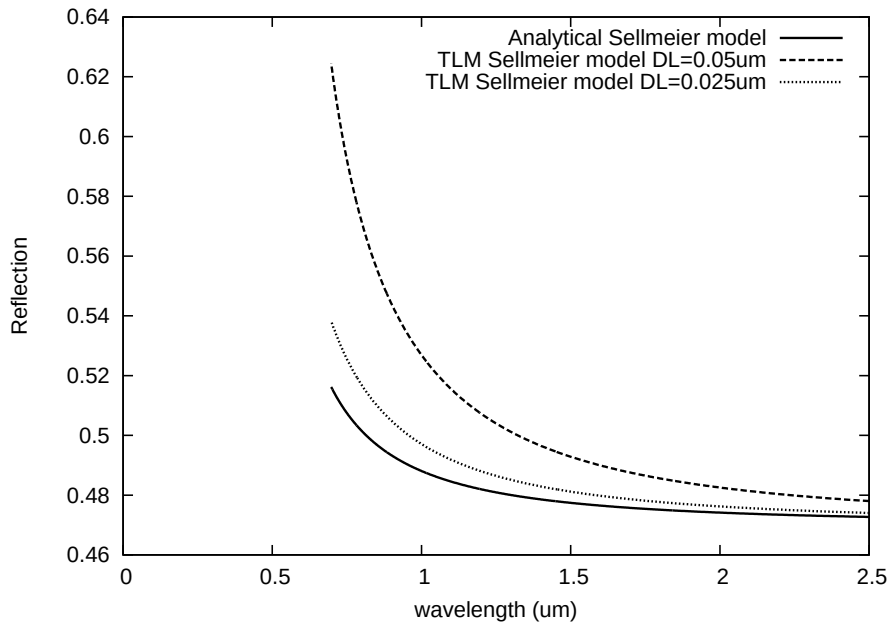

Figure 6.6: Plane wave reflection obtain from TLM Sellmeier I models for $As_{40}Se_{60}$, $Ge_{10}As_{23.4}Se_{66.6}$, and $Ge_{17}As_{18}Se_{65}$ for a space step of $0.05\mu m$, $0.025\mu m$, with theoretical reflecton from Sellmeier I model, when a plane wave is incident from freespace, normal to the boundary.

From figures 6.6 and 6.7, the TLM model is validated against the Sellmeier I model as the results converge towards the theoretical expectation when the space step is decreased.

The error in reflection observed was much larger than the error observed for the transmission for the same parameters. In figure 6.8, at $1500nm$ with $0.05\mu m$, which corresponds to $\lambda/10$ (given that refractive index at $1500nm$ is ≈ 2.8) at that wavelength, the error in reflection is about 4%. Also at

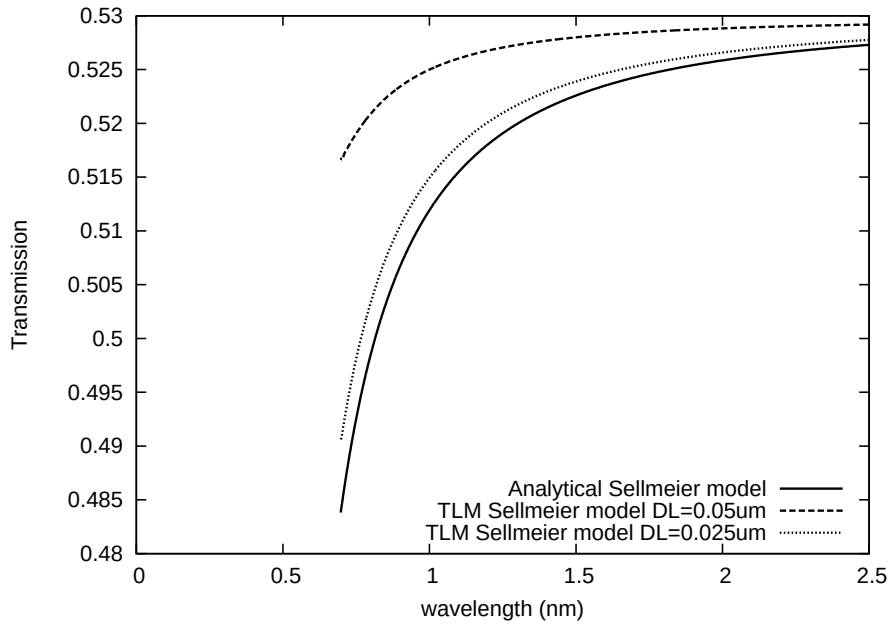

Figure 6.7: Plane wave transmission obtain from TLM Sellmeier I models for $As_{40}Se_{60}$, $Ge_{10}As_{23.4}Se_{66.6}$, and $Ge_{17}As_{18}Se_{65}$ for a space step of $0.05\mu m$, $0.025\mu m$, with theoretical transmission from Sellmeier I model, when a plane wave is incident from freespace, normal to the boundary.

a wavelength of $750nm$ with a TLM space step of $0.025\mu m$ (given that the refractive index at a wavelength of $750nm$ is ≈ 3.2), which corresponds to $\lambda/10$ at $750nm$, the error in reflection is about 4%. This is observed in the discussion of TLM mesh dispersion in [18], which mentions that at $\lambda/10$ the error in velocity is 4%. Hence, the error in reflection is a direct consequence of mesh dispersion. However, the errors in transmission at both locations are about 1%. Hence, it can be concluded that the modelling errors in TLM affects less for transmission, and reflection is the more stringent measure for error analysis.

When an error of about 4% is compared with the modelling error of the Sellmeier model, which was less than 0.1% beyond $700nm$, it is clear that it is more important to reduce TLM mesh dispersion than to accommodate more elaborate models such as the Tauc-Lorentz one.

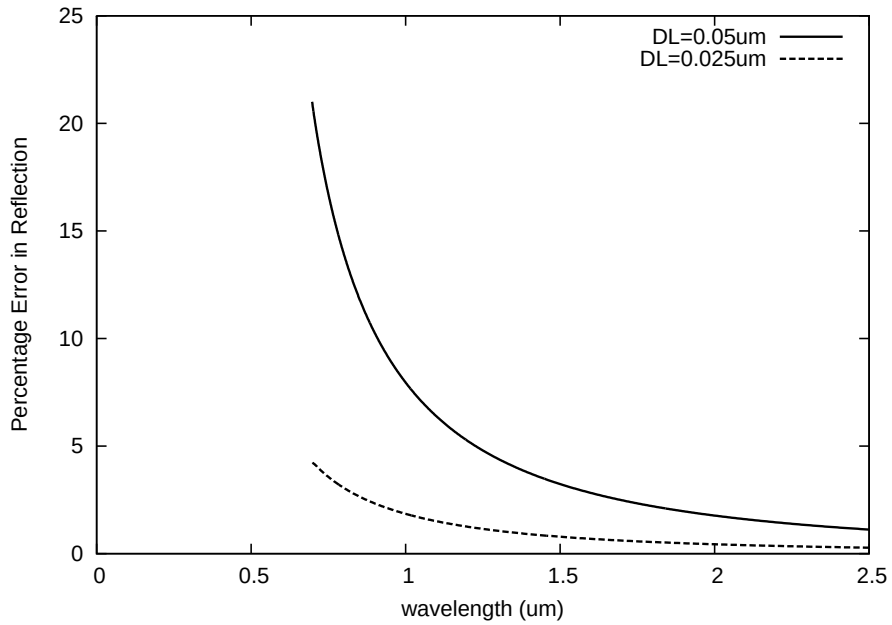

Figure 6.8: Percentage error in plane wave reflection obtain from TLM Sellmeier I models for $As_{40}Se_{60}$, $Ge_{10}As_{23.4}Se_{66.6}$, and $Ge_{17}As_{18}Se_{65}$ for a space step of $0.05\mu m$, $0.025\mu m$, relative to theoretical reflecton from Sellmeier I model, when a plane wave is incident from freespace, normal to the boundary.

6.6 Conclusions

In this chapter, the complex refractive index was assumed to be frequency dependant. In order to describe measured refractive indices of some chalcogenide glasses, several models were discussed. The Cauchy, Sellmeier Drude, and Tauc-Lorentz models were considered as suitable candidates for such modelling. The Tauc-Lorentz model was identified as the best model for chalcogenide glasses representing the complex refractive index for the whole range of the wavelengths of interest. The Drude model and Sellmeier model were the next best, but they were only accurate when the material is significantly transparent (in these glasses for wavelengths above around $700nm$ wavelength). It was also understood that the Sellmeier model with one term with a constant is the suitable Sellmeier model for chalcogenide glasses.

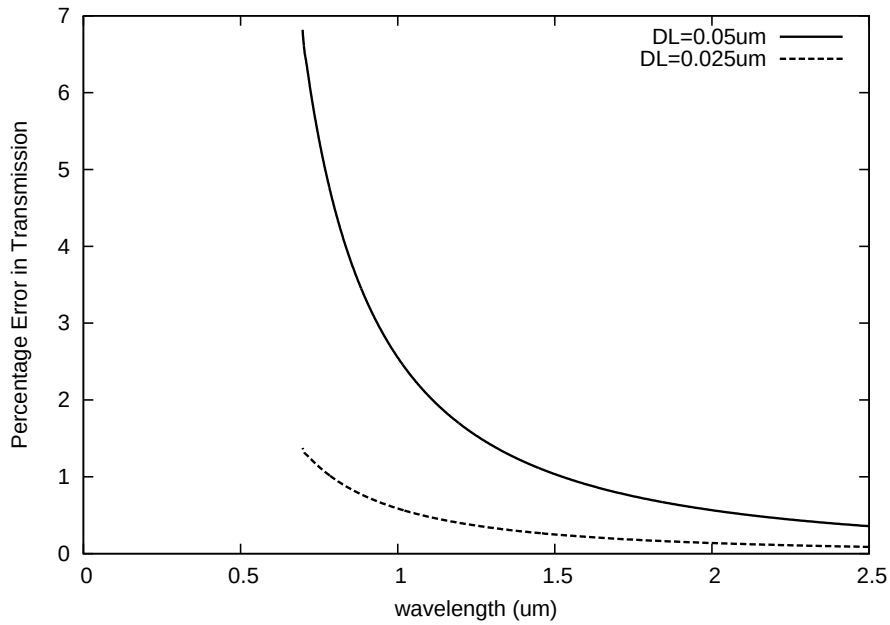

Figure 6.9: Percentage error in plane wave transmission obtain from TLM Sellmeier I models for $As_{40}Se_{60}$, $Ge_{10}As_{23.4}Se_{66.6}$, and $Ge_{17}As_{18}Se_{65}$ for a space step of $0.05\mu m$, $0.025\mu m$, relative to theoretical transmission from Sellmeier I model, when a plane wave is incident from freespace, normal to the boundary.

Then, the dispersive models are accommodated into TLM by means of z-transform. The Sellmeier model was the most suitable candidate as the Cauchy model is unstable due to its non-strict transfer function. The Drude model coincides with the Sellmeier model for the given chalcogenide glasses. The Tauc-Lorentz model included terms that cannot be readily converted to s-domain to be later transformed to z-domain. The plane wave reflection and transmission was observed and the results verify that the TLM models closely represent the Sellmeier model as the space step is decreased. The error in reflection was about 4% and transmission was about 1% when $\lambda = 10\Delta l$. The reflection error was in accordance with the standard TLM mesh dispersion error, and is understood as the better representative of modelling error. Lastly, it was noted that it is more important to minimise the TLM meshing error than to incorporate more elaborate refractive index models in

TLM.

The frequency dependence of chalcogenide glasses were modelled in this chapter from measurement to electromagnetic simulation. The next most important feature of chalcogenide glasses, the nonlinearities is the subject of the next chapter.

References

[1] D. Vernooy, V. Ilchenko, H. Mabuchi, E. Streed, and H. Kimble, "High-q measurements of fused-silica microspheres in the near infrared," *Optics Letters*, vol. 23, no. 4, pp. 247–249, 1998.

[2] A. Seddon, "Chalcogenide glasses: a review of their preparation, properties and applications," *Journal of non-crystalline solids*, vol. 184, pp. 44–50, 1995.

[3] A. Zakery and S. Elliott, *Optical nonlinearities in chalcogenide glasses and their applications*, vol. 135. Springer, 2007.

[4] R. Collin, *Field theory of guided waves*, vol. 2. IEEE press New York, 1991.

[5] V. Janyani, *Modelling of Dispersive and Nonlinear Materials for Optoelectronics using TLM*. PhD thesis, The University of Nottingham, 2005.

[6] J. Liu, *Photonic Devices*. Cambridge University Press, 2005.

[7] R. Ditchburn, *Light*. Dover Books on Physics, Dover Publications, 1991.

[8] G. Jellison and F. Modine, "Parameterization of the optical functions of amorphous materials in the interband region," *Applied Physics Letters*, vol. 69, no. 3, pp. 371–373, 1996.

[9] E. Palik, *Handbook of optical constants of solids*, vol. 3. Academic press, 1998.

[10] G. Ghosh, *Handbook of thermo-optic coefficients of optical materials with applications*, vol. 5. Academic Pr, 1998.

[11] G. E. Jellison, Jr. and F. A. Modine, "Erratum: Parameterization of the optical functions of amorphous materials in the interband region," *Applied Physics Letters*, vol. 69, no. 14, pp. 2137–2137, 1996.

[12] Z. Lian, *Fabrication of Rib Waveguides and Optical Fibres in Chalcogenide Glasses*. PhD thesis, The University of Nottingham, 2011.

[13] S. Adachi and S. Ozaki, "Optical constants of amorphous ga2se3," *Japanese Journal of Applied Physics Part 1 Regular Papers Short Notes and Review Papers*, vol. 32, pp. 4446–4446, 1993.

[14] S. Adachi, H. Mori, and S. Ozaki, "Model dielectric function for amorphous semiconductors," *Physical Review B*, vol. 66, no. 15, p. 153201, 2002.

[15] J. Orava, J. Šik, T. Wagner, and M. Frumar, "Optical properties of assse bulk glasses studied by spectroscopic ellipsometry," *Journal of Applied Physics*, vol. 103, p. 083512, 2008.

[16] I. Ohlídal, D. Franta, M. Šiler, F. Vižd'a, M. Frumar, J. Jedelskỳ, and J. Omasta, "Comparison of dispersion models in the optical characterization of as–s chalcogenide thin films," *Journal of non-crystalline solids*, vol. 352, no. 52, pp. 5633–5641, 2006.

[17] J. Paul, *Modelling of General Electromagnetic Material Properties in TLM*. PhD thesis, The University of Nottingham, 1998.

[18] C. Christopoulos, *The transmission-line modeling method: TLM*. Institute of Electrical and Electronics Engineers, 1995.

7

Nonlinear Models for Chalcogenide Glasses

Optical nonlinearity is the nonlinear relationship between dielectric polarisation and electric field in certain materials, in the presence of various types of fields. The nonlinear effects include thermal, electrical, magnetic and optic. Unlike thermal, electrical, and magnetic effects, optical effects have almost instantaneous response and can be controlled by fast optical signals. On the downside, optical effects are small in magnitude requiring large optical fields in order to take effect. Therefore, optical materials showing high nonlinearity should be combined with structures which enhance the nonlinear characteristics of the underlying material. To this end, modelling of optical components containing nonlinear material is highly influential in taking optical research forward. In this chapter, instantaneous Kerr nonlinearity is looked at in detail from a modelling perspective.

As pointed out in the introductory chapter of this thesis, one of the main advantages of time domain numerical techniques over frequency domain techniques is the ability to solve nonlinear problems with high accuracy. In the previous chapter, TLM was utilised to model dispersion in chalcogenide glass materials. In this chapter, TLM modelling is taken a step further to include

Kerr nonlinearity present in chalcogenide glass materials [1].

In this chapter, a two dimensional stub TLM model and a z-transform model for Kerr nonlinearity are presented. They are compared in the context of a self focusing problem. Results from the models are also compared with those from a time domain approximate beam propagation technique in the context of a nonlinear waveguide junction.

7.1 Optical Nonlinearities

Until now in this study, the polarisation vector was assumed to have a linear relationship with electric field. The last chapter discussed the frequency dependency of this relationship. Due to this assumption, optical beams at one frequency could not affect beams at other frequencies or generate new frequencies. Further, bending of optical beams occurred as a refraction phenomenon only. This excluded the possibility of controlling optical signals via other optical signals. Similar phenomenon in semiconductors in the kilohertz to gigahertz electromagnetic signal regime was solely responsible for the advancement of electrical technologies.

The polarisation vector can be written as a Taylor polynomial of the applied electric field [2], [3].

$$\mathbf{P} = \varepsilon_0 \chi_e \mathbf{E} + \varepsilon_0 \chi_e^{(2)} |E| \mathbf{E} + \varepsilon_0 \chi_e^{(3)} |E^2| \mathbf{E} + \dots \tag{7.1}$$

where χ_e is the linear susceptibility, $\chi_e^{(2)}$ and $\chi_e^{(3)}$ second and third order nonlinear susceptibilities. All susceptibilities are complex in general, where the imaginary part represents loss or gain.

The second order nonlinearity is the strongest and gives rise to phenomena such as second harmonic generation (SHG) and sum and difference frequency generation [3]. However, centrosymmetric (symmetric in all directions) molecules and crystal latices do not exhibit second order nonlinearities [2, 1]. The third order nonlinearity present in most materials occur due to various physical phenomenon. Some result in instantaneous effects such a Kerr

nonlinearity while some result in non-instantaneous effects such as Raman nonlinearity.

7.1.1 Kerr Nonlinearity

Kerr nonlinearity in material is a third order nonlinearity where the refractive index of the material at a given time depends on the optical power intensity. Theoretically this effect is taken as instantaneous since in most materials the response time for Kerr nonlinearity is small.

Instantaneous Kerr nonlinearity is the most desired form of nonlinearity due to its self focusing effects and its usability in all optical control. In most materials, including silica, its magnitude is small, requiring high optical power to induce such effects. However, such high optical power either breaks down the material or activates multi photon absorption, another nonlinear absorptive effect, resulting in a thermal fusing of the material. There has been a growing interest in this research area due to some semiconductors such as *Gallium Arsenide* showing Kerr effects more than three orders of magnitude higher than that of silica. Chalcogenide glass materials which contain some semiconductor elements, also show similar Kerr effects.

The refractive index of a Kerr nonlinear material is given by,

$$n = n_0 + n_2 I \tag{7.2}$$

where n_0 is the linear refractive index, n_2 is the Kerr coefficient and I is the optical intensity. The nonlinear coefficient can either be positive or negative and the materials are termed accordingly (i.e. "positive-Kerr materials" and "negative-Kerr materials"). Kerr nonlinearity is also widely defined as a third order nonlinear susceptibility $\chi_e^{(3)}$.

$$n_2 = \frac{3\chi_e^{(3)}}{4c\varepsilon_0(\chi_e + 1)} \tag{7.3}$$

where c is the velocity of light in vacuum, and χ_e is the linear electrical

susceptibility. Equations 7.1, 7.2 and 7.3 are linked together by the optical intensity $I = |E^2|/(2\eta)$, where $\eta = \eta_0/n_0$.

The Kerr coefficient combined with the local instantaneous intensity is a measure of the change of refractive index and all the consequent effects depend on this combination $n_2 I$. Usually the maximum nonlinear change in the refractive index is limited by the maximum electric field intensity that the material can withstand. Materials like silica have a small Kerr coefficient around $2 \times 10^{-17} m^2/W$, whereas materials like chalcogenide glasses and $AlGaAs$ have high Kerr coefficients around $2 \times 10^{-13} m^2/W$ [3, 1].

7.2 Formulation

Instantaneous Kerr nonlinearity can be modelled in TLM as a sudden increment(decrement) of the local electrical susceptibility function. Hence, an additional (reductional) stub at the centre of the TLM node can model Kerr nonlinearity. V.Janyani [4] has proposed a stub addition for incremental changes of refractive indices for TLM nodes in 1 dimension. In this section this method is further generalised to 2 dimensions. Alternatively, J.Paul [5, 6] has proposed a z-transform based Kerr nonlinearity implementation of a simpler formulation. This implementation is also pursued in this study to compare their similarities and limitations.

7.2.1 2D Nonlinear Stub model

The stub that used to model increased permittivity can be used to express the time dependent changes of refractive index. Hence, by intuition, stubs can be added at each time step to represent incremental changes in refractive index as they would occur on top of the stubs already present. However, this would lead to a very complex TLM node, which grows over time.

The solution given by V.Janyani[4] to overcome this problem is to obtain an equivalent stub at each time step to combine the two stubs. This method essentially maintains a single stub, the properties of which changes over time.

The following briefly underlines the concept.

Consider electrical susceptibility at time k, $\chi_{ek} = \chi_{e(k-1)} + \chi_{e\Delta}$. The added stub looks like figure 7.1 and can be reduced as illustrated. As soon as the differential stub is introduced, its incident voltage will be zero.Hence, the combined stub can be reduced as shown. As shown in chapter 2, a stub corresponding to χ_e is given by $Y_s = 4\chi_e/Z_{TL}$, which can be used to express an increment of $\chi_{e\Delta}$. Thus:

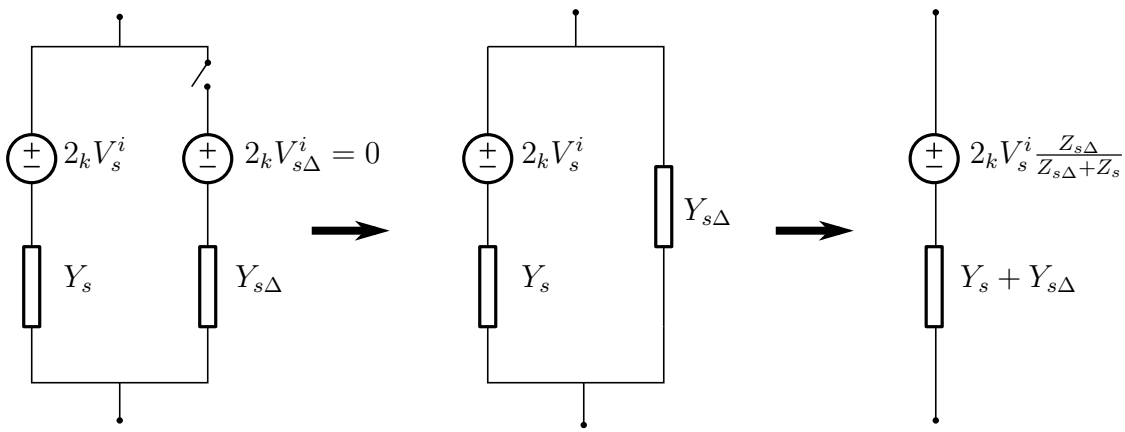

(a) Newly Connected Stub (b) Reducing Stub (a) Resultant Stub

Figure 7.1: Incremental Stub Reduction to a Single Stub

$$Y_{s\Delta} = 4\frac{\chi_{e\Delta}}{Z_{TL}} \tag{7.4}$$

From the above equation, the voltage of the TLM node voltage V_z can be obtained by modifying the linear formulation slightly, as proven by Janyani, [4], as follows.

$$V_z = \frac{2(V_1^i + V_2^i + V_3^i + V_4^i) + 2V_s^i \frac{Z_{s\Delta}}{Z_{s\Delta}+Z_s}(Y_s + Y_{s\Delta})Z_{TL}}{4 + g_e + (Y_s + Y_{s\Delta})Z_{TL}} \tag{7.5}$$

The above can be reduced to the following equation by incorporating terms involving susceptibilities and eliminating admittances.

$${}_kV_z = \frac{2({}_kV_1^i +_k V_2^i +_k V_3^i +_k V_4^i) + 8_kV_{s\,(k-1)}^i\chi_e}{4 + g_e + 4_k\chi_e} \tag{7.6}$$

The only unknown in this equation is ${}_k\chi_e$, which changes instantaneously with $|\mathbf{E}|$. From equation 7.2 and the definition of optical intensity I as,

$$I = \frac{V_z^2 n_0}{2(\Delta l)^2 \eta_0} \tag{7.7}$$

$$\tag{7.8}$$

By definition the electrical susceptibility at time instant k is given by,

$${}_k\chi_e = ({}_kn)^2 - 1 \tag{7.9}$$

In Kerr media $n_2 I$ term is usually less than 0.01 [4]. This limit is imposed by the maximum electric field tolerated by the material. Therefore, when expressing $({}_kn)^2$, the $n_2^2 I^2$ term can be neglected. Hence,

$${}_k\chi_e = \chi_e + 2n_2 \frac{V_z^2(\chi_e + 1)}{2(\Delta l)^2 \eta_0} \tag{7.10}$$

By substituting equation 7.10 in equation 7.6 one obtains,

$${}_kV_z \left\{4 + g_e + 4\chi_e\right\} + 4\left\{\frac{n_2(1+\chi_e)}{(\Delta l)^2\eta_0}\right\}({}_kV_z)^3 = 2({}_kV_1^i + {}_kV_2^i + {}_kV_3^i + {}_kV_4^i) + 8{}_kV_{s\,(k-1)}^i\chi_e \tag{7.11}$$

The above equation is a cubic polynomial of ${}_kV_z$, where the right hand side is a constant for a given step. Hence, one has to solve a cubic polynomial of the form $x^3 + px = q$. Because p and q^2 are always positive, the equation has only one real root, which can be expressed as [7],

$${}_kV_z = [R + \sqrt{Q^3 + R^2}]^{1/3} + [R - \sqrt{Q^3 + R^2}]^{1/3} \tag{7.12}$$

where $R = W_z/8\chi_{e\Delta}\prime$, $Q = (4 + g_e + 4\chi_e)/12\chi_{e\Delta}\prime$, W_z is the R.H.S of equation 7.11, and $\chi_{e\Delta}\prime = n_2(\chi_e + 1)/(\Delta l)^2\eta_0$. However, this requires one to use an iterative root finding algorithm for cubic root twice and square root twice. Therefore, it is much more economical to use one of Householder's methods (Newton Raphson, Halley's method, etc.)[7] to solve equation 7.11 directly.

${}_kV_z = W_z/(4 + g_e + 4\chi_e)$ gives a good initial guess since $4\chi_{e\Delta}({}_kV_z)^2 \ll 1$.

7.2.2 2D Nonlinear Z tansform model

By extending the model obtained for a dispersive material in the previous chapter, using the polarisation vector, one can obtain [6],

$$2(V_1^i + V_2^i + V_3^i + V_4^i) = 4V_z + g_e V_z + 2\bar{s}\chi_e(s)V_z + 2\bar{s}\chi_{eK}V_z^3 \tag{7.13}$$

where $\chi_{eK} = \frac{3}{4}\chi_e^{(3)}/(\Delta l)^2$. As with the dispersive model, the bilinear z-transform is then used once the partial fraction for $(1 - z^{-2})\chi_e(z)$ is found as mentioned in the last chapter. Hence the voltage calculation equation becomes,

$$(4 + g_e + 4\chi_e^0)V_z(z) + 4\chi_{eK}V_z(z)^3 = \left\{2V_z^i + z^{-1}S_{ez}(z)\right\} \tag{7.14}$$

$$S_{ez}(z) = 2V_z^i - (4 + g_e - 4\chi_e^1)V_z - S_{er}(z) + S_{eNL} \tag{7.15}$$

$$S_{er}(z) = 4\bar{\chi}_e(z)V_z \tag{7.16}$$

$$S_{eNL} = 4\chi_e^{(3)}V_z^3 \tag{7.17}$$

Again, equation 7.14 is a cubic equation in V_z and can be solved using an iterative method, discussed for the Stub model in section 7.2.1.

7.3 Modelling of Nonlinear Waveguide Junction

Nonlinear waveguides are important as controlling components in integrated optics [3]. There exists a myriad of problems regarding nonlinear waveguides. Very interesting phenomena occur in coupled nonlinear waveguides, waveguide lattices etc. However, the model built according to the above formulation needs to be validated before exploiting it for more complex problems. In this

section a linear to nonlinear waveguide junction is modelled to observe the reflection at varying intensity levels as first studied by Janyani [4], and was compared with a nonlinear time domain beam propagation method (TDBPM) developed by Khai Le [8].

The nonlinear waveguide junction was constructed as illustrated in figure 7.2 with a space step of $0.05\mu m$. The cladding is linear with a refractive index $n_{cl} = 1.487$. The linear refractive index of the waveguide core was $n_c = 1.491$ throughout the whole waveguide structure and in the nonlinear section, the Kerr coefficient $n_2 = 2\times10^{-17}m^2/W$. The width of the waveguide $h = 3.1\mu m$. The simulation boundary was terminated with a PML layer of 25 cells. The fundamental TE01 mode of the waveguide was excited at a centre wavelength of $1.53\mu m$ and with Gaussian pulse widths of $18fs$ and $36fs$ in two separate simulations.

The transmitted field was captured within the nonlinear region as soon as the pulse completely enters the nonlinear region. The end of the pulse was taken as when the electric field is 0.01 times the maximum electric field of the pulse. The reflected field was captured at the same time in the linear region. The incident field was captured within the linear region at the beginning of the simulation. The normalised transmission(T) and reflection(R) coefficients are defined as follows.

$$T = \frac{\int_{-Y}^{Y}\int_{x_0}^{\infty} E_z^t(x,y)dy\,dx}{\int_{-Y}^{Y}\int_{-\infty}^{x_0} E_z^i(x,y)dy\,dx} \tag{7.18}$$

$$R = \frac{\int_{-Y}^{Y}\int_{-\infty}^{x_0} E_z^r(x,y)dy\,dx}{\int_{-Y}^{Y}\int_{-\infty}^{x_0} E_z^i(x,y)dy\,dx} \tag{7.19}$$

where $Y = 1.55\mu m$ when calculating transmission and reflection within the core and $Y = 25\mu m$ when calculating the total transmission and reflection. x_0 is the x-plane of the junction as illustrated in figure 7.2, E_z^i, E_z^r, E_z^t are the captured incident, reflected and transmitted fields respectively.

The normalised core reflection and total reflection, computed as mentioned

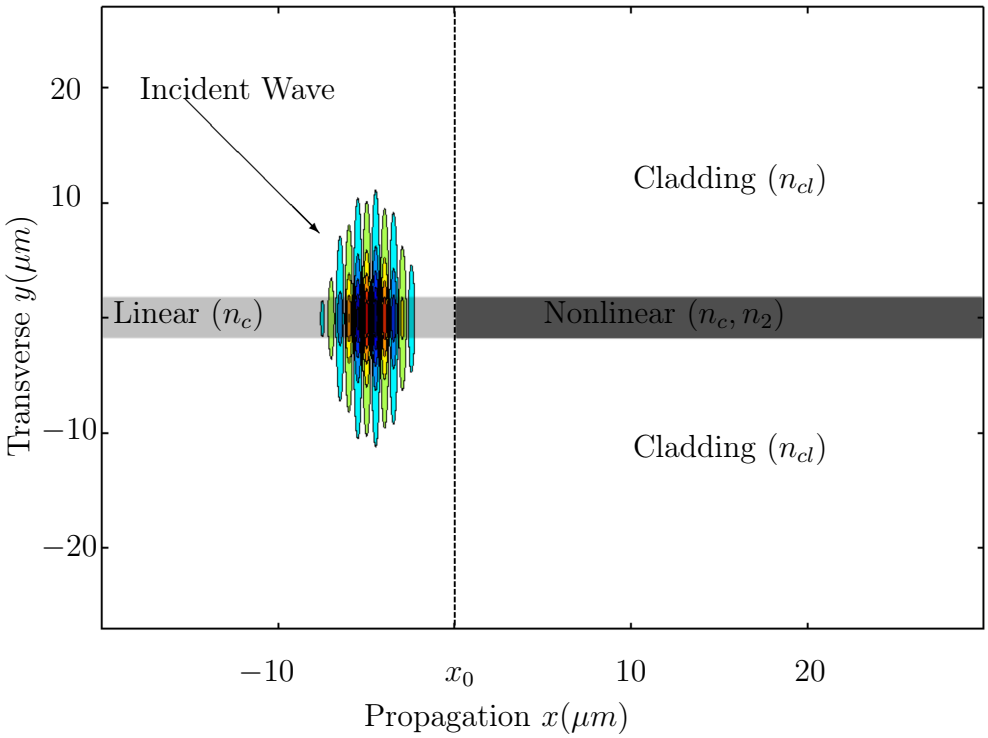

Figure 7.2: Linear to nonlinear waveguide junction where cladding refractive index $n_{cl} = 1.487$, core linear refractive index $n_c = 1.491$, nonlinear Kerr coefficient $n_2 = 2 \times 10^{-17} m^2/W$, core width $h = 3.1\mu m$. The computational domain is truncated by PML.

above, are plotted in figures 7.3, 7.4 against the $n_2 I$ parameter, whereas the normalised core transmission and total transmission are plotted in figures 7.5 and 7.6 respectively. Note that I is the maximum intensity of the incident pulse; hence the parameter $n_2 I$ is the maximum refractive index change experienced by the pulse.

When the core is linear, the pulse which is excited in the mode of the centre wavelength, should travel forward with zero reflection. A very minute back scattering can sometimes occur in numerical simulations due to two reasons. Since the pulse is excited with the mode of the centre wavelength, the mode shape variation within the pulse bandwidth may scatter some power to adjust the overall field of the pulse. The other back scattering is due to the excitation in the TLM mesh. Both these effects are negligible in the present simulations

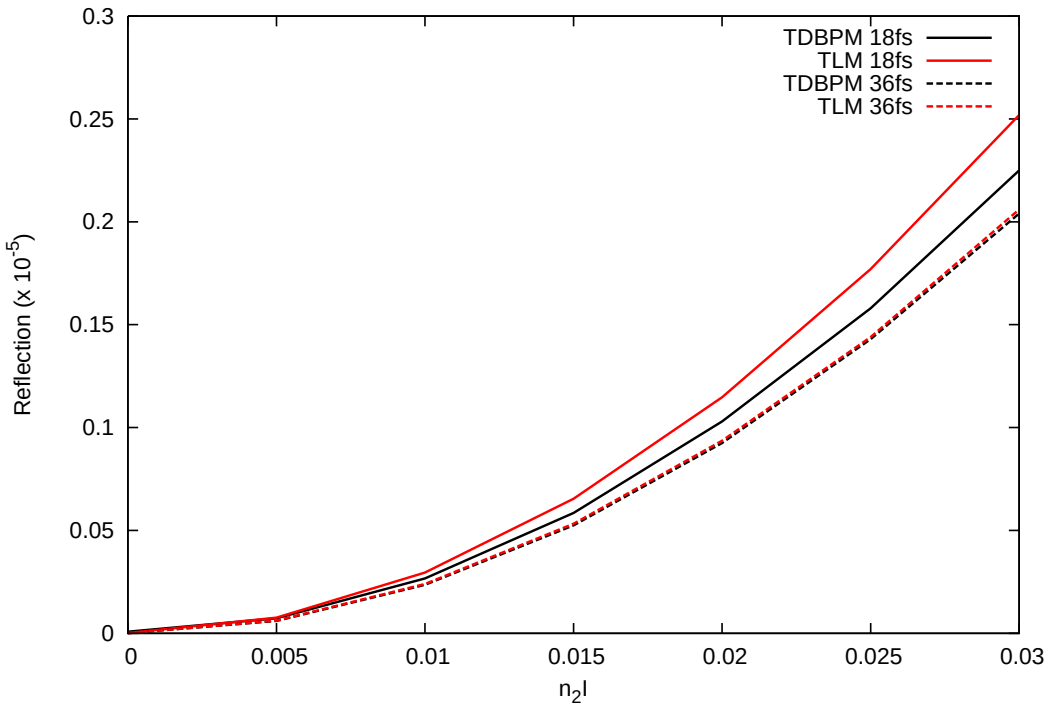

Figure 7.3: Normalised reflection within the core from the linear to nonlinear junction as a function of maximum refractive index change for pulses of pulse widths $18fs$ (solid) and $36fs$ (dashed) in both TDBPM(blue) and TLM(red) simulations.

as the amount of such back scattering is less than 10^{-7} of the total power of the incident pulse.

The nature of the back scattering changes, and becomes significant, when the amplitude of the pulse incident upon the nonlinear junction increases so that $n_2 I > 0.005$. This nonlinear back scattering consists of high frequency components [9]. TD BPM methods, which only approximate the envelope and not the underlying high frequency signal, can model this back scattering to some extent [10]. The generalised nonlinear Shrodinger equation (GNLSE) method as developed by E. Romanova *et. al* [9], does not model back scattering at all, since only forward propagation was considered in their model.

Also, it is very interesting to note that the total reflection at the nonlinear

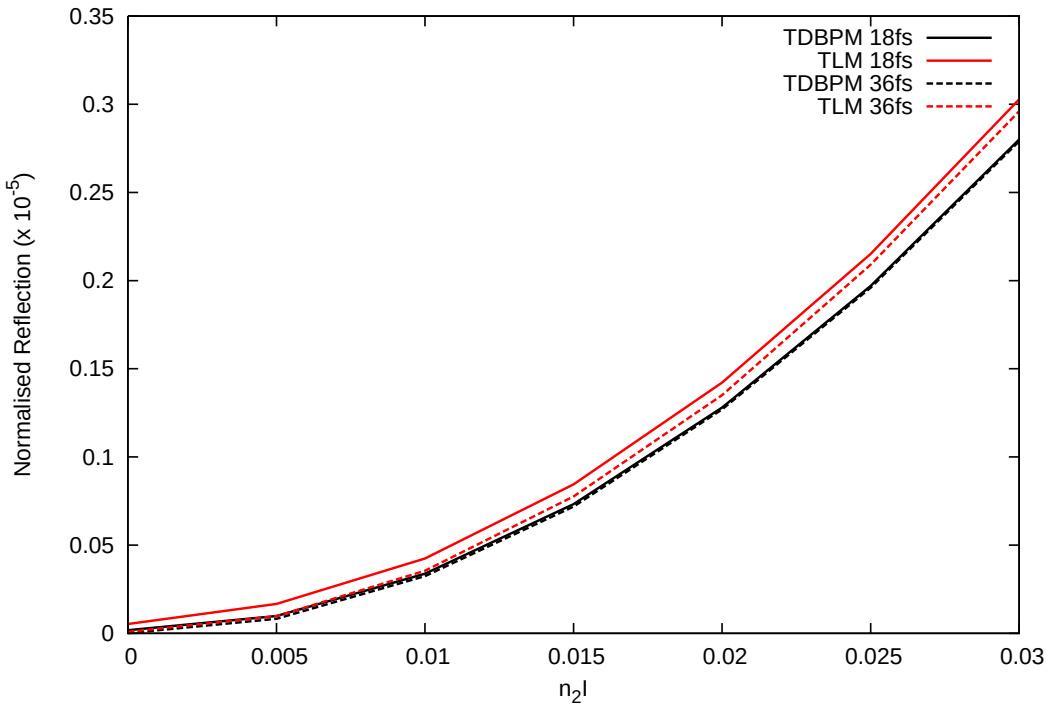

Figure 7.4: Normalised total reflection from the linear to nonlinear junction as a function of maximum refractive index change for pulses of pulse widths $18fs$ (solid) and $36fs$ (dashed) in both TDBPM(blue) and TLM(red) simulations.

waveguide junction did not vary much with the pulse duration. For the same peak I, a longer pulse duration means more cycles in the pulse; hence more energy in the pulse. Therefore, it can be deduced that the amount of reflection depends only upon the pulse height and maximum change of refractive index ($n_2 I$), but not upon the total pulse energy. The total reflection modelled by TLM and TDBPM is close in magnitude as can be seen from figure 7.4. However, the core reflection modelled by TLM becomes larger than that modelled by TDBPM for shorter pulse widths. This might be due to a frequency dependent reflection at the junction. Narrower pulses have broader bandwidths in the frequency domain. BPM methods are band limited [11]. The amount of bandwidth (or in the frequency domain beam angle) that a

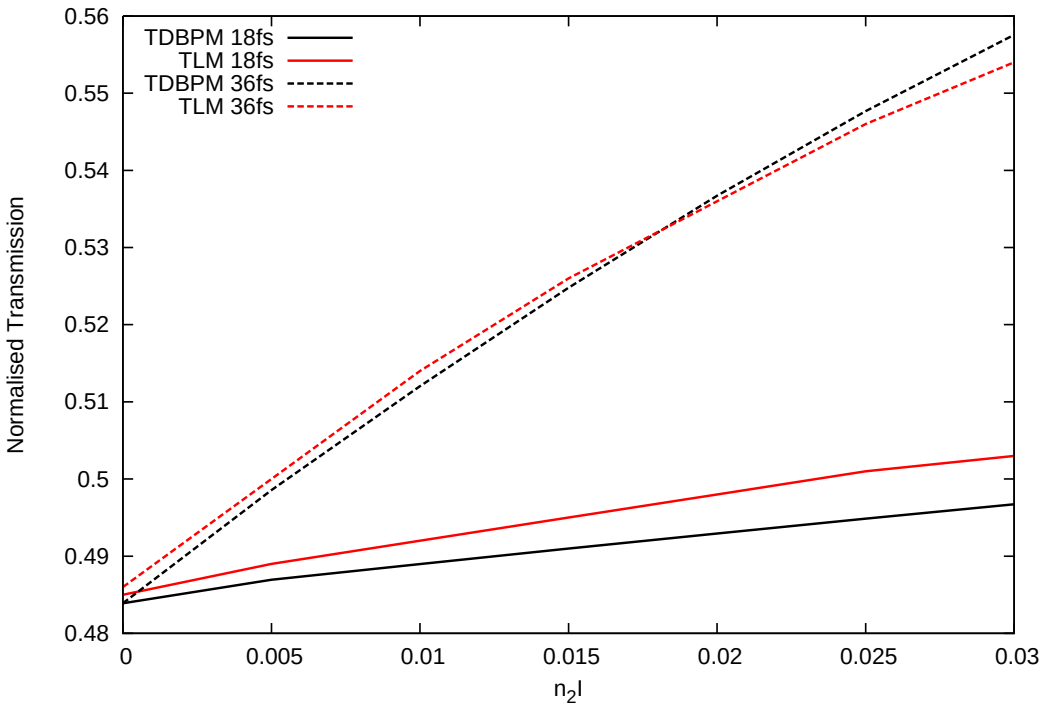

Figure 7.5: Normalised transmission within the core from the linear to nonlinear junction as a function of maximum refractive index change for pulses of pulse widths $18fs$ (solid) and $36fs$ (dashed) in both TDBPM(blue) and TLM(red) simulations.

BPM method can handle depends on the Pade approximant's order of the differential operator of its fundamental equation [10]. In this case, a modified Pade (1,1) was implemented in the TDBPM method, which provides a more wide angled (more bandwidth) BPM than a simple Pade (1,1) approximation, but is still band limited [12]. Therefore, the narrower pulse having a larger bandwidth is prone to more error.

When the transmission in the core is considered in figure 7.5, the transmission is seen to increase with both incident power and pulse width. This is due to the self focusing effect of the nonlinear core. In other words, the more the nonlinear effect (n_2I), the more the concentration of power in the core. It is interesting to note that TLM and TDBPM agree well on the sensitive scale

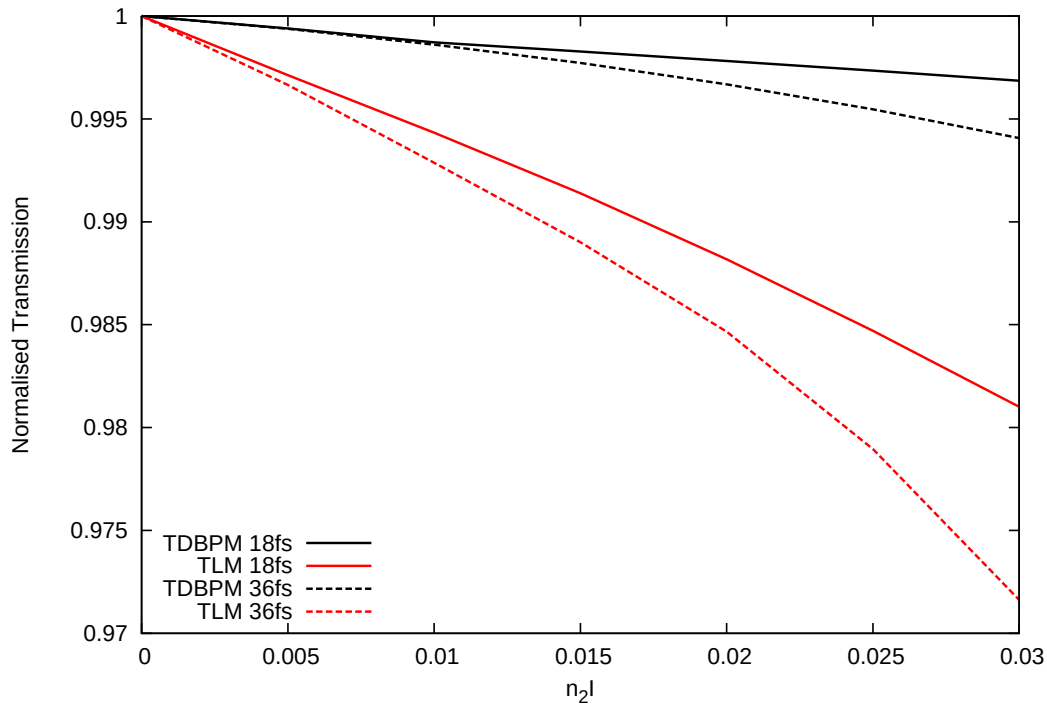

Figure 7.6: Normalised total transmission from the linear to nonlinear junction as a function of maximum refractive index change for pulses of pulse widths $18fs$ (solid) and $36fs$ (dashed) in both TDBPM(blue) and TLM(red) simulations.

shown.

The total transmission shown in figure 7.6 shows a different behaviour to the core transmission. The total transmission decreases with increasing power and pulse width. This is partly due to the back scattering, and partly due to diffraction. For example, the reflection and the transmission at $n_2I = 0.03$ for $18fs$ was considered; the total reflection amounted to $\approx 0.003\%$, whereas the transmission loss modelled by TLM and TDBPM amounts to $\approx 2\%$ and $\approx 0.5\%$ respectively. Hence, all of the power not propagated in both models has diffracted and escaped from the simulation domain in order to support the fundamental mode within the waveguide. The reason why the TDBPM approach models "less" diffraction is due to its less "Wide angle"

behaviour compared to TLM. The use of higher-order Pade approximants should alleviate this situation [12].

From the results obtained so far for the above problem, it can be concluded that the amount of power reflected at the linear to nonlinear junction depends only on the peak power, and the transmission is dependent greatly on the total energy in the pulse. Further, the power transmitted tends to reside more in the core as the pulse is propagated. It should also be noted that the power transfer is more efficient for shorter pulses. This behaviour can be exploited in applications where high power broader mode shaped pulses needs to be transferred to a narrower mode shaped pulse.

7.4 Conclusions

Having modelled the dispersion characteristics of chalcogenide glasses, this chapter aims at modelling the instantaneous Kerr nonlinearity present in chalcogenide glasses. A TLM stub model and a z-domain model was proposed to implement the Kerr nonlinearity. The developed models were used to model a linear to nonlinear waveguide junction. The transmission and reflection was calculated and compared with an approximate time domain beam propagation method.

The results obtained fro TLM and TDBPM for reflection was in general agreement. It was noted that the frequency content of the pulse does not affect the reflection. The reflection depended on the peak amplitude of the pulse. The transmission however is affected by pulse amplitude as well as pulse duration. The difference between the reflected and transmitted power is diffracted away from the simulation domain. This effect was better modelled by TLM than by TDBPM.

So far in this study, several TLM model were considered. These can now be used to model chalcogenide glass resonator applications. The next chapter summarises the achievements of the study and proposes some future directions of research.

References

[1] A. Zakery and S. Elliott, *Optical nonlinearities in chalcogenide glasses and their applications*, vol. 135. Springer, 2007.

[2] R. Ditchburn, *Light*. Dover Books on Physics, Dover Publications, 1991.

[3] J. Liu, *Photonic Devices*. Cambridge University Press, 2005.

[4] V. Janyani, *Modelling of Dispersive and Nonlinear Materials for Optoelectronics using TLM*. PhD thesis, The University of Nottingham, 2005.

[5] J. Paul, *Modelling of General Electromagnetic Material Properties in TLM*. PhD thesis, The University of Nottingham, 1998.

[6] J. Paul, C. Christopoulos, and D. Thomas, "Generalized material models in tlm-part 3: Materials with nonlinear properties," *Antennas and Propagation, IEEE Transactions on*, vol. 50, no. 7, pp. 997–1004, 2002.

[7] S. Lane and G. Birkhoff, *Algebra*. Chelsea Publishing Series, AMS Chelsea Publishing, 1999.

[8] K. Le, R. Godoy-Rubio, P. Bienstman, and G. Hadley, "The complex Jacobi iterative method for three-dimensional wide-angle beam propagation," *Optics Express*, vol. 16, no. 21, pp. 17021–17030, 2008.

[9] E. Romanova, V. Janyani, A. Vukovic, P. Sewell, and T. Benson, "Models of non-linear waveguide excitation by non-stationary light beam," *Optical and Quantum Electronics*, vol. 39, no. 10, pp. 813–823, 2007.

[10] G. Hadley, "Wide-angle beam propagation using Padé approximant operators," *Optics Letters*, vol. 17, no. 20, pp. 1426–1428, 1992.

[11] B. Hu, *Advanced beam propagation method for the analysis of integrated photonic devices*. PhD thesis, The University of Nottingham, 2006.

[12] K. Le, T. Benson, and P. Bienstman, "Application of modified Padé approximant operators to time-domain beam propagation methods," *JOSA B*, vol. 26, no. 12, pp. 2285–2289, 2009.

8

Conclusions and Future Work

In an era where all-optical switching and controlling is of utmost importance to improve the speed of communication and control, optical resonators form the basis and useful photonic controlling devices. Some moderate to high Q factor optical resonators are applied as optical filters currently in the optical industry [1]. However, the more important aspects of high Q optical resonators are yet to be researched. Therefore, optical microresonator based research is gaining momentum to deliver the promised advantages.

The main hindrance in optical resonator research is the lack of efficient and accurate three dimensional simulation tools. Boundary integral equation based methods have good accuracy and efficiency, but are unable to cope with the nonlinear materials which would give rise to interesting properties. Time domain numerical methods on the other hand have less accuracy and efficiency, but can be used to model nonlinear materials.

8.1 The Story So Far

8.1.1 Accurate Modelling of Microresonators in TLM

This study initiated as a bid to improve the accuracy of Transmission Line Modelling (TLM) method - a time domain numerical method - in the context of optical microresonators. Several observation were made regarding the inaccuracies of time domain numerical methods by Boriskin *et. al* [2]. In this study these concerns were explored and it was understood that the inaccuracy is due to the usual and intuitive discretisation methods used. In these discretisations the modelled area/volume is either largely overestimated or underestimated giving rise to the inaccuracies and non-convergence with finer meshes.

The solution provided to solve this problem is to minimise the underestimation and overestimation as far as possible with the given mesh by the "same area" discretisation method. When an infinite cylindrical resonator was modelled with this technique, the inaccuracies in resonant frequency were lifted. Nonetheless, there was a significant error left in resonant Q factor due to the artificial surface roughness experienced by the cylinder due to stair-step approximation.

Anti-aliasing the simulation domain was then proposed to effectively "blur" the sharp corners in the stair-step approximation. A modified Lanczos filter was incorporated as the anti-alias filter applied to the spatial domain, resulting in promising improvements in the accuracy of resonant frequency and Q factor. The accuracy improvement was compared to that obtained from a commercial implementation of TLM with optimised multi-meshing with $\lambda/100$ minimum step size. Anti-aliasing produced better accuracy in Q factor even with $\lambda/10$ compared to the commercial multi-mesh implementation at the space step of $\lambda/100$. At $\lambda/10$, a shift in resonant frequency was observed, which was down to the TLM dispersion error. The results show that by using the "anti-aliasing" discretisation technique, the resonators can be modelled with significant accuracy improvement which converges with the

use of a finer mesh.

8.1.2 Frequency Extraction Methods

In order to come up with a discretisation method to improve the accuracy of resonant frequencies and Q factors represented in TLM, an accurate method was required first to estimate these parameters from a limited time signal obtained from TLM simulations. Extracting resonant peaks from the Fourier transformed time signals did not produce accurate results for the ultra high Q factors of optical resonators. Several complex frequency extraction methods were compared to identify a suitable method to extract resonances. A modified difference and recurred Prony methods,the matrix pencil method, and harmonic inversion method were thus compared.

All methods were found to estimate the resonant frequency and Q factor much better than the Fourier transform based method. However, the difference Prony method was identified as the best method and was used to extract resonances to aid in the search of better discretisation methods in TLM.

8.1.3 Perfectly Matched Layers

Even though simulations of intrinsic resonators are not much affected by the computational domain truncation, when resonators are coupled to an excitation source external to the resonator, the domain truncation plays an important role. Therefore, domain truncation methods better than TLM matched boundaries were sought. Perfectly matched layers (PMLs) are widely used in FDTD as a successful domain truncation method. However, in TLM, the efficacy of PMLs are inferior to that of PMLs in FDTD [3], [4]. Some instability concerns were also raised regarding PMLs in TLM.

In this study PMLs were implemented using various formulations. Direct implementation of Berenger's split field PML[5] in TLM was found to be much less efficient compared to previous implementations of PML in TLM [3, 4, 6]. Uniaxial PML was found to be unstable universally due to the

negative conductivity present in the formulation. Even though there exists a similar effect in convolutional PML formulation, it was made stable by removing some delayed integrating terms. This implementation was the best that were found from the study, but it still as inferior to PML implementations by Pena and Ney [3, 6], and Dubard and Pompei [4].

8.1.4 Dispersive and Nonlinear Materials

Chalcogenide glasses were identified in the beginning of the study as promising materials to be used in optical resonators. The dispersive and nonlinear effects of Chalcogenide materials can be greatly enhanced by the tight optical confinement provided by microresonators.

The refractive index measurements obtained for several glass compositions were fitted for subsequent use in TLM simulations by several material models. The Sellmeier model with one absorption peak and the Tauc-Lorentz model provided accurate representations of the measured refractive index. The Sellmeier model was implemented in TLM using a z-transform technique. The accuracy of the developed model in TLM was muddled by the the TLM mesh dispersion observed at $\lambda/10$ discretisation. However, the accuracy was improved with a finer mesh.

Kerr nonlinearity present in chalcogenide glass materials were also modelled using both stub and z-transform techniques. A nonlinear waveguide junction was modelled and compared with a time domain beam propagation method developed by a collaborating researcher, Dr. Khai Le, University of Belgium. The results obtained from both methods were in broad agreement, but TLM modelled the propagation in the nonlinear waveguide better.

8.2 Future Directions

The most prominent outcome of this study is the ability to model optical resonators by anti-aliasing the simulation domain. This was only achieved for linear dielectric materials in the current study. This can be carefully

extended towards other materials such as dispersive and nonlinear materials. Care to detail and thorough testing is required in these materials because the behaviour of waves are defined by several parameters in such materials. Anti-aliasing is effectively an averaging method. Hence, a solid recipe is needed to be found when combining materials of several parameters to be placed in the blurred boundary region.

Since PMLs were not very successfully implemented in this study, a thorough understanding of PMLs in TLM should be further studied. In a literature review of PML implementations in TLM it was understood that only a handful of publications have emerged from PML implementations. Therefore, further research is required to understand why PMLs do not work in TLM as well as they do in FDTD. Such a research would require one to delve into the mesh dispersion characteristics of TLM in the electrical circuit level. Further it will help formulate a workaround to compensate the errors to form better boundary conditions.

Once the above mentioned issues are resolved, methods to improve the efficiency of TLM and time domain numerical methods in general can be proposed. One such proposal is to simulate only the regions of space that contain significant electromagnetic energy at a given time. This would improve the simulation time of waveguide propagation, but not so much in sub-wavelength optical resonators.

Further, the complex resonance frequency extraction method used in this study can be employed to predict the behaviour of electromagnetic field and hence reduce the computational effort required for modelling transient effects in TLM and other time domain numerical electromagnetic methods.

8.3 Conclusions

In the presented study, accuracy improvement of TLM in modelling optical resonators was achived by the anti-aliasing discretisation method and a same area method. Anti aliasing method emerged as the best discretisation method.

Future directions are recommended to employ the anti-aliasing technique for dispersive and nonlinear materials.

A difference Prony method was identified as the best method to extract spectral information from a limited time signal. It was also proposed as a method to improve the efficiency of modelling optical resonators as a future direction.

Several PML implementations formulated for TLM in this study have not been as successful as in FDTD, but future directions are given to understand how this can be improved.

Chalcogenide glasses were modelled as dispersive and nonlinear materials in TLM. The models can be used to predict the behaviour of optical resonators in the future and to design new geometries exploiting the beneficial properties of these materials.

References

[1] J. Hryniewicz, P. Absil, B. Little, R. Wilson, and P. Ho, "Higher order filter response in coupled microring resonators," *Photonics Technology Letters, IEEE*, vol. 12, no. 3, pp. 320–322, 2000.

[2] A. V. Boriskin, S. V. Boriskina, A. Rolland, R. Sauleau, and A. I. Nosich, "Test of the FDTD accuracy in the analysis of the scattering resonances associated with high-Q whispering-gallery modes of a circular cylinder," *J. Opt. Soc. Am. A*, vol. 25, pp. 1169–1173, May 2008.

[3] N. Peña and M. Ney, "A new TLM node for Berenger's perfectly matched layer," *Microwave and Guided Wave Letters, IEEE*, vol. 6, pp. 410 –412, Nov 1996.

[4] J. Dubard and D. Pompei, "Optimization of the PML efficiency in 3-d TLM method," *Microwave Theory and Techniques, IEEE Transactions on*, vol. 48, no. 7, pp. 1081–1088, 2000.

[5] J. Berenger, "A perfectly matched layer for the absorption of electromagnetic waves," *Journal of computational physics*, vol. 114, no. 2, pp. 185–200, 1994.

[6] N. Pena and M. M. Ney, "Absorbing-boundary conditions using perfectly matched-layer (PML) technique for three-dimensional TLM simulations," *Microwave Theory and Techniques, IEEE Transactions on*, vol. 45, pp. 1749–1755, Oct 1997.